Power-line sparking noise characterisation in the SKA environment

by

Philip Kibet Langat

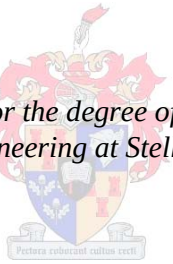

Dissertation presented for the degree of Doctor of Philosophy in the Faculty of Engineering at Stellenbosch University

Supervisor: Prof. Howard Charles Reader
Faculty of Engineering
Department of Electrical&ElectronicEngineering
University of Stellenbosch

December 2011

Declaration

By submitting this dissertation electronically, I declare that the entirety of the work contained therein is my own original work that I am the sole author thereof (save to the extent explicitly otherwise stated), that reproduction and publication thereof by Stellenbosch University will not infringe any third party rights and that I have not previously in its entirety or in part submitted it for obtaining any qualification.

Date: 3 May 2011

Abstract

The Square Kilometre Array (SKA) and its demonstrator *Meer*KAT are being designed to operate over a wide frequency range and are expected to achieve greater sensitivity and resolution than existing telescopes. The radio astronomy community is well aware of the negative impact that radio frequency interference (RFI) has on observations in the proposed frequency band. This is because weak radio signals such as those from pulsars and distant galaxies are difficult to detect on their own. The presence of RFI sources in the telescope's operating area can severely corrupt observation data, leading to inaccurate or misleading results.

Power-line interference and radiation from electric fences are examples of RFI sources. Mitigation techniques for these interference sources in the SKA system's electromagnetic environment are essential to ensure the success of this project. These techniques can be achieved with appropriate understanding of the characteristics of the noise sources. Overhead power-line interference is known to be caused mainly by corona and gap-type (commonly known as sparking noise) discharges. Sparking noise is the dominant interference for the SKA. It is mainly encountered on wooden pole lines, which are usually distribution lines operated at up to 66 kV AC in the South African network. At this voltage level, the voltage gradients on the lines are insufficient to generate conductor corona. The power requirements for SKA precursors will be below this voltage level.

The aim of the research in this dissertation is to evaluate the power line sparking characteristics through measurements and simulation of line radiation and propagation characteristics. An artificially made sparking noise generator, which is mounted on a power line, is used as noise source and the radiation characteristics are measured. Measurements were carried out in different environments, which included a high-voltage laboratory (HV-Lab), a 40m test-line, and another 22-kV test line of approximately 1.5 km. The key sparking noise parameters of interest were the temporal and spectral characteristics. The time domain features considered were the pulse shape and the repetition rate. The lateral, longitudinal and height attenuation profiles were also quantified.

Since sparking noise current pulses are injected or induced onto power line conductors, the line will act as an unintentional antenna. The far-field radiation characteristics of the line were evaluated through measurements on physical scale-model structures and simulations. $1/120^{th}$ and $1/200^{th}$ scaled lines, using an absorbing material and metallic ground planes, respectively, were simulated in FEKO. The measurements of the constructed scale models were taken in the anechoic chamber. Both measurements and simulations showed that the line exhibits an end-fire antenna pattern mode. Line length, pulse injection point and line configuration were some of the parameters found to affect the radiation patterns.

The findings from this study are used to determine techniques to identify the sparking noise, and locate and correct the sources when they occur on the line hardware. Appropriate equipment is recommended to be used for the location and correction of sparking noise.

Opsomming

Die Vierkante Kilometer Reeks (SKA) en sy demonstrasie projek, die Karoo Reeks Teleskoop (KAT), word ontwerp om oor 'n wye frekwensie-bereik te funksioneer. Beide sal na verwagting beter sensitiwiteit en resolusie as bestaande radioteleskope hê. Die radio-astronomie-gemeenskap is deeglik bewus van die negatiewe impak wat radio-frekwensie steurnisse (RFS) op waarnemings in die voorgestelde frekwensieband het. Die rede hiervoor is dat swak radio-seine soos dié van pulsars en verafgeleë sterrestelsels inherent moeilik is om te bepaal. Die teenwoordigheid van RFS bronne in die teleskoop se onmiddellike operasionele gebied kan waarnemings nadelig beïnvloed. Dit lei uiteindelik tot onakkurate of misleidende resultate.

Kraglyne en uitstralings van elektriese heinings is voorbeelde van RFS bronne. Metodes om die oorsake van die steurnisse van die SKA se elektromagnetiese omgewing te verminder is noodsaaklik om die sukses van hierdie projekt te verseker. Dit vereis egter deeglike begrip van die eienskappe van hierdie bronne. Steurnisse as gevolg van oorhoofse kraglyne word hoofsaaklik veroorsaak deur korona en gapingtipe ontladings (algemeen bekend as vonkontladings). Vonkontladings word hier beskou as die belangrikste oorsaak van steurnisse vir die SKA. Dit word in die Suid-Afrikaanse netwerk hoofsaaklik aangetref op houtpaal-installasies, wat gewoonlik bestaan uit distribusie lyne wat tot en met 66 kV wisselstroom (WS) bedryf word. By hierdie operasionele spanning is die spanningsgradiënt op die lyn onvoldoende om korona op te wek. Die kragvereistes vir die SKA se voorafgaande projekte sal sodanig wees dat hierdie spanningsvlak nie oorskry sal word nie.

Die doel van die navorsing omskryf in hierdie proefskrif is om die eienskappe van vonkontladings rondom kraglyne te evalueer. Dit word gedoen met behulp van metings en simulasies van uitstralings- en voortplantingspatrone wat met ŉ spesifieke lyn geassosieer kan word. ŉ Kunsmatige vonkontladingsopwekker word op ŉ kraglyn geplaas en dien as bron om die uitstralingspatrone te meet. Metings is uitgevoer in verskillende omgewings, insluitende 'n hoogspanningslaboratorium (HV-Lab), 'n 40 m toetslyn en 'n 22 kV WS toetslyn van ongeveer 1.5 km lank. Die hoof vonkontladings eienskappe van belang is die temporale en spektrale eienskappe. Die tydgebied-eienskappe wat ondersoek is, is die pulsvorm asook die pulsherhalingskoers. Die laterale, longitudinale en hoogte-attenuasie profiele word ook gekwantifiseer.

Aangesien stroompulse deur vonkontladings op die kraglyn geplaas of geïnduseer word, sal die lyn as ŉ ongewenste antenna optree. Die ver-veld uitstralingskenmerke van die lyn is ook geëvalueer deur gebruik te maak van fisiese skaalmodelstrukture en -simulasies. 1/120ste en 1/200ste geskaleerde lynmodelle, wat onderskeidelik ŉ absorberende- en metaalgrondvlak bevat, was gebruik om ŉ 3 spanlengte kraglyn te simuleer met behulp van FEKO. Metings van die fisiese skaalmodel strukture is in ŉ anegoïse kamer geneem. Beide die metings en die simulasies toon dat die lyn ŉ endpunt uitstralingspatroon het. Lynlengte, die opwekkingsposisie van die stroompuls en die lynkonfigurasie is ‘n paar van die parameters wat die uitstralingpatroon beïnvloed, soos in die navorsing aangedui.

Die bevindinge van hierdie studie word gebruik om steurnisse as gevolg van vonkontladings op die kraglyn te identifiseer, op te spoor en uiteindelik reg te stel. Toepaslike toerusting word voorgestel wat gebruik kan word vir die identifisering en opsporing van vonkontladings.

Acknowledgements

I would like to acknowledge the contributions of the following whose help and support were very invaluable during the development of this dissertation. I would like to express my sincere thanks to my promoter, Prof. Howard Reader, for his invaluable guidance, encouragement and unfailing assistance throughout this research. I am grateful to Dr. Wernich de Villiers and Dr. Adrian Tiplady for the design of the spark-gap device and their assistance in measurements.

Many thanks also go to Dr. Braam Otto and Dr. Paul van de Merwe for their insights and assistance particularly with the Klerefontein and the anechoic chamber measurements. I gratefully acknowledge the valuable assistance from Petrus Pieterse while taking measurements in the high-voltage laboratory and the short test-line. I also thank Wessel Crouwkamp, Ulrich Büttner and Lincon Saunders for helping in the construction of the scale models, and André Swart and Murray Jumat for their assistance in the high-voltage laboratory and short test-line measurements.

I thank Martin Siebers for his help in setting up scale model measurements at the anechoic chamber. I appreciate the great assistance from Joely Andriambeloson in taking measurements especially at the short test-line, the high-voltage laboratory and in the anechoic chamber. I would like to acknowledge the technical support from Carel van der Merwe, Jasper Grobbelaar, Dawie Snyman, and Gerrit Coreejes during the Klerefontein measurements. Kim de Boer, Dr. Richard Lord, and the KAT Office are thanked for facilitating the measurements especially in organising the logistics related to the Klerefontein tests.

I acknowledge all the support from Dr. Gideon Wiid with regards to the scale model simulation setups and useful power line design philosophy information. I thank Mel van

Rooyen of EMSS for his help in refining FEKO models. Dr. Evan Lezar is thanked for his help in accessing the Stellenbosch University high performance computer centre (Rhasatsha). Many thanks go to Riaan Roets of ESKOM for the enlightening discussions on noise source location techniques. South Africa's SKA office and electricity utility, ESKOM (TESP), are gratefully thanked for the bursary and research funding linked to this programme.

I thank Gideon and Paul for their help with the Opsomming. To all postgraduate students with whom I shared the E212 office space, many thanks for your friendship and for creating a good working environment.

Finally, I thank my parents and siblings for their continuous support and encouragement throughout my entire studies.

Table of Contents

List of Figures

List of Tables

Nomenclature

AGA	Astronomy Geographic Advantage
ALMA	Atacama Large Millimeter Array
AM	Amplitude Modulation
CM	Common-mode
dB	Decibel
EM	Electromagnetic
EMC	Electromagnetic Compatibility
EMI	Electromagnetic Interference
FFT	Fast Fourier Transform
FoV	Field of View
GMRT	Giant Metrewave Radio Telescope
HF	High Frequency
HPC	High Performance Computing
HV-Lab	High-Voltage Laboratory
IF	Intermediate Frequency
IFFT	Inverse Fast Fourier Transform
ISSC	International SKA Steering Committee
ITU	International Telecommunication Union
JWST	James Webb Space Telescope
Jy	Jansky
KAT	Karoo Array Telescope
LNA	Low Noise Amplifier
LPDA	Log Periodic Dipole Array
M*eer*KAT	Karoo Array Telescope (Final Phase)
MoM	Method of Moments

NF	Noise Figure
PEC	Perfect Electric Conductor
RA	Radio Astronomy
RBW	Resolution Bandwidth
RF	Radio Frequency
RFI	Radio Frequency Interference
RSA	Republic of South Africa
SA	Spectrum Analyzer
SARAS	South African Radio Astronomy Service
SG	Spark Gap
SKA	Square Kilometre Array
SMA	Sub-miniature version A
spfd	spectral power flux density
TVI	Television Interference
VHF	Very High Frequency
VNA	Vector Network Analyzer

Chapter 1

Introduction

1.1 SKA project background

Radio astronomers proposed a concept for an international radio telescope array with a collecting area of a square kilometre in the early 1990s [1,2]. This was meant for investigating various outstanding astrophysical problems such as surveying of the red-shifted neutral hydrogen and searching for pulsars. This concept “gave birth” to the Square Kilometre Array (SKA) project which is an international project to design and build a new generation radio telescope that operates at metre to centimetre wavelengths [3]. It will be a multi-purpose radio telescope operating in the frequency range from 70 MHz up to at least 25 GHz [3,4].

Its specifications have been expanded from the original concept to allow astronomers to answer more fundamental scientific questions about the origins and evolution of the universe [5]. Together with the wide frequency coverage and the large collecting area, this instrument will achieve unprecedented sensitivity as well a large angular field of view (FoV). It will complement major ground and space-based astronomical facilities under construction or planned in other parts of the electromagnetic (EM) spectrum (e.g. Atacama Large Millimeter Array (ALMA), James Webb Space Telescope (JWST), etc.). Its capabilities are projected to be between 50 and 100 times more sensitive than the largest existing synthesis arrays. This will enable the instrument to detect extremely faint astronomical radio signals.

Although the technology definition continues to evolve, the SKA’s system design proposes the use of phased aperture array technology as the primary collector type for the frequencies below 1 GHz. This will be made up of sparse aperture array in the form of two crossed dipole

antennas for the lowest frequencies of observation. Dense aperture array in the form of closely packed antennas arranged in tiles are expected to be utilized for the mid-frequencies while the 12-15 m dish antennas will be used for the higher frequencies [6]. The distribution of the entire array will be in baselines extending from a few tens of metres to some thousands of kilometres. An example configuration for the array is illustrated in Figure 1-1.

Figure 1-1: An artist's animation of the SKA core site, with aperture arrays and dishes visible [6].

To build the SKA, the initial siting proposals were received from Argentina, Australia, Brazil, China, the Republic of South Africa (RSA), and the USA. The RSA and Australia were short-listed by the International SKA Steering Committee (ISSC) to bid for hosting the radio telescope. In each of these two countries, work is being carried out to study and prototype the technologies that could be used to construct the array. The RSA is developing a precursor telescope for the SKA project in the form of dish antenna array, which is currently under construction in the Karoo area of the Northern Cape Province. This demonstrator, known as Karoo Array Telescope (KAT or M*eer*KAT), will be an array of 64 offset Gregorian dishes each dish having an effective diameter of 13.5 m [7]. This follows the initial development of

an interferometer array made up of seven 12 m dish antennas, called KAT-7, which was used as a prototype. The construction of the latter array, shown in Figure 1-2, has been completed and is currently being evaluated to come up with optimized design specifications for the M*eer*KAT.

Figure 1-2: A view of the KAT-7 array [7]

Due to the large number of antennas and other support facilities, electric power provision forms one of the major infrastructural parts of this project. Since the telescope site is located in a remote area, substantial new power supply infrastructure needs to be provided. For the M*eer*KAT project, a 33 kV grid power line has been designed, constructed and routed from the Carnarvon substation to the site. The line has 3 sections: the first section from the substation is an overhead line suspended on wooden poles, the second section that connects the first part to an onsite facility is an overhead line suspended on mono structure steel poles, and the last section from the onsite facility to the M*eer*KAT dishes is of an underground cable. This line, although it is designed for a capacity of 33 kV, will initially be energized at 22 kV. The power requirement for the SKA is still under investigation and its distribution network is expected to be more complex than that of the M*eer*KAT.

1.2 RFI and radio astronomy

Radio telescopes are passive communication devices, which only receive radio signals (of natural, cosmic origin) and do not transmit radiation themselves. Due to the very long distances between astronomical objects and the telescopes, the radiated signals from these objects arriving at the receivers are extremely weak. This necessitates the use of very sensitive receivers to detect them above the noise floor level. A complication that often faces the radio astronomy (RA) community is the presence of various radio frequency interferers radiating within the radio telescope's frequency band of operation. This has a negative impact on observational RA since the weak astronomical signals can easily be masked or contaminated by the strong signals from these interferers. This would either impede observations altogether or lead the astronomers into making erroneous data interpretations.

With the SKA and the M*eer*KAT planned to operate within a very wide frequency range (most of which being outside the bands set aside for RA by the International Telecommunication Union (ITU)), the presence of man-made radio frequency interference (RFI) from a variety of sources can present a great challenge to them. Other frequency spectrum users already occupy the allocated frequency band. The interferers that are of concern include aircraft distance measuring equipment, cellular phone signals, television and radio broadcasts, orbiting and geostationary satellites. Others are power-line radiation due corona and gap-type discharges, nearby electric fence sparking noise, and local interference from electronic equipments within the telescope's system. The signals from these interferers are much stronger than the relevant astronomical signals negatively affecting observations. The measurements of these astronomical signals are usually expressed in terms of spectral power flux density (spfd) whose unit is dB(W/m^{2}Hz) i.e. power in Watts falling on a square metre of antenna collecting area per hertz of receiver bandwidth. Because of the tiny amounts of power received from cosmic sources, their spfd is usually specified in terms of the Jansky (Jy) i.e.

$$1Jy = 10^{-26} Wm^{-2} Hz^{-1} = -260dB(W/m^2 Hz) \qquad 1\text{-}1$$

To ensure successful use of these devices, RFI mitigation techniques for the various interference sources are essential. This would, first, require that the telescope be located within an area free from most of these interference sources. This is mainly aimed at reducing the effect caused by the man-made interfering sources that are external to the telescope system. The main consideration of the site to locate the M*eer*KAT and possibly the SKA was the RFI environment. The Karoo area of the Northern Cape Province has a very low human settlement and thus low man-made RFI. The Government of the RSA has further, through the Astronomy Geographic Advantage (AGA) Act [8], declared the site as a radio quiet zone. The South African Radio Astronomy Service (SARAS) protection levels [9], which are based on the ITU Recommendation ITU-R RA.769-2 [10], governing the amount of RFI radiation in the site have also been proposed. The core site is also situated in a mountainous terrain, which would further aid in shielding the telescope antennas from the interferences due to most of the land-based radiators.

Proper electromagnetic compatibility (EMC) principles are necessary in designing and installing the electronic equipment used within the telescope system. This is to prevent or minimize the internally generated RFI from affecting the operations of the telescope.

Other RFI sources, which would require proper design and maintenance guidelines, include the power line generated noise. This is in the form of either corona or sparking discharge noise. To mitigate these kinds of noise sources requires an understanding of their characteristics. This dissertation investigates the characteristics of power line electromagnetic noise with a specific emphasis on the sparking discharge type of noise.

1.3 Research Description

Overhead high voltage power lines generate undesirable electromagnetic interference (EMI), which could cause detrimental effects to the operation of various sensitive facilities such as the radio telescopes that operate near these lines. This EMI is mainly caused by electrical

discharges due to conductor corona, sparking at highly stressed areas of insulators, and sparking discharges at loosely bonded line hardware [11]. Conductor corona is most prevalent on high voltage transmission lines [12], which on South Africa's power line network operate from 132 kV and above. Sparking noise on the other hand is a major EMI source on distribution lines [12]. These lines operate at 66 kV and below (in the South African network) and are usually constructed on wooden pole distribution lines. At these voltage levels, the voltage gradients on the lines are insufficient to generate conductor corona [13]. Therefore, due to the power requirements of the SKA precursor instruments, which will utilize 33 kV capacity lines, the contribution from conductor corona to the overall power line noise will be insignificant.

The research in this dissertation focuses mainly on the sparking type of power line noise by investigating its characteristics. The power lines could be those supplying electric energy to the telescope or those located within the surrounding environment. When noise sources are present on these lines, the resulting sparking discharge currents are induced onto the line conductors. This turns the lines into unintentional radiators. The resulting radiated electromagnetic field can be measured or detected in the form of time domain pulses as well as characteristic energy in the frequency domain spectrum. Both the time and frequency domain descriptions have specific noise properties.

Numerous investigations, such as in [11] - [13], have reported the characteristics of radiated power line interference where it is found that the radiated sparking noise frequency spectrum reaches across a wide range of frequencies. These studies were mainly concerned with the effect of the power line noise on services such as amplitude modulation (AM) radio and television reception. The effect to the latter is commonly referred to as television interference (TVI). The referred findings observed the noise field strength decaying after a frequency of 100 MHz and reaching about 1 GHz. The noise behaviour at a wider frequency range is necessary in order to understand the effect of this noise on the planned telescope operations, which will operate at a very wide frequency band.

The frequency and time domain properties of this noise are investigated here by undertaking measurements using an artificial spark-gap device that act as a noise generator. These tests are performed in three environments: a high-voltage laboratory, a 40 m three-wire test-line, and an approximately 1.5 km, three-phase, test-line. During the tests, the source is mounted on one of the energized line conductors. A wide bandwidth oscilloscope is used for measuring the time domain pulse properties such as the pulse rise times and repetition rates. The discharge pulses are also measured in the time domain using a spectrum analyzer (SA) set to zero-span mode. Due to the broadband nature of the noise, a SA operating at a wide frequency range and having various resolution bandwidth (RBW) settings is utilized to evaluate the frequency spectrum of the noise. The effect of the variation of the SA's RBW on the frequency spectrum is evaluated. The influences of the change in gap length, supply voltage levels, and the measurement environment on the noise frequency spectrum are also investigated.

To understand the propagation of the pulses onto the long power line conductors, lateral, longitudinal and height profiles of the noise were examined. This involved travelling along the line while taking measurements at various measurements positions for the longitudinal profile. For the lateral profile case the measurements were taken at measurement positions that were perpendicular to the line. These are to determine the extent of the noise field strength decay with distance from the source and from the line, respectively. The measurements for the height profile on the other hand were taken while varying the height of the measuring antennas.

In addition to the spectral extent and time properties of any sparking noise, an investigation of the radiation pattern characteristics of this noise due to the power line system itself is also undertaken in this research. This would give an indication on the possible interaction between the radiated fields from the lines and the receiving antennas located near such lines. This is done through numerical simulations and physical scale model lines. Numerical modelling of various power line configurations is undertaken using FEKO [14], which is a Method-of-

Moment-based frequency domain electromagnetic code. The radiation characteristics of these lines depend on such factors as the frequencies of the source, line length, spacing between the conductors, line impedances, line topology, ground properties, position of the source along the line, measuring antenna heights *etc*. From the simulations, the effect on the radiated field patterns was evaluated while varying these parameters. A Sommerfeld integral ground plane was included in FEKO to represent the dielectric nature of the soil at the location of the radiating power line. The physical scale model structures for simple line geometries were constructed and the radiated field patterns measured in the anechoic chamber using high-dynamic-range measurement equipment. The measured field patterns were compared with the simulation from the corresponding line configurations.

1.4 Dissertation contributions and claims

In this research, the radiated sparking noise has been shown to have a wide frequency spectrum which, as determined by equipment available in our laboratories, extends well beyond 3.6 GHz. This has not been previously reported in the literature. A new, double-exponential, time-domain pulse is proposed which describes the measured characteristics of radiated sparking phenomena. This pulse will predict all the measured observations to the bandwidth of our present 3.6 GHz systems. More sensitive systems are expected to show the noise components at higher frequencies still.

The recorded emissions levels are also shown to vary with the change in the RBW of the measuring receiver. This level variation is found to be higher than that of the white noise with the instrument noise floor level changing by the expected 10 dB, per frequency decade of the RBW. Due to the impulsive nature of the sparking noise, its levels, on the other hand, change by around 20 dB, per frequency decade of the RBW. This reinforces the observations made by Hodge [15].

The effect of the variation of a spark-gap length on the frequency spectrum was investigated and it was found that the shorter lengths had a slightly higher energy level across the frequency band as compared to the larger gap lengths. This is due to the increase in the gap impedance with the increased electrode spacing and a higher voltage being required to overcome the air breakdown field strength within the gap.

The investigation of the radiation characteristics of the power lines has shown the lines to have complex radiation patterns, which depend on the source position on the line, the line geometric topology, the ground plane properties, and the source frequencies. The line impedance was found to have insignificant influence on the shape and symmetry of the line radiation patterns. Notwithstanding the influence of these parameters, the overall azimuthal field patterns are found to have the characteristics of an end-fire pattern.

1.5 Dissertation structure

To mitigate the power line noise, it is important to understand its characteristics and also its possible sources. An overview on both corona and sparking discharge noise is provided in Chapter 2. Some of the potential sources of sparking noise on power lines are highlighted. Published literature on some of the measured characteristics of sparking noise is also discussed. Measurement instrumentation, used for the tests reported in this dissertation, as well as the measurement environments, are detailed in chapter 3. The measured results of the characteristics of sparking noise, such as spectral and temporal spectra for radiated and conducted cases, are discussed in chapter 4. The radiated longitudinal, lateral and height profiles of this noise are also provided in this chapter.

To further understand the propagation and radiation characteristics of a power line due to induced sparking noise currents from a source, scale model structures representing simple line configurations were simulated using FEKO. Physical scale models were also constructed and measured in an anechoic chamber. These are discussed in chapter 5, which also compares the

measured and simulated radiation patterns from these models. Chapter 6 details the localization, correction, prevention and mitigation measures for sparking noise on power lines. The measures that have been put in place to minimize the occurrence of this noise on the newly-constructed power line to supply M*eer*KAT have also been highlighted in this chapter. Finally, chapter 7 provides concluding remarks of the entire dissertation and gives some recommendations for future research studies.

The following is a list of publications and presentations arising from the research presented on this dissertation.

- *P. Kibet Langat and H. C. Reader,* "On the Evaluation of Radiated Power Line Sparking Noise Characteristics", submitted to SAIEE Transactions October 2010.
- *P. Kibet Langat, P S van der Merwe, T Ikin, H C Reader,* "CAT-7 Cable Evaluation for Square Kilometre Array Analogue Signal Transport", SAIEE Africa Research Journal, Vol. 102, No. 1, March 2011, pp 2-7.
- *T.S. Ikin, P.N. Wilkinson, A.J. Faulkner, M. Jones, A. Baird, A.K. Brown, D. George, G. Harris, P.L. Kibet, M. Panahi, H.C. Reader, S. Schediwy, P.S. van der Merwe, K. Zarb-Adami, and Y. Zhang,* "Progress on Analogue Front end for 2PAD", Widefield Science and Technology for the SKA SKADS Conference 2009, S.A. Torchinsky, A. van Ardenne, T. van den Brink-Havinga, A. van Es, A.J. Faulkner (eds.),, Chateau de Limelette, Belgium, 4-6 Nov. 2009, pp. 267-272.
- *P G Wiid, H C Reader, R H Geschke, P S van der Merwe, P L Kibet*, "Developing RFI Studies on KAT-7: Lightning, Earthing and Cabling", 2009 SA IEEE AP/MTT Conference, all invited papers, abstracts published only, Technopark, Stellenbosch, Mar 2009.
- *L P Kibet, W de Villiers and H C Reader*, "Characterisation of spark-gap radiated noise", SAUPEC 2009, Proc. 18th Southern African Univ. Power Eng. Conf, Protea Hotel, Stellenbosch, Jan 2009, paper 18, CD ROM.

- *L P Kibet and H C Reader*, "Power line radiated sparking noise", SAUPEC 2010, Proc. 19th Southern African Univ. Power Eng. Conf, Wits University, Johannesburg, Jan 2010, CD ROM.
- *P Kibet Langat and H C Reader*, "Power-line sparking noise characterization in the SKA environment", South African SKA / M*eer*KAT Project, 5th Annual SKA Postgraduate Bursary and Postdoctoral Fellowship Programme, Stellenbosch, Dec. 2010, presentations available on SKA website: www.ska.ac.za.
- *P L Kibet and H C Reader*, "Characterization of radiated sparking noise in the SKA environment", South African SKA / M*eer*KAT Project, 4th Annual SKA Postgraduate Bursary and Postdoctoral Fellowship Programme, Stellenbosch, Dec. 2009, presentations available on SKA website: www.ska.ac.za.
- *P L Kibet and H C Reader*, "RFI Mitigation for Electronic and Natural SKA Environment", South African SKA / M*eer*KAT Project, 3rd Annual Postgraduate Bursary Conference, Stellenbosch, Dec 2008, presentations available on SKA website: www.ska.ac.za .
- *H C Reader, R H Geschke, P G Wiid, P L Kibet, A J Otto and P S van der Merwe*, "EMC and RFI Mitigation for Developing Large Systems: Experience from South Africa's SKA Demonstrator", address given to EM Divisions of NIST (National Institute of Standards and Technology), Boulder, Colorado, December, 2009.

Chapter 2

AC Power line EMI sources

2.1 Introduction

Electrical power from a utility's generating plant is transported to consumers via transmission and distribution lines. These power networks mainly consist of overhead lines and in some instances underground power lines. These lines are operated at different voltages with transmission lines being at higher-voltage ratings while the distribution lines operate at lower voltage, at most 66 kV in the South African network. These lines are constructed with supporting structures, either wooden poles or steel poles, or a combination of both, where one section is steel-structured while wooden poles are used in the remaining section. In all these lines, a wide variety of hardware/fittings and pole configurations can be found.

Overhead power lines have been found to be a source of EMI mainly due to electrical discharges from conductor corona in the air at the surfaces of conductors and fittings, sparking at highly stressed areas of insulators, and gap-type discharges at loosely bonded line hardware [16]. The noise signals generated by these discharges may be conducted and/or radiated by the power line network and may interfere with nearby communication facilities.

Other noise sources associated with power lines include signals intentionally injected onto the lines by connected devices such as broadband-over-power-line carriers. These signals may be radiated by these lines and thus interfering with the operations of other spectrum users. Power line conductors can also easily pick up radiated electromagnetic noise signals from sources such as lightning, thunderstorms, automobile ignition systems, etc, which are either reradiated or conducted [17]. Transients or impulses caused by rapid rates of current change in inductive

loads, switches and circuit breakers may also be conducted through power lines causing connected electronic equipment to malfunction [17].

The corona and sparking noise have been found to be the main EMI sources with the sparking type contributing at least 90% of all reported power line related noise [18]. In this chapter, the generation mechanisms and characteristics of both corona and sparking noise are described with the emphasis on the latter.

2.2 Generation mechanisms of power line noise

2.2.1 Corona noise/discharge

Conductor corona from high-voltage transmission lines is generally categorized into two types: pulse-less or glow corona and pulse-type or streamer corona discharges [19]. They both cause energy loss on power line conductors and audible noise near the transmission line. The pulse-type corona is the only one that causes EMI. Due to our interest in EMI, only the pulse-type corona is briefly described here.

Conductor corona discharges are mostly generated due to the presence of conductor surface irregularities. These could be in the form of a defect, caused by damage or poor design, which protrudes above the nominal conductor surface and thus increasing the electric field intensity around the conductor. Water droplets, bird droppings, insects, snow, and dust/dirt formed on the conductor surfaces also form bulges which can result in corona discharges [20]. Depending on the presence of surface irregularities, atmospheric conditions and the level of line voltage gradient among other parameters, corona discharge sources are randomly distributed along the high voltage power line conductors [20]. From several studies, a higher corona activity occurs mainly during foul weather such as rain, as compared to that found during fair weather conditions [21]. These discharges can occur on all the three voltage phase conductors and the amount of corona intensity generally decreases with the line voltage.

This conductor corona noise is generated due to partial electrical discharge caused by ionization of air surrounding the irregularities on the surfaces of electrical conductors of power lines at high voltages. This ionization generates streamers, which carry electric charges into the surrounding air away from the conductor surfaces. This results in current in the conductor, which accumulates due to electron avalanche. This occurs when the electric field intensity at the surfaces of the conductors exceeds the corona onset electric field [21]**.** After the current reaches its maximum, it will start falling due to the lowering of the electric field intensity [19]. These generated corona currents are in the form of pulses having short rise times and relatively longer fall times. The currents get injected or induced onto the power line conductors and get conducted or radiated, thus causing time varying EMI fields [22].

2.2.2 Corona noise characteristics

The presence of corona is characterized by visual effects, a violet-coloured light, due to free photons released during the ionization process. An acoustic audible noise in the form of a hissing or frying sound is also produced during the corona discharge process [20]. Radio interference due to radiated or conducted EM fields from the lines can be observed in the time domain as repetitive pulses having a fast rise time and short duration. The frequency spectrum of the radiated EMI from these pulses is dependent on the rise time.

2.2.2.1 Time domain corona current

Corona current pulses are double exponential in nature and occur on both positive and negative half-cycles of the 50Hz power line frequency. These pulses can be represented in the form given by equation 2-1 [19], [23].

$$I(0,t) = K_p I_p\left(e^{-\alpha t} - e^{-\beta t}\right), \qquad t \geq 0 \qquad 2\text{-}1$$

Here K_p, I_p, α and β are empirical constants which are influenced by discharge conditions making them to vary randomly. I_p is the current amplitude in mA while t is time in

nanoseconds (*ns*). It has been found that the amplitudes of positive pulses are higher than those of the negative pulses [24]. The latter have much smaller rise and fall times but much higher repetition rates than the former. Typical average parameters defining these pulses i.e. the amplitude, rise time and duration are given in Table 2.1 [19], [24].

Table 2-1: Typical parameters of corona current pulses [19], [24]

Pulse type	**Peak current Amplitude (mA)**	**Rise Time (ns)**	**Pulse Duration to 50% (ns)**	**Repetition rate (Pulses/s)**	
				AC	**DC**
Positive Corona	100	50	200	Power frequency (PF)	$10^3 – 5.10^3$
Negative Corona	10	20	50	100 x PF	10^4 - 10^5

Here, the pulse rise time t_r is the time interval where the pulse amplitude changes from 10% to 90% of its maximum value. The pulse duration to 50%, *d*, is the interval between the time where the pulse amplitude is 50% on the rising edge and the time it drops to 50% on the falling edge with both edges being nearest to the maximum point, as shown in Figure 2-1 [25].

From experimental measurements made by Begamudre [19], the typical time-domain representation for a positive corona pulse can be written as shown in equation 2-2:

$$I_+(0,t) = 2.35 I_p (e^{-0.0105t} - e^{-0.03465t}) \quad 2\text{-}2$$

Similarly, a typical negative corona pulse can be written as [24]:

$$I_-(0,t) = 1.3 I_p (e^{-0.019t} - e^{-0.285t}) \quad 2\text{-}3$$

These pulses are plotted in Figure 2-1 with amplitudes of 100 *mA* and 10 *mA* for positive and negative pulses, respectively.

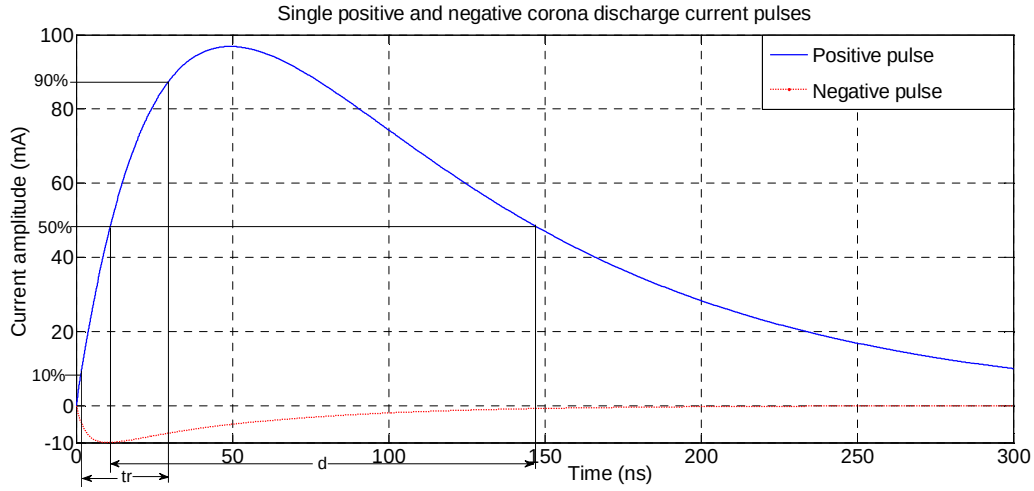

Figure 2-1: Corona discharge current pulses (after [19], and [24])

2.2.2.2 Frequency domain of corona noise

Corona current pulses generate EMI whose characteristics depend on the nature of the frequency spectrum of these currents. These frequency spectral characteristics are related to the pulse time-domain properties through the Fourier transform (FFT) of a single pulse [26]. For a double exponential pulse such as that given in equation 2.1, the transformation from time domain, *f(t)*, to frequency domain, *F(ω)*, can be represented by the following equation:

$$F(\omega) = \int_{-\infty}^{\infty} f(t) e^{j\omega t} dt = \int_{-\infty}^{\infty} KI_p \left(e^{-\alpha t} - e^{-\beta t}\right) e^{j\omega t} dt \qquad 2\text{-}4$$

where $\omega = 2\pi f$ is the angular frequency with f being the frequency. This gives a magnitude, in dB, for a single pulse, as

$$|F(\omega)| = 20 log_{10} \left[KI_p \frac{\beta - \alpha}{\sqrt{(\beta^2+\omega^2)(\alpha^2+\omega^2)}} \right] \qquad 2\text{-}5$$

Equation 2-5 gives the typical relative frequency spectra, shown in Figure 2-2, for both positive and negative corona pulses given in equations 2.2 and 2.3.

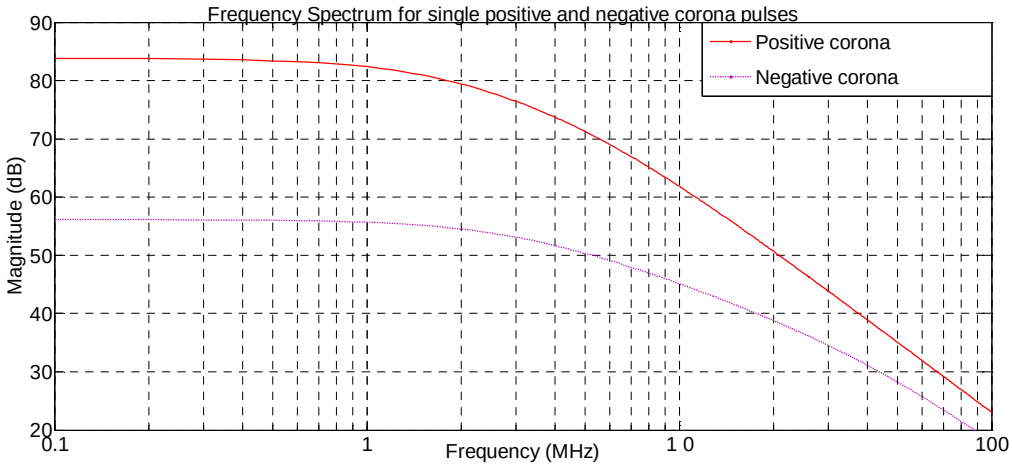

Figure 2-2: Frequency spectra for single corona current pulses (from equation 2.5)

It can be seen that the positive corona spectrum starts to decrease rapidly after 2 MHz while that of negative corona rapidly falls off beyond 10 MHz. The positive corona also has a higher magnitude, which makes it the dominant source of EMI on power lines.

EMI due to corona is most prevalent on high voltage transmission lines as compared to that from distribution lines since corona intensity reduces with the line voltage. Distribution lines operating at low voltages even up to 66 kV, with normal conductor sizes, have very low operating gradients typically about 6 or 7 kV/cm. This is insufficient to support the air breakdown process of conductor corona noise sources [27]. Corona will be more pronounced on transmission lines, which on South Africa's power line network operate from 132 kV and above. MeerKAT facilities and its predecessor, KAT, will be supplied from a 22/33 kV distribution power line. Under these low voltages, corona activity will be too low to cause significant interference. It is suggested in [21] that at voltage levels of less than 200 kV, corona noise is usually too small to cause EMI at frequencies above 30MHz. However, at these low voltages, corona sources can still occur at discrete points such as on insulators and also at sharp points left on the conductors and other hardware. This could be due to poor construction practices or the presence of debris, such as small pieces of wire, on the line [28].

2.2.3 Sparking noise generation

Gap-type discharge, unlike the corona discharge, is a complete electrical breakdown of insulation between two surfaces, which are charged to different potentials, on high voltage power-line hardware [29]. This occurs when at least two charged components become electrically separated by a small gap. The surfaces forming the gap may be two metallic electrodes or a metallic electrode and a non-metallic material. At least one of the electrodes is capacitively coupled to a voltage source or to the ground [29]. These gap discharges can be categorized into sparking, micro-sparking, and surface discharges on insulators [30], [31]. Micro-sparking results from a very small spark, as small as 0.02 mm, while sparking results from electrical breakdown between two conducting parts that are separated by a gap that is as small as a fraction of a cm or up to 20 mm long [30].

The insulation within the gap, which could be air, dielectric, or any other non-conducting medium, gets ionized when sufficient potential difference exists between the surfaces. If the potential difference is in excess of the insulation's critical voltage, the resulting ionization reduces the insulation resistance until it is enough to support conduction and a complete breakdown occurs [11]. With the insulation turned into a conductor, a large avalanche of current then flows through the ionized channel in the form of a spark discharge. This results in the potential across the gap between the two surfaces being temporarily diminished and the spark is stopped. The breakdown is extinguished for a short time before the potential across the gap starts to increase again to the breakdown point, thus generating another spark.

Since the power line voltage has a fundamental 50-Hz waveform, this discharge process is repeated until the line alternating voltage decreases to the point where it can no longer support the breakdown process [11], [30]. This repetition is determined by the time the capacitively coupled electrode requires to get charged to a threshold voltage and this depends on the gap size and the reactance of the gap charging source [11]. This process can occur on both positive and negative polarities of the AC power supply giving a pulse group repetition rate of

100 per second. A train of impulse-type current waveforms on each half-cycle of the power frequency could be produced in the process and is concentrated near the peaks of the 50-Hz waveform. The pulse trains could consist of one or more pulses and the number could be similar or different on both polarities of the line voltage waveform, as typically illustrated in Figure 2-3.

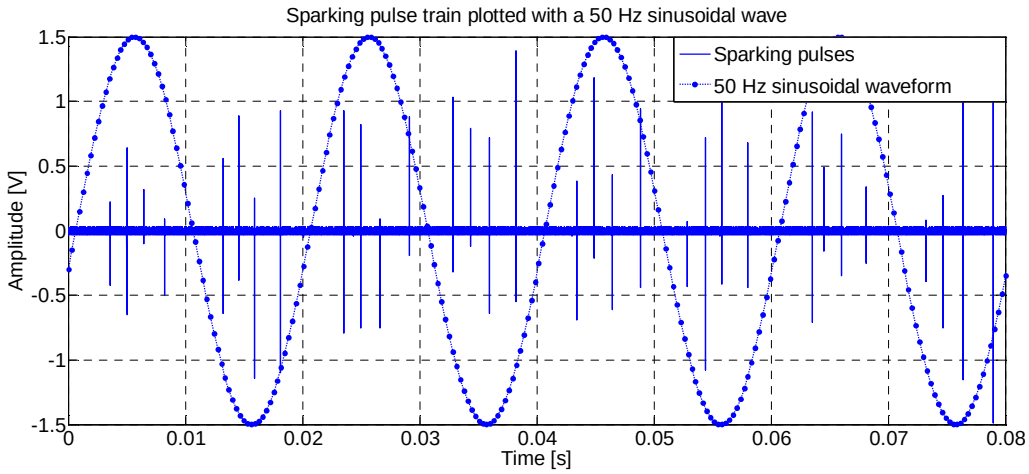

Figure 2-3: A typical illustration of the relationship between a sparking pulse train and a 50 Hz sinusoidal waveform

2.3 Examples of sparking noise sources

Sparking noise, as mentioned in the previous section, is caused by electrical breakdown of insulation across small gaps formed by two closely spaced electrodes that are charged to different potentials. The electrodes involved in sparking could be a guy wire, a loose nut, a corroded wire on the line, or a loose clamp or connection on a power line device. The gaps are most commonly found on loose, unbonded and/or corroded hardware on distribution wooden-structured power lines [21]. A typical distribution power line pole has several items of hardware such as that given in Figure 2-4a and some of these components can be sources of sparking discharges.

The line hardware that has been found to cause severe EMI includes bell insulators, loose hardware and defective lightning arresters [30]. The loose hardware could be a loosened cross-arm bolt causing a small gap to occur between the bolt head and the washer or at the other end between the nut and its corresponding washer [11]. A small gap can also arise between a ground wire and a loose cross-arm brace or loose bond between ground wires and staples used to fasten these wires to the poles. Other major sources are insulated tie wires on either bare or insulated conductors and bare tie wires on insulated conductors, arcing between inadequately spaced and unbonded metal components such the ground wire and the cross-arm bolt shown in Figure 2-4b, and improper termination of high voltage cables at underground to overhead line transitions.

Aging wooden-structured power line poles, and also the shrinking and swelling of these poles due to change of weather conditions can make the bolts, nuts and washers used to fasten other line hardware, such as cross-arms and insulators, loosen, creating small gaps resulting in sparking. Metallic debris thrown onto the line conductors may form intermittent contacts with the lines which could create erratic sparking especially if the contact becomes corroded.

Similarly, poor contact at slack spans, where there are insufficient weights to prevent the formation of small gaps or formation of oxidation on metal contact surfaces can also cause spark discharges. These can be found on air gaps formed between the cap and pin of lightly weighted suspension insulators strings on transmission lines [16]. Voids found on broken porcelain insulators have also been found to cause spark discharges [21].

(a) (b)

Figure 2-4: (a) typical hardware on a distribution power-line pole (b) unbonded ground-wire to cross-arm bolt connection

2.4 Sparking noise characteristics

The EMI from sparking noise sources can be represented by its frequency spectrum, which is the change in the noise magnitude level with frequency [19]. This is usually given in terms of either μV or μV/m (or their dB values above 1μV or 1μV/m) [19]. The frequency spectrum is dependent on the time domain characteristics of the current pulses, which include the pulse rise time, duration and repetition characteristics [21].

2.4.1 Time domain properties of sparking current pulses

Like the corona current pulses, the general shape of a current pulse generated by sparking gap discharges can be approximated by a double exponential function which can be represented as follows [19]:

$$I(t) = KI_p\left(e^{-\alpha t} - e^{-\beta t}\right), \qquad t \geq 0 \qquad 2\text{-}6$$

where K, α and β are empirical constants which are determined through the knowledge of pulse rise time and pulse duration [32], I_p is the current amplitude in mA and t is time in nanoseconds (ns). The typical average parameters defining these sparking current pulses, i.e. the amplitude, rise time and pulse length, are given in Table 2-2 together with the pulse repetition rate [21].

Table 2-2: Typical sparking current pulse parameters [21]

Current Amplitude (mA)	**Rise Time (ns)**	**Duration (ns)**	**Repetition rate (Pulses/s)**
500 – 2000	1	5	$10^2 – 5.10^3$

Comparing these parameters with those given in Table 2-1 shows that the sparking current pulses have higher amplitudes with shorter rise time and duration than those of corona pulses. A typical time-domain representation of a sparking pulse can be written as follows [24]:

$$I(t) = 2.334 I_p (e^{-0.51t} - e^{-1.76t}) \qquad 2\text{-}7$$

which when plotted with a current amplitude of 1 A is as shown Figure 2-5.

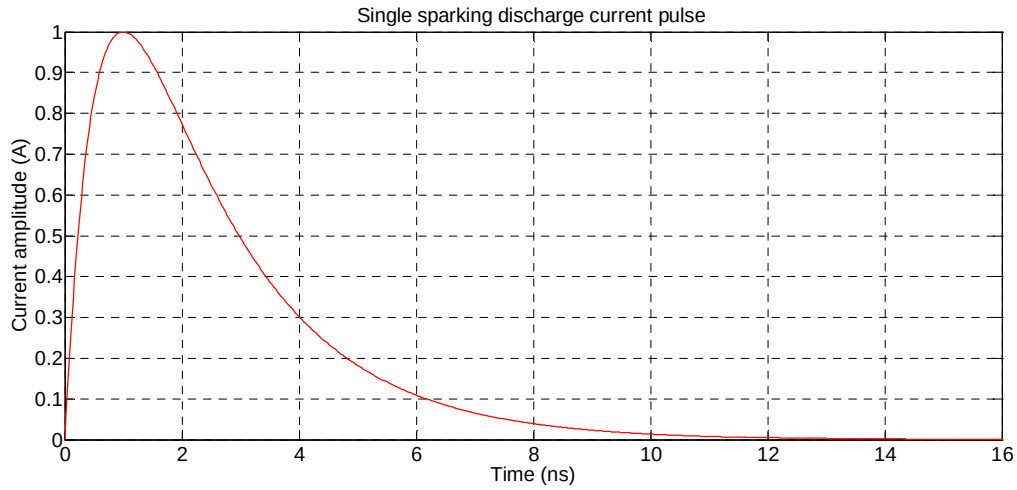

Figure 2-5: A typical current pulse produced by a sparking discharge (after [24])

2.4.2 Frequency spectrum for sparking discharges

As was shown in section 2.2.2.2 that the frequency domain representation of a pulse can be obtained through the Fourier transformation of its time domain, the frequency domain for a sparking pulse given in equation 2-7 can be represented as follows [24]:

$$F(\omega) = \int_{-\infty}^{\infty} KI_p\left(e^{-\alpha t} - e^{-\beta t}\right).e^{-j\omega t}.dt$$

$$= KI_p \frac{\beta-\alpha}{\alpha\beta+j\omega(\alpha+\beta)-\omega^2} \qquad 2\text{-}8$$

This also gives a magnitude, in dB, for a single sparking pulse, as:

$$|F(\omega)| = 20log_{10}\left[KI_p \frac{\beta-\alpha}{\sqrt{(\beta^2+\omega^2)(\alpha^2+\omega^2)}}\right] \qquad 2\text{-}9$$

Equation 2-9 gives the typical frequency spectrum, given in Figure 2-6, which also shows the spectra for the positive and negative corona pulses as were plotted in Figure 2-2. The three graphs are plotted with typical current amplitudes of *1000 mA*, *100 mA* and *10 mA* for the sparking, positive corona- and negative corona pulses, respectively.

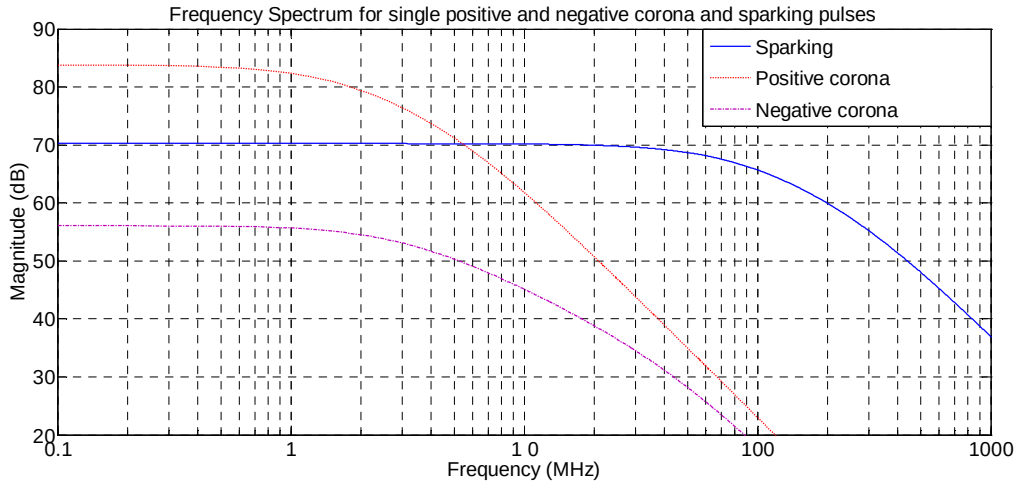

Figure 2-6: Typical frequency spectra for corona and sparking current pulses

From equation 2-9, the maximum magnitude of the spectrum is reached when ω = 0. This results in a spectrum that is dependent on the product of the pulse amplitude and the pulse duration [21]. At low frequencies, including ω = 0, when ω << α or β, the value of $|F(\omega)|$ varies as $KI_p\frac{\beta-\alpha}{\alpha\beta}$ which is independent of the frequency [19]. This magnitude will remain constant as the frequency increases until when ω = α then it start to decrease inversely proportional to the frequency. At high frequencies when ω >> α or β, $|F(\omega)|$ varies inversely proportional to ω^2. This variation in magnitude of the frequency spectrum can be summarized as follows [24]:

$$|F(\omega)| = 20log_{10}\left[KI_p\frac{\beta-\alpha}{\alpha\beta}\right],\ \ \omega \ll \alpha \text{ or } \beta \qquad 2\text{-}10$$

$$|F(\omega)| = 20log_{10}\left[KI_p\frac{\beta-\alpha}{\sqrt{2}\beta\omega}\right],\ \ \omega = \alpha, \omega \ll \beta \qquad 2\text{-}11$$

$$|F(\omega)| = 20log_{10}\left[KI_p\frac{\beta-\alpha}{\sqrt{2}\omega^2}\right],\ \ \omega \gg \alpha, \omega = \beta \qquad 2\text{-}12$$

$$|F(\omega)| = 20log_{10}\left[KI_p\frac{\beta-\alpha}{\omega^2}\right],\ \ \omega \gg \alpha \text{ or } \beta \qquad 2\text{-}13$$

From these equations, the critical frequencies that determine this spectrum variation are given by $f_\alpha = \frac{\alpha}{2\pi}$ and $f_\beta = \frac{\beta}{2\pi}$ which for the sparking discharge pulse given in equation 2-7, would be around 80 MHz and 280 MHz, respectively.

Figure 2-6 has shown that at low frequencies both positive corona and sparking noise are the major source of EMI. Due to the dependence of the amplitude of the spectrum on the pulse amplitude, the contribution of negative corona on the overall EMI is minimal. At the higher frequencies, beyond about 10 MHz, sparking noise is the main EMI source. Essentially, this plot suggests that the sparking noise is constant over a wider frequency range, while the corona noise decreases rapidly with increasing frequency. This is in line with the prediction given in Figure 2-7 which was obtained from calculations using empirical formulae developed

by CIGRE for high voltage transmission lines [31]. This spectral plot shows that the radiated sparking noise extends up to about 100 MHz, when measured near the source at x = 0, after which its field strength starts to decay rapidly. In these plots the line is assumed to be oriented along the x-axis.

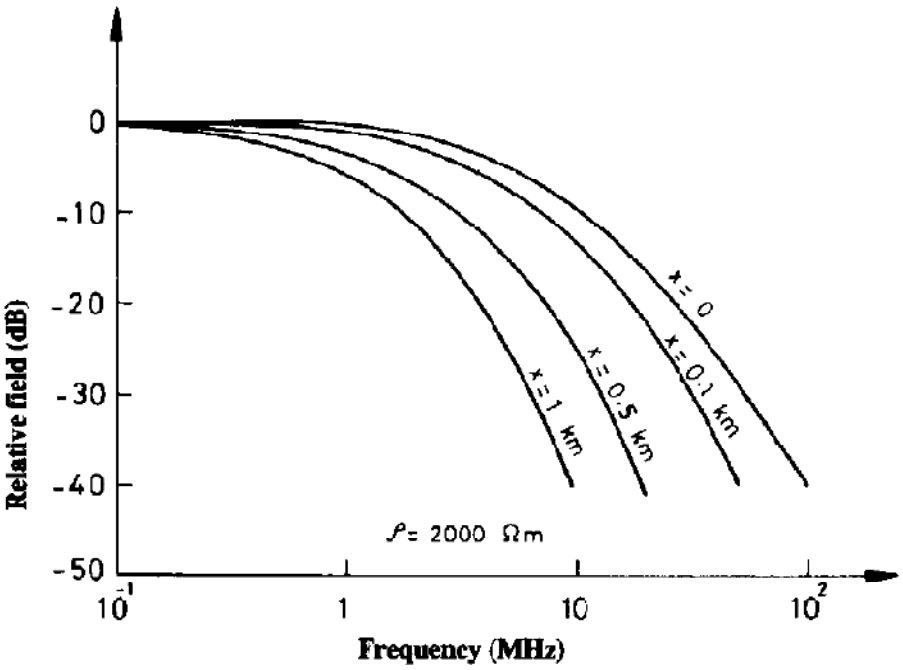

(a)

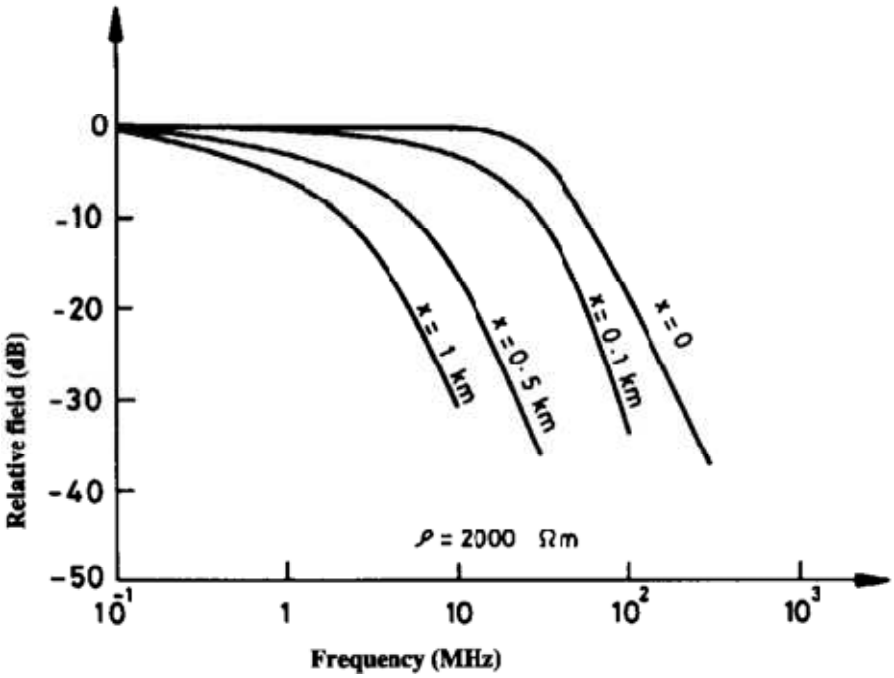

(b)

Figure 2-7: Typical frequency spectrum found in current literature for (a) corona and (b) sparking noise relative field strength [31]

2.4.3 Frequency spectrum observations from measurements in the literature

Malik and Al-Arainy [28] carried out laboratory measurements to compare the frequency spectra of radiated EMI from sources that simulated corona at sharp points, contaminated insulator discharges, and gap discharges. The gap discharge source utilized a point plane geometry having a gap of 1 mm while the corona discharge was from a 20-mm point-plane gap. The measured spectra, given in Figure 2-8, which were taken with an antenna placed about 5 m from the sources, shows the gap discharge source to have a relatively flat and wide frequency spectrum. The frequency spectra from the corona source and that from the post-type, dry, and contaminated insulators decrease significantly with increasing frequency.

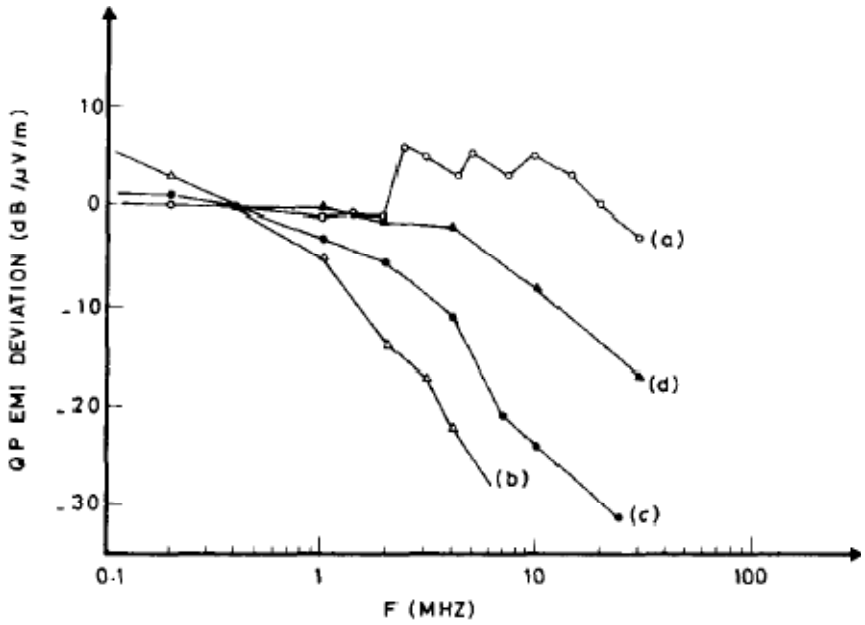

Figure 2-8: Laboratory radiated EMI measurements of frequency spectra from (a) gap discharge source (b) average of all weather EMI spectra measured for distribution lines (c) corona discharge source (d) contaminated insulator [28].

Pakala and Chartier [12] conducted various radio noise measurements on twenty-two AC overhead power lines rated between 2.4 kV and 735 kV and on an 800-kV DC test line in the frequency range of 60 Hz to 10 GHz. This exercise involved measuring both corona and sparking interferences. In this set of tests, the measurements taken from a natural gap source occurring on a distribution line, given in Figure 2-9, extend the above theoretically predicted frequency spectrum to a breakpoint of perhaps a few hundred MHz. The natural source here was a sparking discharge between a pole guy wire and a neutral conductor on a 12.5 - 34.5 kV dual line. The measurement position is reported as being 15 m from the outer phase conductor. The spectrum given in Figure 2-9 was also compared in [12] with a corona noise spectrum from a 345-kV line. It was found that above a frequency of about 1.6 MHz the EMI from the gap source has a much higher noise level than that from the 345-kV line conductor corona. The spectrum from the gap source was observed to be much flatter than that for the 345-kV line corona noise.

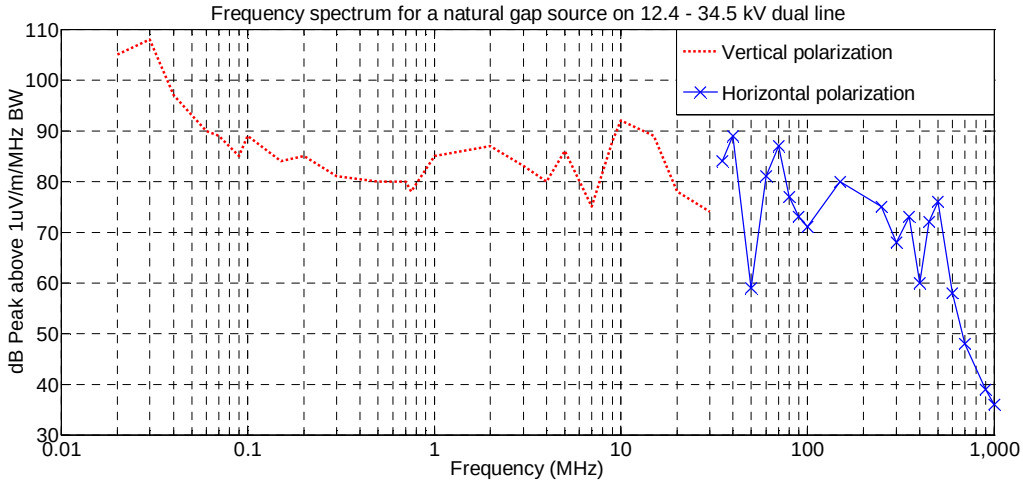

Figure 2-9: Frequency spectrum of a natural gap source on a power line (adapted from [12]).

Another measurement taken by [12] for a frequency spectrum of a natural gap source occurring on a wooden pole between a cross-brace floating hardware and the vertical ground wire on a 345-kV line showed the trend given in Figure 2-10. It is also reported that the measurements were taken at a lateral distance of about 60 m from an outer phase conductor. The shape of this spectrum was found to be similar to that for the low voltage line given in Figure 2-9. It can be noted that the spectrum remains relatively constant between the frequencies of 200 kHz and 30 MHz beyond which it rolls off with an inverse proportionality to the square of frequency or 20 dB per decade of frequency.

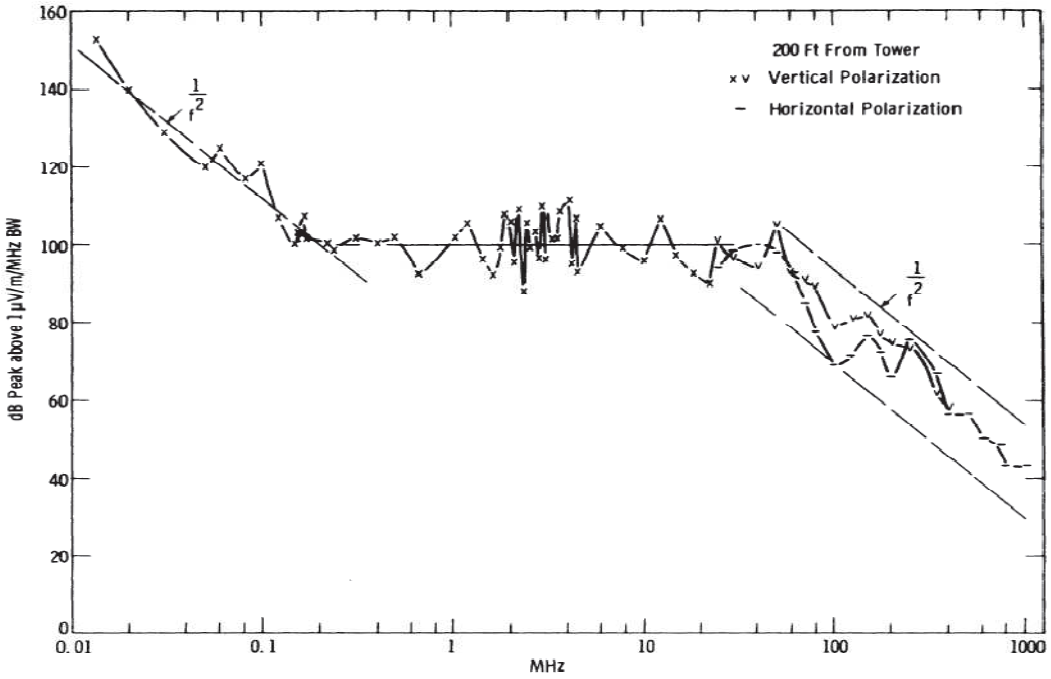

Figure 2-10: Frequency spectrum for a natural gap source on a wooden tower of a 345 kV horizontal configuration line [12]

German [13], [33] investigated the radiated gap discharge from various sources on a low voltage test line. In one of the measurements carried out using a log conical spiral antenna with a 14 kHz – 1 GHz Fairchild Electro-Metrics Interference Analyzer Model EMC-25 in the frequency range of 500 to 1000 MHz showed a radiated frequency spectrum given in Figure 2-11. Here, the radiation was from a 0.762 mm spark-gap discharge between a zinc-coated insulator pin and a grounded zinc-coated bolt on a 6.9-kV 3-pole test line. The antenna was about 1.8 m above the ground and placed at about 15 m laterally from the centre conductor. From this spectrum, the radiated field strength exceeds the ambient noise up to about 1 GHz, beyond which it becomes undetectable above the noise floor level. This was one of the widest radiated spectra obtained in these and other surveyed measurement results obtained from the literature. It is necessary to examine the behaviour of the radiated frequency spectra of this sparking noise in the frequencies beyond 1 GHz.

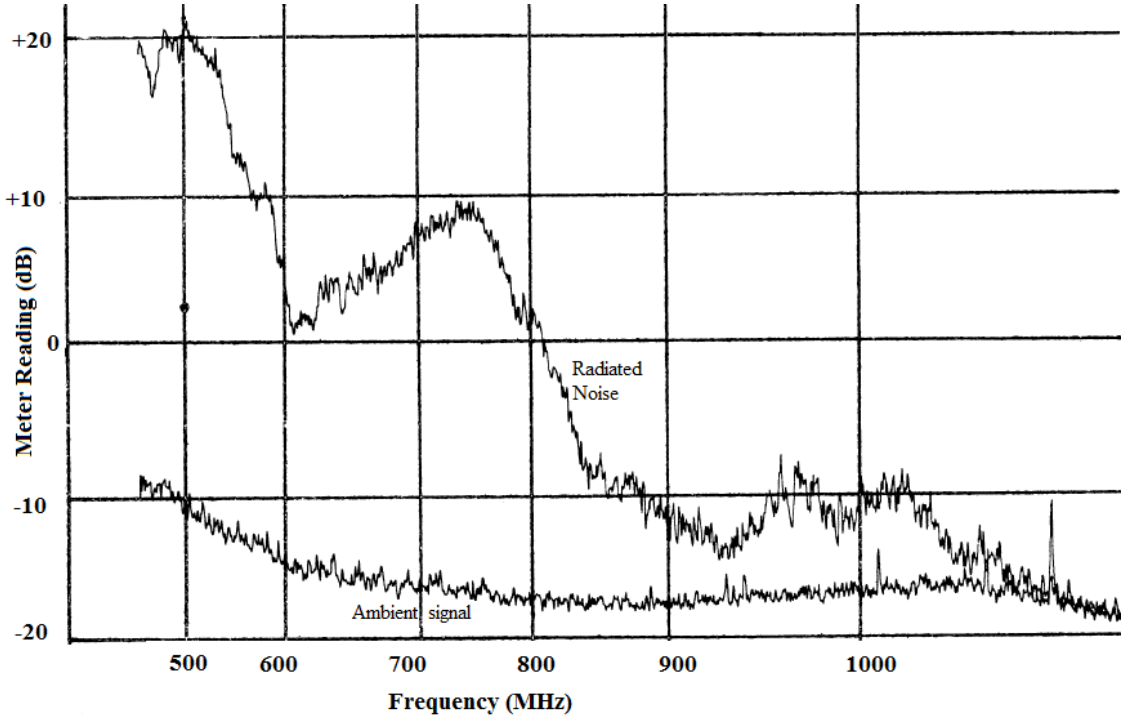

Figure 2-11: Radiated frequency spectrum from a 0.762 mm spark discharge between a zinc-coated insulator pin and a grounded zinc-coated bolt on a 6.9-kV 3-pole test line [13].

2.5 Conclusions

In this chapter, the existing literature on power-line interference characteristics, measurement methods, and possible noise sources with an emphasis on the sparking noise was explored. This survey forms the basis for further investigation of the characteristics of sparking noise such as its radiated spectral behaviour in the higher frequency band, which was found to extend only up to about 1 GHz.

Chapter 3

Sparking noise measurement setup and procedures

3.1 Introduction

To investigate and quantify the key characteristics of power-line sparking noise, radiated measurements were performed at various environments. These environments include a high-voltage laboratory (HV-Lab), a 40 m test-line, and an approximately 1.5 km of 22-kV test-line. In all these cases, an artificially made spark-gap device was used as a sparking noise generator where it was mounted on one of the energized line conductors. This artificial gap is used to simulate the natural gaps occurring on the lines. The important parameters considered were the frequency spectrum and time domain characteristics of the radiated noise. The frequency spectrum data were used to determine the lateral, height and longitudinal profiles of the noise while the time domain results were used to establish information concerning the pulse shape and repetition rate of the discharge pulses generated. These results can be used in identifying sparking sources for diagnostic purposes as well as helping in developing test and fault finding procedures. The conducted sparking noise measurements were also carried out to evaluate the time domain characteristics in comparison with the radiated noise patterns. A description of the measurement setups and procedures used in these evaluations is provided in this chapter.

3.2 Instrumentation

Sparking RF radiation measurements were derived from an artificially made spark-gap test structure shown in Figure 3-1, which consisted of two cylindrical electrodes whose tips were hemispherically shaped. One of the electrodes is connected to the high voltage line and the other is a floating passive electrode. This spark-gap structure permits fine adjustment of the gap spacing by moving the active electrode up and down. The floating electrode is attached to a metallic sphere, which is capacitively coupled to the ground potential. This structure simulates the metal-to-metal gap, which could occur on loosely bonded or closely spaced parts of power line hardware. This can happen in a situation such as loose tie wires on insulators where the wire and the line conductor have poor contact and since the wire is not grounded, it acts as floating electrode.

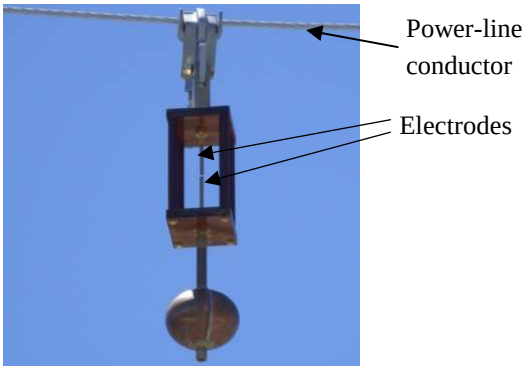

Figure 3-1: Spark-gap device mounted on power line conductor

Various measuring devices can be used to measure the radiated sparking noise from power lines. These devices have to be capable of appropriately identifying and distinguishing between power-line generated noise and other kinds of noise. They should also be sensitive enough to measure the power-line noise well above their system noise floor levels. These devices can be classified into frequency domain and time domain categories, and they are usually used in conjunction with antennas to obtain the radiated emission data.

3.2.1 Antennas and/or field probes

Antennas and field probes are the main devices on the front end of a measuring system used to measure the radiated sparking noise emissions from power lines. There are many types of antennas that can be used for this purpose. The type of antenna to be used is mainly dependent on the noise frequency to be measured. These antennas have different characteristics including their bandwidths and gains. Since sparking from power lines emits a very wideband noise, it is difficult to find a single antenna that operates in that entire bandwidth and hence several antennas would be required to cover the desired frequency range.

Rod antennas and loop/magnetic field coils are widely used for measurements at frequencies below 30 MHz. Measurements done by Pakala *et al* [12] in the frequency range from 10 kHz to 10 GHz used a vertical rod antenna from 10 kHz to 25 MHz. The loop antennas detect the magnetic component while the rod antennas measure the electric component of the electromagnetic field. The loop antennas are preferred for this frequency range since measurements are mostly in the near field and magnetic fields are not easily disturbed by the presence of nearby objects including people [34].

At frequencies above 30 MHz, dipole, biconical, log periodic dipole arrays (LPDA), bilog, horn and parabolic reflector are some of the antennas that are often used. Most of these antennas are broadband and directional. In many cases, the aim of gap noise measurements is to locate the noise source to carry out correction procedures, and these antennas are valuable. This is because the high frequency components of the noise are attenuated more rapidly as they propagate down the power line as compared to the low frequency components [12]. The broadband antennas would then be useful in evaluating this field strength attenuation. Examples of such applications include those performed by [12] who utilized horn and parabolic reflectors and [35] who used the VHF/UHF log periodic and Yagi-Uda antennas.

Measurement receivers are calibrated to record data that they detect at their 50 Ω input in either dBm or dB above 1 μV. The latter is commonly used for radiated noise emission

measurements as it can readily be converted to electric field strength limits. This requires that the antenna to be used has to be calibrated to obtain its antenna factor. This factor relates the incident electromagnetic field to be measured at a point where the antenna phase centre is located and the voltage on a 50 Ω load connected to the antenna [36]. This can be represented in an equation form as [34]:

$$E_{(dB\mu V/m)} = V_{(dB\mu V)} + AF_{dB/m} \qquad 3\text{-}1$$

where E is the electric field, V is the receiver reading, and AF is the antenna factor.

The results presented in this dissertation were obtained using various antennas. A 60 cm diameter R&S HFH2-Z2 magnetic loop antenna (see Figure 3-2a) with operational band of 9 kHz – 30 MHz was used in some of the sites. This antenna has a battery-powered preamplifier that helps in matching the low loop antenna impedance to the 50 Ω impedance of the measurement receiver. Also due to the loop antennas' frequency-sensitivity, the preamplifier ensures that the response across its entire wide bandwidth is measured with a constant antenna factor of 20 dBm^{-1}. A dipole antenna with a frequency range of 25 MHz – 80 MHz and a vertical resistively loaded monopole antenna of 30 MHz – 300 MHz (see Figure 3-2b) were also used. Their antenna factors are as given in Figure 3-3a and Figure 3-3b, respectively.

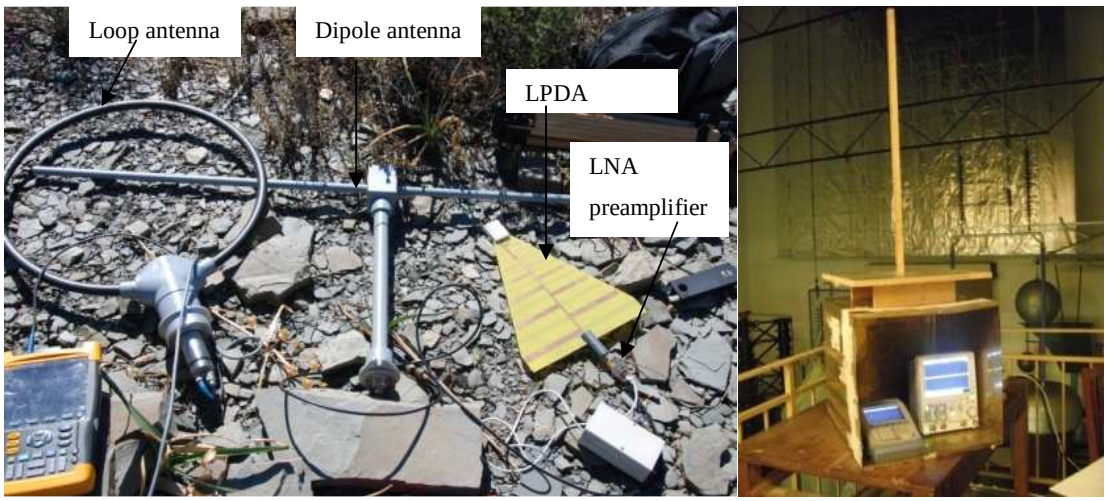

(a) (b)

Figure 3-2: (a) Loop, dipole and LPDA antennas used in the measurements (b) vertical resistively loaded monopole antenna

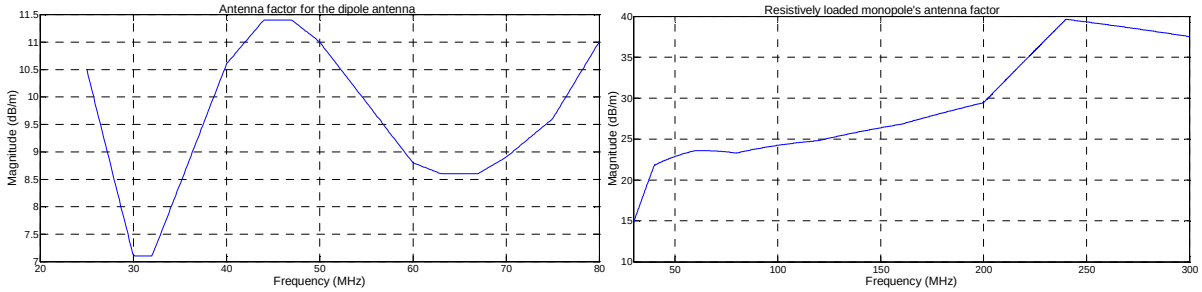

(a) (b)

Figure 3-3: Antenna factors for (a) Dipole antenna (b) vertical resistively loaded monopole antenna

An antenna for sparking noise measurements at frequencies above 300 MHz was not originally available. Three identical LPDA antennas were designed and characterized in an anechoic chamber. Their characterization involved measuring their gains with an HP8510C vector network analyzer (VNA). A one-path two-port calibration was first performed on the VNA to correct for systematic errors and to set the reference plane at the connectors where the antennas would be connected. The three-antenna gain calibration method was then done by taking three S_{21} measurements using all combinations of the antennas. The S_{11} of each antenna was also measured. During this process, the antennas were aligned for boresight radiation at 2 m above the ground and each placed 5 m apart to ensure that they were in the far-field region.

With the use of the Friis transmission formula given by (3-2), the results were then used to calculate the gain of each antenna [36].

$$\frac{P_r}{P_t} = G_i G_j \left(\frac{\lambda}{4\pi R}\right)^2 \qquad 3\text{-}2$$

where P_r is the power received in Watts, P_t is the power accepted by the transmitting antenna in Watts, λ is the wavelength in metres, R is the antenna separation distance in metres, and G_i and G_j are the numeric power gains of two antennas used in a given set of measurements. Since the S_{21} in dB is essentially the power ratio given in (3-2) as $\frac{P_r}{P_t}$, the antenna gains are then calculated using the following equations:

$$G_{A\,dB} + G_{B\,dB} =$$

$$20log_{10}\left(\frac{4\pi R}{\lambda}\right) + S_{21(1)dB} - 10log_{10}\left(1 - |S_{11B}|^2\right) - 10log_{10}\left(1 - |S_{11A}|^2\right) \quad 3\text{-}3$$

$$G_{A\,dB} + G_{C\,dB} =$$

$$20log_{10}\left(\frac{4\pi R}{\lambda}\right) + S_{21(2)\,dB} - 10log_{10}\left(1 - |S_{11C}|^2\right) - 10log_{10}\left(1 - |S_{11A}|^2\right) \quad 3\text{-}4$$

$$G_{B\,dB} + G_{C\,dB} =$$

$$20log_{10}\left(\frac{4\pi R}{\lambda}\right) + S_{21(3)\,dB} - 10log_{10}\left(1 - |S_{11C}|^2\right) - 10log_{10}\left(1 - |S_{11B}|^2\right) \quad 3\text{-}5$$

where the cable losses have been accounted for in the S_{21} given in 3-3 to 3-5. The antenna mismatch has also been accounted for by including the reflection coefficient of each antenna in the equations. This system of equations can be re-written as;

$$G_{A\,dB} = \frac{GAB+GAC-GBC}{2} \quad 3\text{-}6$$

$$G_{B\,dB} = \frac{GAB+GBC-GAC}{2} \quad 3\text{-}7$$

$$G_{C\,dB} = \frac{GAC+GBC-GAB}{2} \quad 3\text{-}8$$

where $GAB = G_{A\,dB} + G_{B\,dB}$, $GAC = G_{A\,dB} + G_{C\,dB}$, and $GBC = G_{B\,dB} + G_{C\,dB}$. The antenna factors would then be calculated as

$$AF_{A\,dB} = 19.765 - 20log_{10}(\lambda) - G_{A\,dB} \quad 3\text{-}9$$

$$AF_{B\,dB} = 19.765 - 20log_{10}(\lambda) - G_{B\,dB} \quad 3\text{-}10$$

$$AF_{C\,dB} = 19.765 - 20log_{10}(\lambda) - G_{C\,dB} \quad 3\text{-}11$$

Using equations 3-6 to 3-11, the antenna gains were found to average about 5.5 dB across the design frequency band of 300 MHz – 6 GHz. Figure 3-4 shows the antenna factor for the antenna that was used to conduct most of the measurements above 300 MHz.

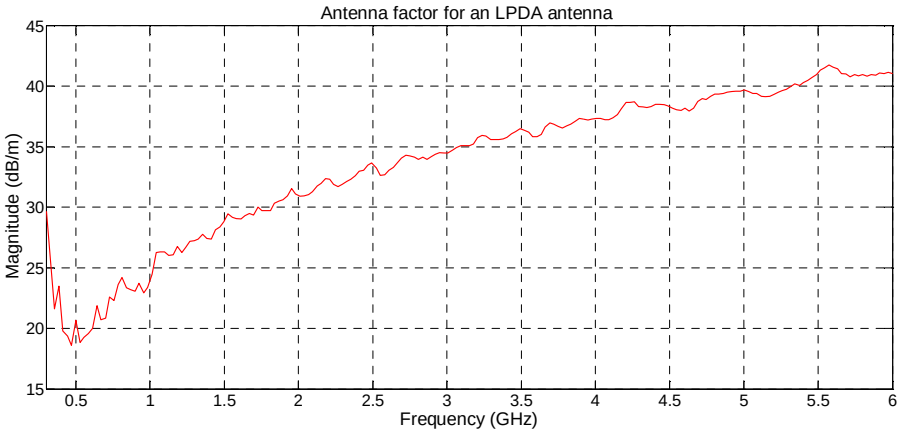

Figure 3-4: Antenna factor for an LPDA antenna

3.2.2 Frequency Domain Measurement system

The frequency domain characteristics of power-line EMI can be measured using either frequency-selective EMI receivers or spectrum analyzers. These instruments are preferred over radio noise meters since the latter only allow measurements at a single frequency [37].
The EMI receiver is also a narrowband super-heterodyne receiver whose output, though mostly provided at a spot frequency, can be swept through a wide range of frequency points. It also has better sensitivity compared to a SA [34].

The SA is also a heterodyne receiver in which the appropriately attenuated output signal from the antenna is fed directly into a continuously tunable local oscillator that is swept in time across a certain frequency band and the resultant signal converted to a lower, fixed intermediate frequency (IF) [38]. This wide input frequency range makes the analyzer suitable for use in wideband type of measurements. The output of the IF filter is then fed to a detector circuit. The magnitude levels of spectral components of the input signals that fall within the bandwidth of that filter are processed and displayed mostly in a logarithmic scale calibrated in

dB. This process is illustrated by Figure 3-5 [21]. The detectors mostly found in spectrum analyzers include minimum peak, maximum peak, auto peak, sample detectors and sometimes average and RMS detectors [39]. The maximum peak detector allows the maximum value of the encountered signal at any given frequency point during multiple sweeps to be displayed [21]. This is commonly referred to as Max Hold or peak hold trace mode. Due to the multiple sweeps and regardless of the desired frequency band being much greater than the set RBW, most of the important information is recorded. The maximum spectrum level reached is retained in each trace over a period of time and this is particularly useful is cases where there is erratic and intermittent sparking noise.

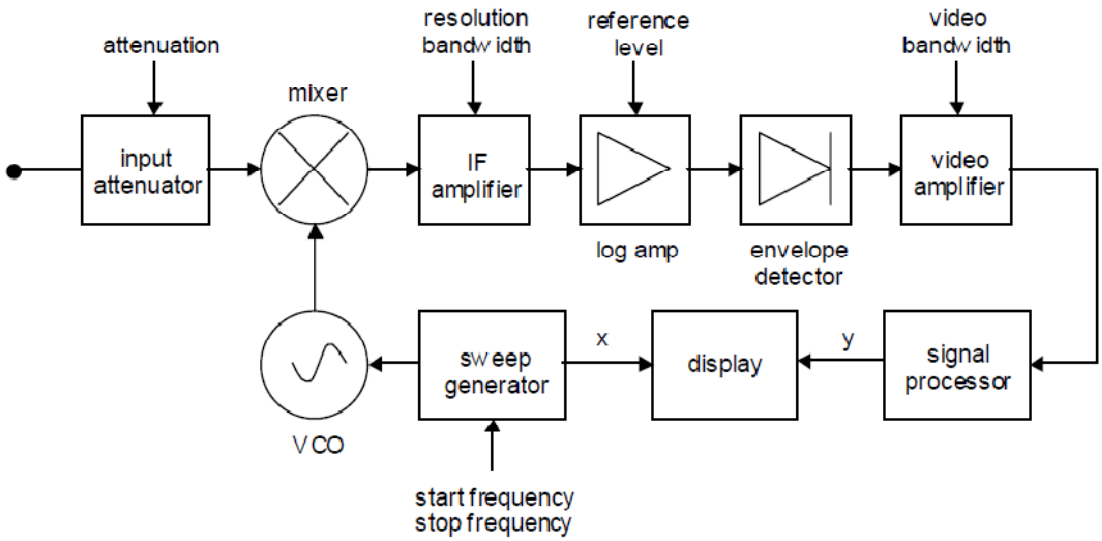

Figure 3-5: A block diagram of a typical spectrum analyzer [34,40]

Since the sparking noise is a highly impulsive type of noise, the SA settings have an influence on its displayed power levels. The displayed noise level increases with an increase in the IF filter's bandwidth, the RBW [34]. This is illustrated by equation 3-12 where the displayed average noise level is a function of varying RBW.

$$\Delta N_{(dB)} = 10log_{10}\left(\frac{RBW_2}{RBW_1}\right) \qquad 3\text{-}12$$

where RBW1 and RBW2 are the analyzer's RBWs before and after variation, in Hz, and ΔN is the difference in displayed noise level as a function of varied RBW, in dB.

A wider RBW would capture much of the noise input since the spectral components of this noise occupy a wider bandwidth than that of the analyzer. However, the sensitivity of the analyzer would reduce due to its noise floor being increased. In addition, a wider RBW would miss the narrowband signals occupying portions of the desired frequency band. A compromise would therefore be necessary in choosing the RBW to be used while taking spark-gap noise measurements.

A hand-held battery operated SA, FSH3 (100 kHz – 3 GHz), and in some cases FSH8 (9 kHz – 8 GHz) and FSH4 (9 kHz – 3.6 GHz) spectrum analyzers were used to make frequency domain measurements. These FSH spectrum analyzers are manufactured by Rodhe & Schwarz.

3.2.3 Time Domain Measurement system

An oscilloscope can be used to take time domain measurements of sparking noise originating from power lines. It can be used for analyzing pulse noise characteristics such as rise time, shape and repetition rate. The measured single pulse data can be Fourier transformed to extract the noise frequency spectrum. Since the frequency spectrum is dependent on the measured rise time, and the sparking noise is broadband in nature, the oscilloscope's bandwidth should be wide enough to ensure that this pulse rise time is measured correctly. If not, the oscilloscope's bandwidth will limit the highest frequency components which can be detected, i.e. the higher frequency components of the measured signal will be filtered out. This can be illustrated by the following expression, which relates the oscilloscope bandwidth to the pulse rise time that it can display [41]:

$$t_r \cong \frac{K}{BW} \qquad 3\text{-}13$$

where t_r is the pulse rise time, BW is the oscilloscope bandwidth, and K is a constant of proportionality, which depends on the exact pulse shape. Theoretically, for a Gaussian response system, this constant, K ≈ 0.339, however, it is usually taken by the industry as K = 0.35 [42].

In the time domain measurements undertaken here, broadband antennas were used with a Yokogawa DLM2052 oscilloscope, which features an analog bandwidth of 500 MHz, up to 2.5 GS/s of sampling rate, and up to 62.5 MPoints of record length. Adapting from [42], typically, to measure a pulse with 1 ns rise time to an accuracy of 10%, using a Gaussian response oscilloscope, requires at least 455 MHz of bandwidth and 1.82 GS/s of sampling rate (the latter is to avoid sampling-alias errors). For more accurate, faster pulse rise times, these values need to be higher. The sensitivity of the DLM2052 oscilloscope used, at the DC coupling for 50Ω input, is 20 mV/div and its lowest time resolution is 1ns/div. The R&S FSH4 SA was also used to make time domain measurements. This was done by setting the SA to zero-span mode at the centre frequency of interest. The zero-span mode has the added advantage of measurement sensitivity as the RBW can be narrowed to exclude broadband noise.

3.3 Measurement environments, methods and procedures

3.3.1 High Voltage Laboratory investigations

The laboratory tests to characterize the sparking noise, presented in this dissertation were conducted in a high voltage laboratory environment at the University of Stellenbosch. The test structure was attached to a 2 m long rod, as shown in Figure 3-6a, which was connected to an AC voltage source and raised about 7 m above the ground. This laboratory environment is not electromagnetically shielded and due to the presence of various metallic components, the radiated noise measurements would be affected by reflections from these metallic parts. Also common mode currents flowing on the outer surfaces of the measurement cables used

can be conducted onto the measuring receivers. To reduce this interference, an EMC cabinet was used to house the measuring equipment as shown in Figure 3-6b. The cabinet has a power filter to minimize conducted noise, which can also enter the AC powered oscilloscope used through the power supply cord. Properly shielded coaxial cables were used between the antennas and the input of the cabinet. A coaxial bulkhead connector was used at the input of the EMC cabinet to reduce EMI current and voltage on the cable shield getting into the measuring instruments.

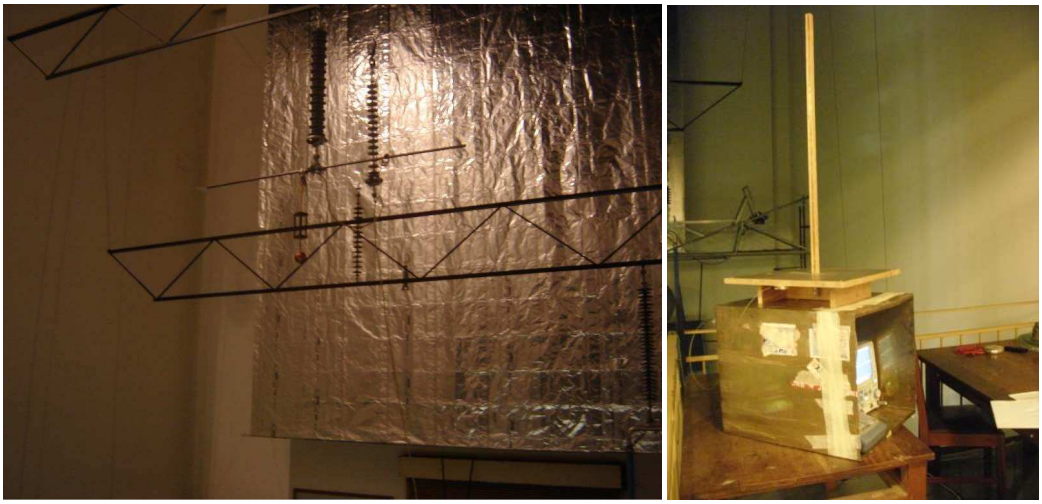

(a) (b)

Figure 3-6: (a) High voltage laboratory measurement setup (b) EMC cabinet with measuring equipment

3.3.2 Measurements on short test-line

Another location where radiated electromagnetic fields from induced sparking currents onto, and propagated by transmission lines were measured, is a short test-line. This line, due to its close availability at the University of Stellenbosch, was used to refine measurement procedures and carry out extensive noise characterization. The line has three phase conductors in an open area, it is about 40 m long, 7 m above the aluminium-painted, bitumen roof, and all the three line conductors are open circuited at both ends. During the measurements, a step-up

single-phase transformer, rated at 30 kV_{rms}, was used to energize the middle line conductor on one end, as shown in Figure 3-7a. The other end of the line was either left open or grounded through a series surge-impedance termination of 375 Ω resistor (4 resistors of 1.5 kΩ in parallel) and a high-voltage capacitor of 1.2 nF.

The spark-gap is attached at the centre of this middle conductor and the properties of the radiated noise were measured as depicted in Figure 3-7b. A variable voltage controller is used to adjust the AC voltage level applied to the spark-gap. The frequency and time domain properties of radiated sparking noise are measured approximately 10 m laterally away from the line. The measurements showed no difference when the line was either open-circuited or terminated. This is likely because the line is situated on the roof of a two-floor building and the reference grounding termination, two floors down, presents a large, unknown inductance to the terminating impedance. This essentially makes the line unmatched regardless of the terminating impedances at its ends. The results obtained at this test location are thus reported for the non-terminated line only.

a) b)

Figure 3-7: Short test line site: (a) transformer to line connection (b) measurement setup and spark-gap mounted on the line

3.3.3 Measurements at Klerefontein, Karoo support base

To provide the required electrical energy for the M*eer*KAT systems, an approximately 110 km 33 kV power line has been designed. This line runs from Carnarvon substation to the Karoo core site. During the design of this line, a short 22 kV grid power line was also constructed to supply power to the Karoo support base at Klerefontein. This short line has 13 spans, each of approximately 110 m in length and it is powered, through a 22 kV transformer, by a diesel generator at one end. This line is suspended on wooden poles and has been designed with the same specifications as those used for the wooden section of the main grid 22/33 kV power line.

Sparking noise measurements were carried out on this test line, which is situated about 70 km from the core site. Figure 3-8 is a sketch of the spark-gap noise measurement site. It also shows the position where the spark-gap was attached on the power line, (SG), and various measurement points. The spark-gap test device was set to 2 mm gap length and mounted on the centre conductor of the line as shown in Figure 3-9.

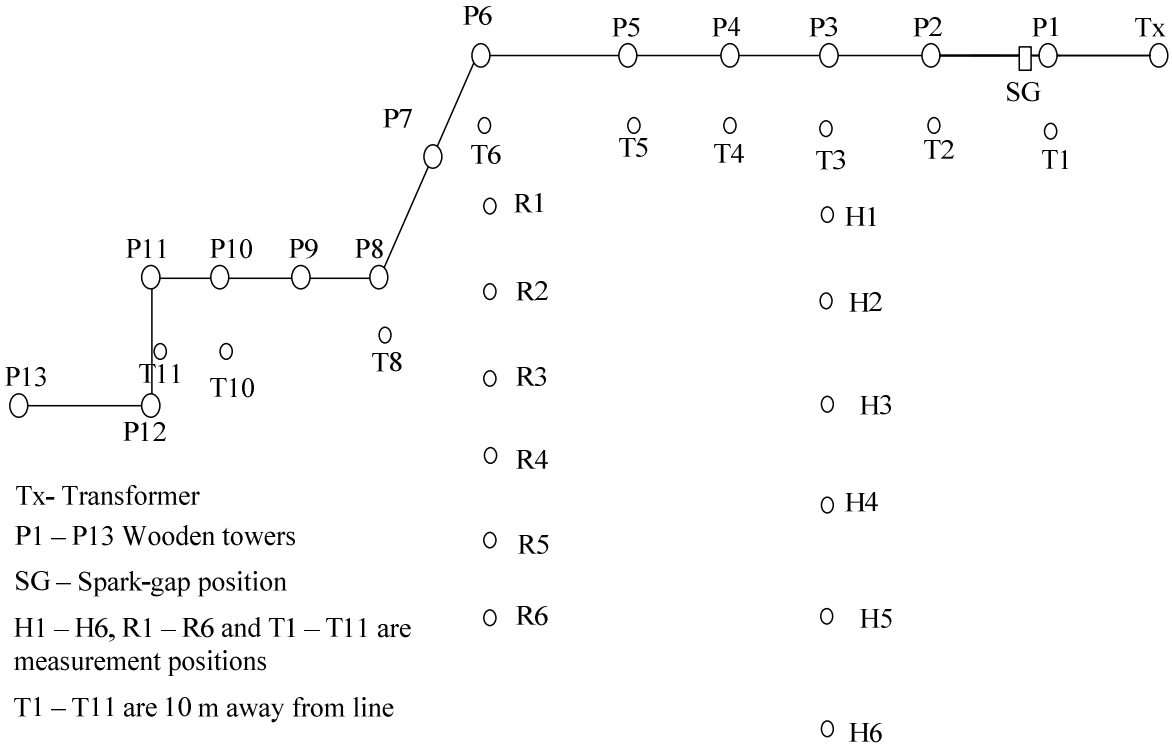

Figure 3-8: Sketch of measurement site at the Klerefontein, Karoo support base

Figure 3-9: Mounted spark-gap device on the centre conductor at point SG

The positions T1 – T11 of Figure 3-8 were used for taking measurements for the longitudinal profile as illustrated in Figure 3-10. This was done to evaluate the amplitude variation of

sparking pulses, injected onto the line, along the line and away from the source location. The frequency spectrum at each position was recorded to observe the change in magnitudes at various frequency points. The positions T6, R1 – R6 and T3, H1 – H6 were used to evaluate the variation of the radiated noise with observation distance. The positions T3 and T6 are 10 m away from the line. The measurement positions from T6 to R4 were 20 m apart. Position R5 was 150 m from the line while R6 was 200 m away. Similarly, the measurement positions from T3 to H3 were 20 m apart. Positions H4, H5 and H6 are 100 m, 200 m, and 300 m away from the line, respectively.

Figure 3-10: Measurements made on the 1.5 km test-line site at point T2 of Figure 3-8.

3.4 Conducted sparking noise measurements

Sparking noise pulses from a source on power line hardware get injected onto the line conductors if that source is coupled to these conductors. Apart from the radiation, these pulses are conducted over a considerable distance from the source along the line conductors resulting in conducted EMI. This conducted EMI can be measured to evaluate its characteristics in comparison to those of radiated EMI measurements.

In the preceding section, the environments and procedures used to undertake radiated noise measurements with the artificial spark generator are described. The radiated pulses were measured in the time domain using an oscilloscope and a SA in zero-span mode. The lines used for these tests were not terminated in their characteristic impedances since power lines in general are unmatched due to the various loads connecting them at any given time. Due to these mismatches, and the fact that the shape of the pulses is dependent on the path length, the measured radiated pulses (as will be seen in section 4.3.2) are oscillatory and this poses difficulties in accurate recording.

To evaluate an approximate pulse shape injected onto the line by this spark-gap device, a conductive coupling measurement was done. This entailed an experimental setup shown in Figure 3-11, which was constructed in the high voltage environment.

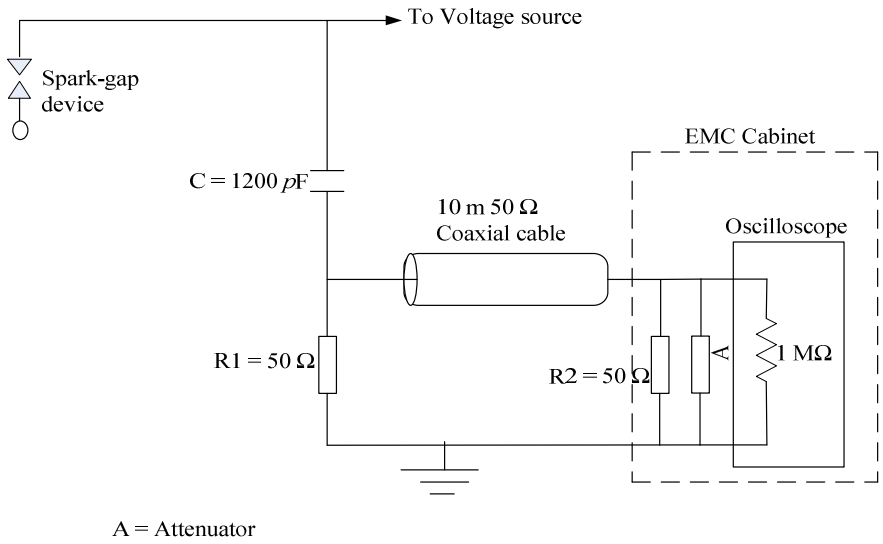

Figure 3-11: Conducted sparking noise measurement circuit at the HV-Lab

Using the same line conductor as for the radiated measurements, the spark-gap device was connected to one end of the line, which is conductively coupled to the high voltage source. An oscilloscope was connected to the line through a matching circuit and a 1200 pF coupling capacitor. The matching circuit used a 50 Ω shunt resistor R1 connected to a 10 m coaxial

cable with characteristic impedance of 50 Ω. The time domain pulses were measured by observing the voltage drop across this shunt resistor R1. The other end of the cable (at the input of the oscilloscope) was connected to another 50 Ω shunt resistor R2. This arrangement avoids multiple reflections due to mismatches.

Since the line was 7 m above the ground, a conducting wire was needed to connect this line to the coupling capacitor as shown in Figure 3-12. The oscilloscope was housed in an EMC cabinet to reduce the background noise level. The conductive pulse amplitudes were expected to be high and this necessitated the use of an attenuator between the shunt resistor R2 and the 1 MΩ oscilloscope input. This ensured that the pulse amplitudes at the oscilloscope input were at an acceptable level. A coaxial variable attenuator HP8495B, operating in the frequency range dc – 18 GHz, with 0 to 70 dB attenuation in steps of 10 dB, was used for this purpose. The observations showed that 20 dB of attenuation was sufficient to carry out safe measurements. The time domain measured characteristics are presented in section 4.3.2.

Figure 3-12: Conducted sparking noise measurement setup at the HV-Lab

3.5 Conclusions

The measurement instrumentation and their setups to be used in this research to investigate the characteristics of power line sparking noise have been described. These systems are used for conducting measurements in the time and frequency domains. The noise characteristics are evaluated in three measurement environments: a 40 m test-line and an approximately 1.5 km power line, and a high-voltage laboratory. An artificially made spark-gap device mounted on one of the energized line conductors was used as a noise generator. Test procedures used for taking the radiated pulse time domain and frequency spectrum as well as conducted time domain properties have been outlined. These properties are discussed in the following chapter.

Chapter 4

Sparking noise measurement results

4.1 Introduction

The experimental setups described in the previous chapter were used to take power line sparking noise measurements. In this chapter, some of the findings from these tests for both radiated and conducted noise are presented. Both the time domain and the frequency domain characteristics of the radiated noise were measured but only the time domain data were taken for the conducted noise. The temporal results were used to extract the information regarding the pulse duration and repetition rates. The spectral results were used to determine the frequency range of the radiated noise and to analyse the noise attenuation with respect to the power line measurement positions in the lateral, height and longitudinal profiles.

4.2 Measured frequency domain characteristics

Before evaluating the radiated frequency spectrum characteristics of spark-gap noise at a given site, it is necessary to survey the background signals in that environment. It is also important to establish the measurement sensitivity and dynamic range.

In the measurement results of this chapter, unless otherwise stated, the receiver's pre-amplifier was always on. In some instances, depending on its availability and necessity, a coaxial low-noise amplifier (LNA) was used to improve the analyzer's sensitivity. The LNA that was used is a commercially available Mini-Circuits ZX60-33LN-S+ that operates over the 50-3000MHz range with a gain of between 13 – 22 dB, and a typical noise figure (NF) of 1.1 dB. To reduce the transmission losses of additional cables and thus maximise the signal-to-noise ratio of the

measuring system, the LNA was connected directly at the SMA input connector of the antenna. The LNA was powered by a regulated 5 V DC from dry cell batteries.

With non-energized power lines, the background noise for each of the measurement sites was always checked. This ensured that signals, such as broadcast signals, were not strong enough to saturate or overload the receiving instruments.

4.2.1 Sparking-noise frequency spectrum

The radiated frequency spectrum of the generated noise was recorded to determine the frequency range of the noise, which could be detected with the available instruments. The effect on the spectrum due to various parameters was also investigated. These parameters included the gap length, supply voltage level, and the change in the SA's RBW.

Typical measured spectra of a spark-gap are shown in Figure 4-1 and Figure 4-2 for the low and high frequency ranges respectively. These spectra were taken on the short test line site, at a measuring position shown in Figure 3-7, with the spark-gap set to 2 mm gap length. The line to ground supply voltage level was set to 12 kV, which was just enough to generate an intermittent sparking for this gap size. With this erratic sparking condition, the maximum peak of the signal was recorded after several sweeps to allow all the frequency components to be captured and to produce a stable spectrum. A spectrum such as that given in Figure 4-3 would be recorded if only a few sweeps are taken. The number of sweeps required depends on the sparking intermittency, sweep time and RBW set. The SA's automatic sweep time setting which varies with the RBW was mainly used. The resultant field strength level is seen to be well above the system's noise floor level and extends beyond 3.6 GHz. This was repeatedly observed in the various measurements performed. This has not been previously reported in the literature and more sensitive systems will show noise components at higher frequencies still. The spectrum is also relatively flat across the considered band.

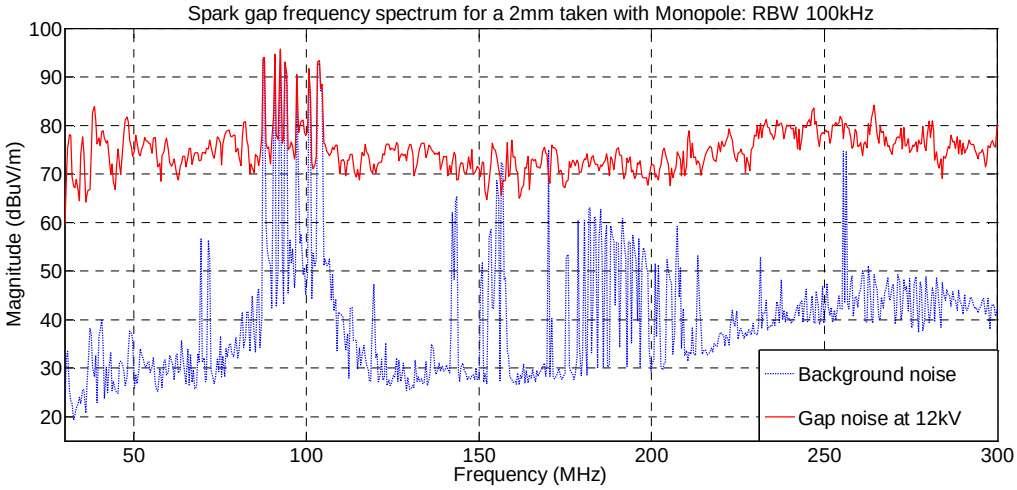

Figure 4-1: Spark-gap lower band frequency spectrum taken on the short test line site

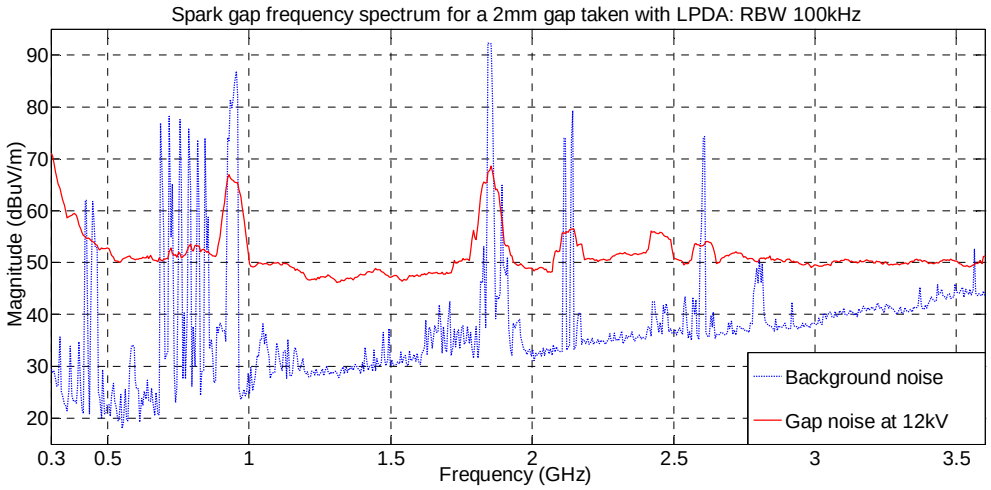

Figure 4-2: Spark-gap higher band frequency spectrum taken on the short test line site

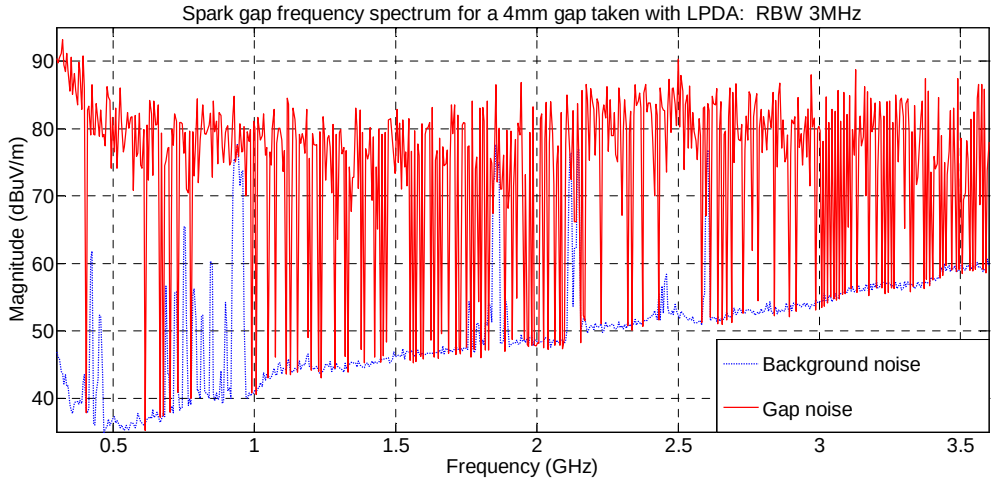

Figure 4-3: An incompletely filled up spark-gap frequency spectrum taken on the short test line site

4.2.1.1 Variation of frequency spectrum with resolution bandwidth

The influence of RBW variation on the frequency spectrum was also investigated. The SA used allows for a wide range of RBW settings, from 1 Hz up to a maximum of 3 MHz, to be made. Variation of the RBW influences the sweep time which is also dependent on the frequency span required and the number of scan points to be taken [39]. The RBW and the sweep time are related by the following equation [39].

$$\Delta T_{sw} = k \frac{\Delta f_{Span}}{RBW^2} \qquad 4\text{-}1$$

where ΔT_{sw} = minimum sweep time, in s

RBW = Resolution bandwidth, in Hz

Δf_{Span} = frequency span for a sweep, in Hz

k = a constant of proportionality

This equation implies that the sweep time is directly proportional to the frequency span and also that a higher RBW requires a smaller minimum sweep time for proper amplitude detection. The maximum sensitivity of a SA is achieved with the lowest IF filter bandwidth setting and thus reducing the RBW improves the resolution and chances of picking up

narrowband signals, at the expense of longer observation time. By varying the RBW and noting the variation of the signal amplitudes, the measured signals can be distinguished as being of either the narrowband or broadband type. The variation of RBW will have no impact on the amplitude of signal the bandwidth of which is equal to or less than the measurement bandwidth. On the other hand, the amplitudes of impulsive and broadband signals whose spectral components are wider than the measurement bandwidth will vary with a change in RBW [41].

Typical frequency spectra taken on the short test line site with various RBW are shown in Figure 4-4, Figure 4-5, and Figure 4-6 for 10 kHz, 100 kHz and 3 MHz bandwidths respectively. Those of 300 kHz and 1 MHz are given in Figure A-1 and Figure A-2, respectively in Appendix A. The spark-gap size for all cases was maintained at 2 mm and the line to ground supply voltage set at about 12 kV. The default sweep time chosen by the analyzer when varying the RBW was used in all reported cases. This ensures that the response time of the analyzer's intermediate filter is not compromised. It should, however, be noted that measurements taken with several sweep time choices gave the same result. The maximum magnitude level of the measured spectra is found to increase with an increase in the RBW. This implies that their real magnitudes are much higher than those measured with the specified RBWs because some of their spectral components fall outside the analyzer's bandwidth. This increase in amplitudes concurs with equation 3-12, confirming the broadband nature of the measured noise. To prevent obtaining erroneous results, the SA was checked to ensure that it was not overloaded. This was done by adjusting its RF attenuator settings. There was no noticeable difference in the recorded spectra with attenuation variation indicating that there was no overloading. The spectrum levels taken with a RBW of less than 10 kHz were not detectable above the system's noise floor level at the high frequencies.

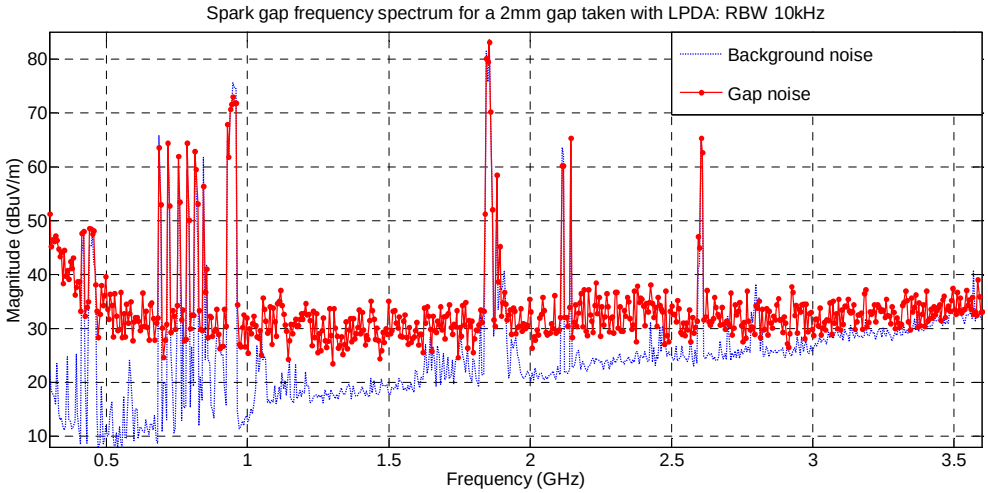

Figure 4-4: Spark-gap frequency spectrum with RBW of 10 kHz

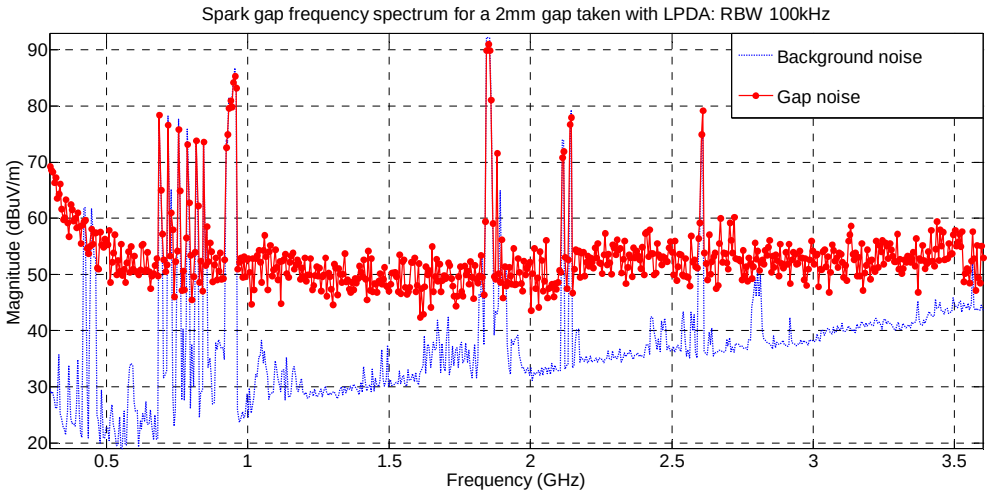

Figure 4-5: Spark-gap frequency spectrum with RBW of 100 kHz

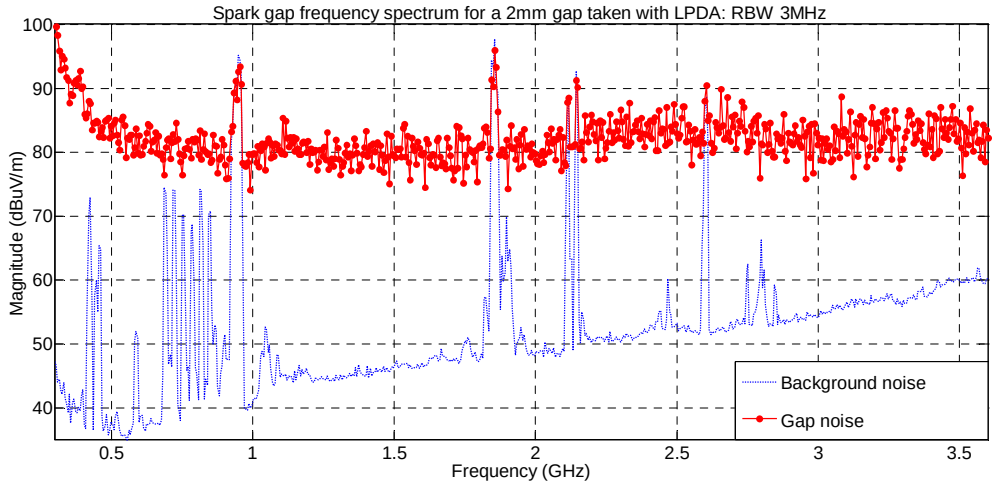

Figure 4-6: Spark-gap frequency spectrum with RBW of 3 MHz

To confirm this trend of increasing noise amplitude with RBW, the frequency spectrum was scanned for portions that are free of background signals. These quiet portions were located at around 600 MHz and 1 GHz. The SA was then set to zero-span mode and centred at each of these two frequencies. The zero-span mode turns the analyzer into a sensitive time domain instrument where the temporal structure of the noise at a specific frequency is provided. The maximum magnitudes of the spark-gap noise from a 2 mm gap length were then measured at various bandwidths. These are shown in Figure 4-7 and Figure 4-8 for 600 MHz and 1 GHz frequencies respectively.

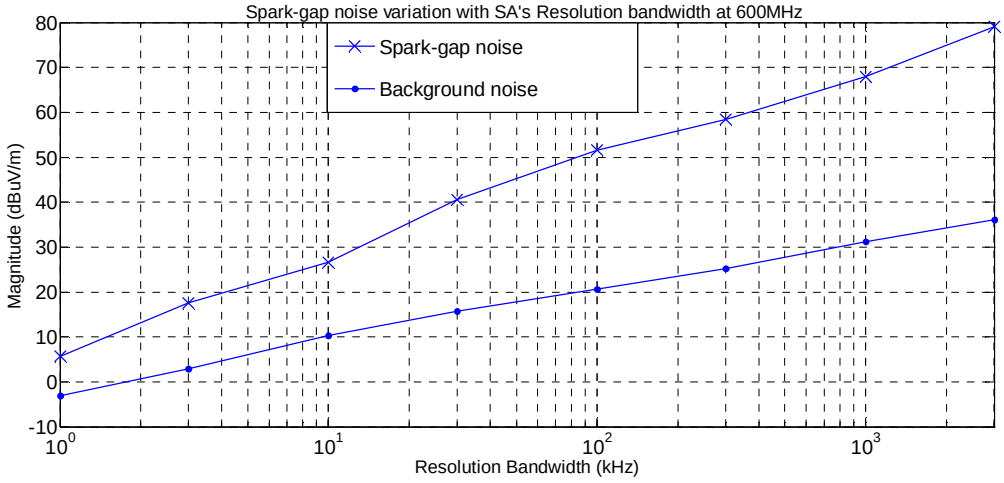

Figure 4-7: Spark-gap noise amplitude variation with RBW taken at 600 MHz

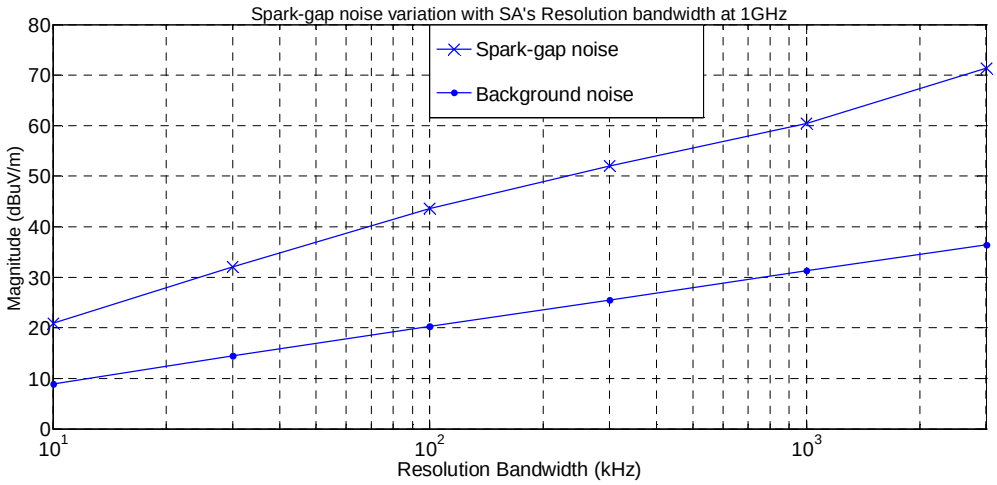

Figure 4-8: Spark-gap noise amplitude variation with RBW taken at 1 GHz

A similar trend was also observed for the 4 mm and 6 mm gap lengths. It can be seen in both plots that the instrument noise floor, as expected for broadband noise, changes by the expected 10 dB per frequency decade of the RBW. The sparking noise, on other hand, varies by around 20 dB, per frequency decade of the RBW, which agrees with what Hodge [15] obtained from the measurements of the impulsive power-line noise in the HF (High Frequency) and VHF (Very High Frequency) bands. This higher change in sparking noise compared to the background noise is due to the latter being stationary over a longer period of time while the former is impulsive in nature characterised by pulses with sharp rising edges. These findings can be used to approximately scale the amplitudes of sparking noise from one measurement bandwidth to another [15]. Due to this dependency on the RBW, the bandwidth at which noise measurements are made has to be indicated.

4.2.1.2 Influence of supply voltage on spark-gap frequency spectrum

The AC voltage applied to the spark-gap device was varied to determine its influence on the radiated frequency spectrum. This was done in both the high voltage laboratory and the short test line sites. With the gap length set to 2 mm, 4 mm, or 6 mm, the applied voltage to each gap was increased until the onset voltage was reached. This was found to be around 11 kV, 17

kV and 23 kV line to ground voltages for the three gap lengths respectively. The sparking condition at these voltages was quite erratic. With further increase in the supply voltage, the resultant radiated frequency spectra were measured. For each gap length considered, the first spectrum recorded was taken with the applied voltage set slightly above the onset voltage. Further measurements were taken as this voltage was increased.

Figure 4-9 is a typical frequency spectrum taken in the high voltage laboratory for a 4 mm gap length with applied voltage level varied from 21 kV to 30 kV. The plots clearly indicate that the radiated field strength level increases with an increase in the supply voltage level. The shape of the spectrum remains unchanged with the variation in the voltage level; this is an important finding. Similar observations were made on the 6 mm gap. With the 2 mm gap length, the resulting frequency spectra are as shown in Figure 4-10. Here the change in the applied voltage has minimal effect on the frequency spectra.

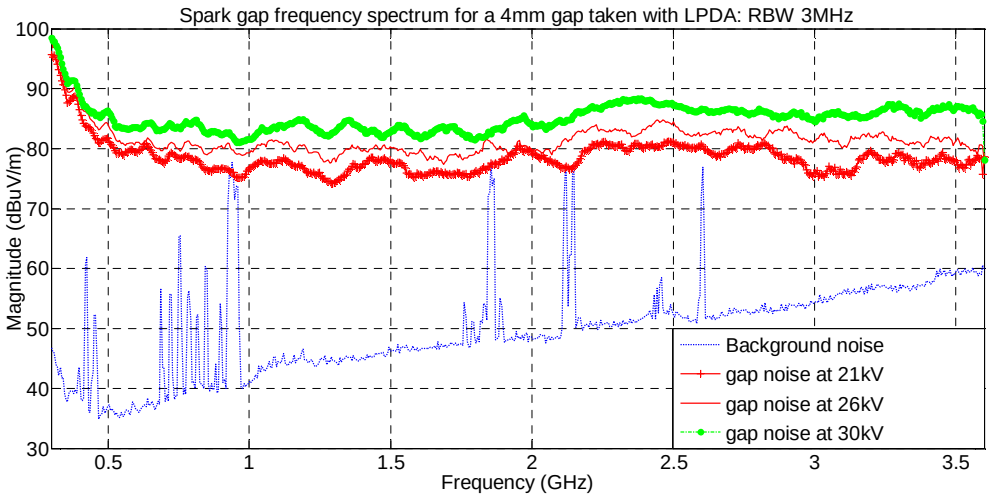

Figure 4-9: Sparking noise frequency spectrum for a 4 mm gap at different supply voltage levels

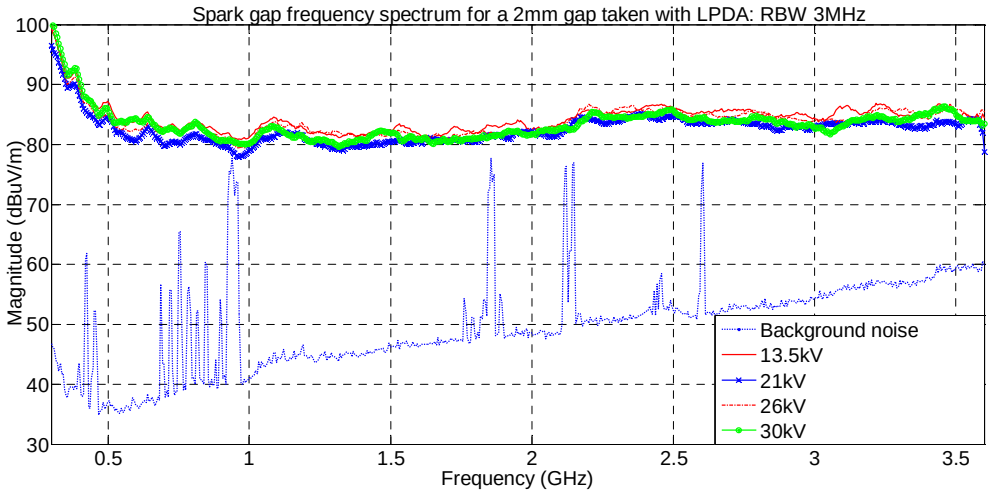

Figure 4-10: Sparking noise frequency spectrum for a 2 mm gap at different supply voltage levels

4.2.1.3 Variation of frequency spectrum with measurement environment

Radiated noise measurements were carried out at both the HV-Lab and on the short test line under similar conditions. This was done to determine the effect contributed by the two sites and the length of the lines on the frequency spectrum. Similar gap length, voltage supply level, and the SA settings were used in both environments. Figure 4-11 gives the frequency spectra for a 4mm gap taken using an LPDA antenna with a RBW of 3 MHz set on the SA. Here, the supply voltage was set to approximately 24.5 kV line-ground voltage level at both sites. The onset breakdown voltage for this gap length was about 17 kV on the short test line and about 18 kV at the HV-Lab.

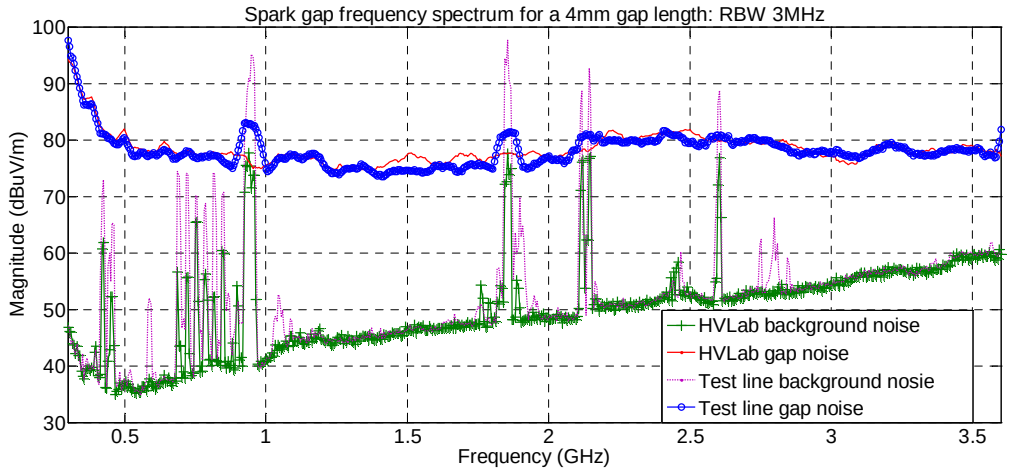

Figure 4-11: Difference between spark-gap noise spectrum as recorded in the HV-Lab and on the short test-line

From this figure, there is no significant difference in the frequency spectra for the sparking noise taken in both environments. This implies that the sparking noise measurements can be carried out in any of these two environments and the results will be representative.

4.2.1.4 Variation of frequency spectrum with gap length

The change in sparking noise frequency spectrum when the gap spacing is varied was evaluated. This was done by varying the gap length of the spark-gap device from 2 mm to 6 mm in steps of 2 mm. With an equal voltage level applied to all the gap lengths, the resulting frequency spectra were measured in the same measurement environment. Similar settings on the measuring instruments were used to make the comparison of the patterns easier.

Figure 4-12 and Figure 4-13 show typical frequency spectra for the three gap lengths as they were taken on the short test line at the same line to ground supply voltage level of 24.5 kV. The 2 mm gap is seen to have a slightly higher energy level across the frequency band as compared to both 4 mm and 6 mm gap lengths. This is because the gap impedance increases with the increased electrode spacing and a higher voltage is required to overcome the air breakdown field strength.

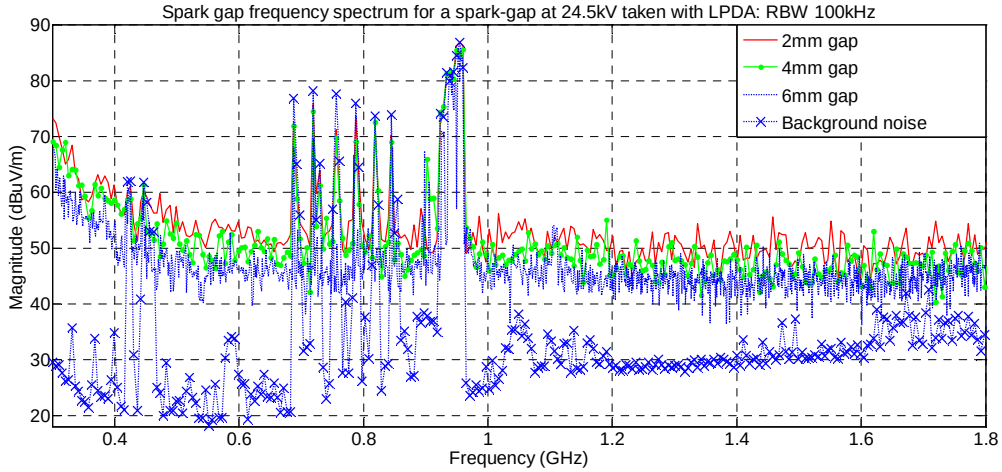

Figure 4-12: Sparking noise frequency spectrum associated with different gap lengths: RBW = 100 kHz

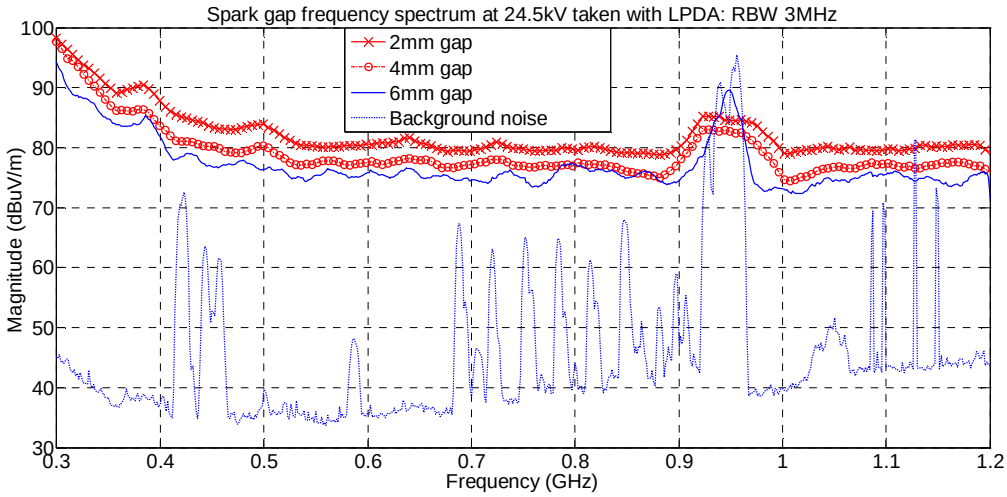

Figure 4-13: Sparking noise frequency spectrum associated with different gap lengths: RBW = 3 MHz

The 24.5 kV supply voltage, which is close to the 23 kV onset voltage of a 6 mm gap, results in a higher pulse repetition rate for a 2 mm gap when compared to the larger lengths. This would imply that short gaps, which can easily occur in bad contacts on power line hardware causes higher interference levels when compared to larger gaps such as those due to inadequately spaced metallic parts which are mostly wider, at the same line voltage level. A

similar frequency spectrum pattern in the measured bandwidth remains unchanged when the gap length is changed.

4.2.2 Sparking noise longitudinal profile

The sparking noise longitudinal profile gives the noise attenuation with distance as measured along the axis of the power line under test. As shown at the Klerefontein site, given in Figure 3-8, this was undertaken by taking field level measurements at points that are nearly parallel to the lines, in this case points T1 – T11. These measurement points were 10 m away from the outer line conductor. The measurements made at each of these points utilized both the dipole and LPDA antennas oriented in both vertical and horizontal polarizations. The FSH8 SA had its preamplifier on and set to Max Peak Hold detection mode. The dipole and the LPDA were used for lower and higher frequency measurements respectively. An external LNA was used between LPDA and the SA to enhance the sensitivity of the analyzer at higher frequencies. The gain of the LNA and the antenna factor of the LPDA antenna are both frequency dependent. Their values, in dB, were later subtracted from the measured signal during post-processing in order to obtain the real field strength levels of the noise. The SA has a feature that allows for transducer characteristics such as amplifier gains and antenna factors to be automatically accounted for by entering their values on transducer tables. The data that is then displayed on the analyzer is the exact field strength levels required. Although this feature is useful, it was not used while carrying out the reported measurements.

Typical measured results are given in Figure 4-14 below where the spectral patterns at each longitudinal position are compared. These measurements were taken with a RBW of 100 kHz. It can be seen that the field strength levels are slightly higher at points near the spark-gap source and start to decay gradually as one moves away from the source. This is also illustrated in Figure 4-15 where the field levels are given for spot frequencies of 500 MHz and 600 MHz. In addition, the spectrum gently decreases with increase in frequency and it is seen that the

higher frequencies are attenuated more than the lower frequencies. The measurements at position T11 were found to be on the noise floor at the applied RBW.

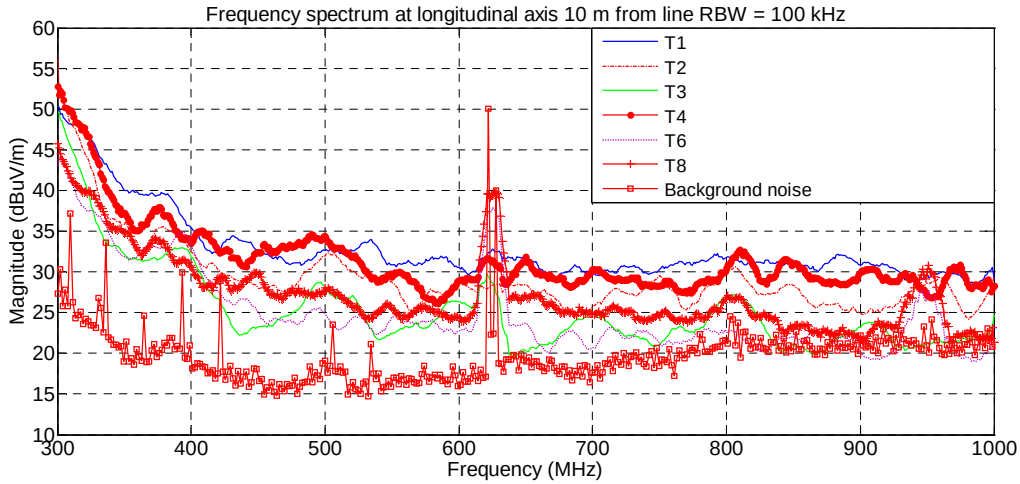

Figure 4-14: Frequency spectrum taken on the longitudinal positions relative to the power line using LPDA antenna

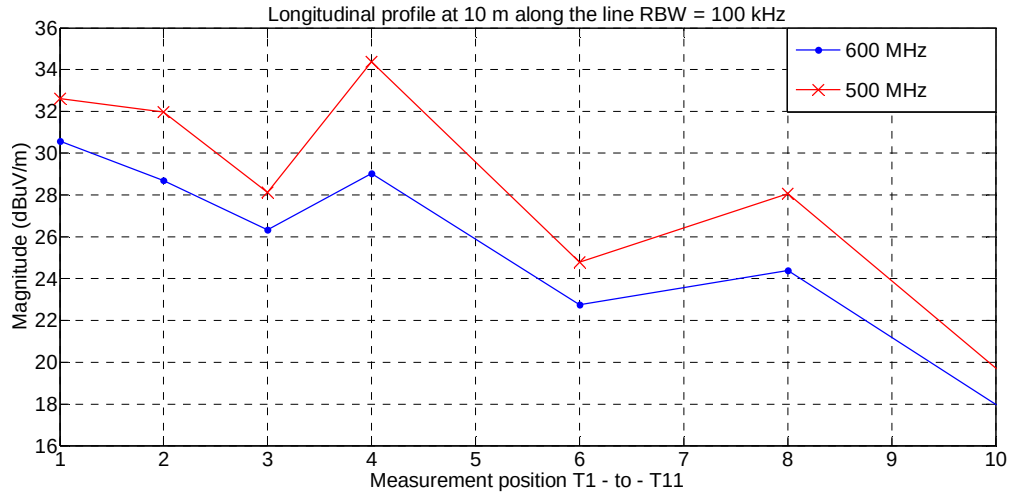

Figure 4-15: Longitudinal profile at two spot frequencies as take at the Klerefontein site

As shown in Figure 4-16 and Figure 4-17, the spectral levels remained almost constant along the line length in the low frequency range. These measurements were taken using a horizontally oriented broadband dipole antenna.

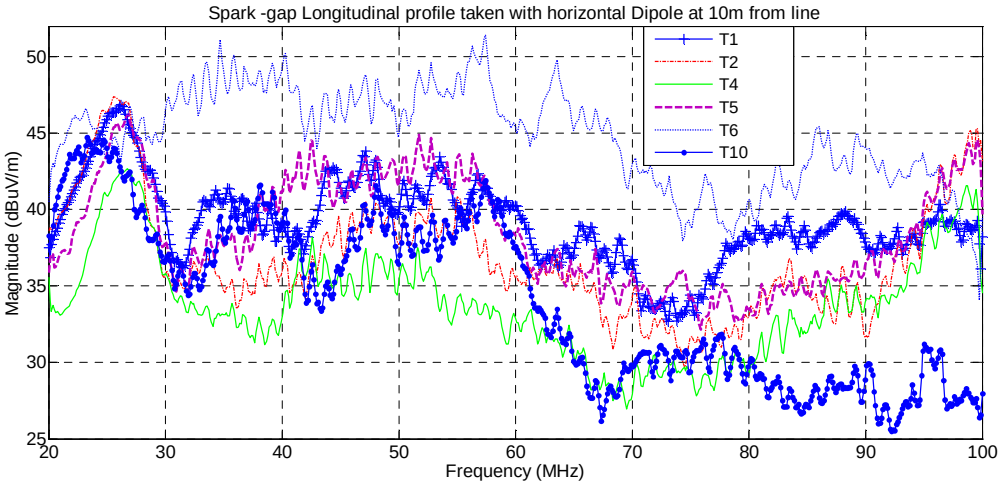

Figure 4-16: Frequency spectrum taken on the longitudinal positions relative to the power line using a dipole antenna

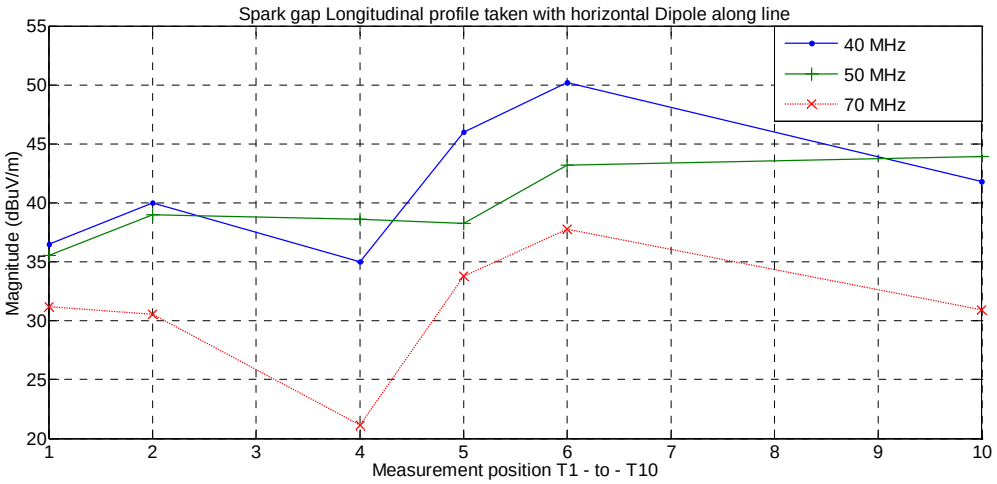

Figure 4-17: Longitudinal profile at two spot frequencies as taken at the Klerefontein site using a dipole antenna

4.2.3 Sparking noise lateral profile

The lateral profile of power line sparking noise describes how the radiated EMI level varies with increasing lateral distance from the power line under test at specific frequencies. These

levels are determined from the frequency spectra at measurement points as one moves away perpendicularly to the line. Examples of this at the Klerefontein site are at points T6, R1 – R6 and T3, H1 – H6, which are perpendicular to the line at T6 and T3, respectively, given in Figure 3-8. Points T6 and T3 are 10 m away from the line while R6 is 200 m away and H6 is 300 m away from the line. The measurements at each of these points used both the dipole and LPDA antennas in both polarizations. The maximum peak of the field strength was measured on the FSH8 SA (SA) with the external LNA to improve its sensitivity at the higher frequencies. As before, the amplifier gain and the antenna factors were later removed from the measured signal during post-processing.

Typical results are given in Figure 4-18 where the spectra were measured at lateral distances T3, H1 – H6. It is evident that the field strength level is greatest at 10 m from the line and it rapidly decreases with an increasing lateral distance. Beyond 50 m from the line, the field levels of these high frequency components do not appreciably change with distance any more. This is demonstrated in Figure 4-19 where the field levels are provided for single frequencies of 400 MHz, 520 MHz and 800 MHz. Due to their short wavelength compared to the distance to the measurement points, the radiated higher frequency components are significantly attenuated as they propagate away from the radiating line. The lower frequency components have a gentle decay with distance as can be seen in Figure 4-20 and Figure 4-21 where a narrow frequency span was taken at all the measurement points.

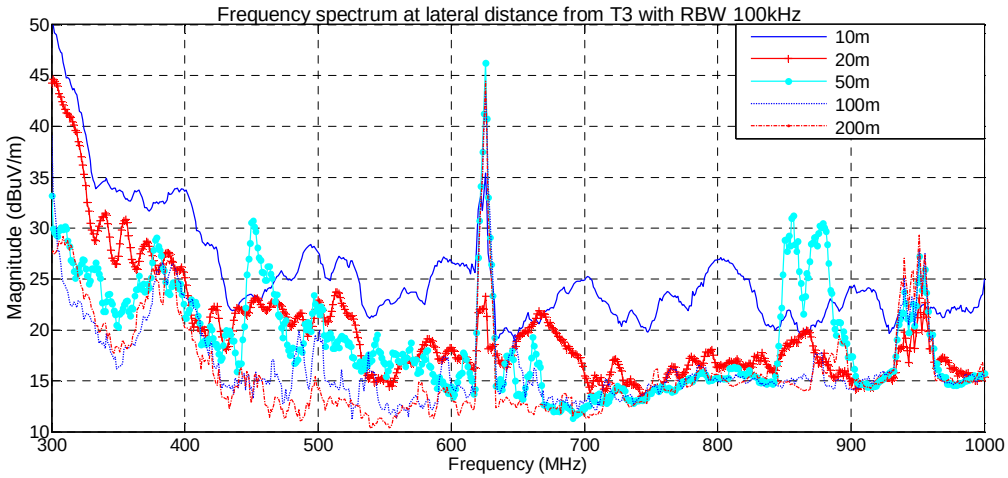

Figure 4-18: Spark-gap frequency spectrum taken at given distances away from the line

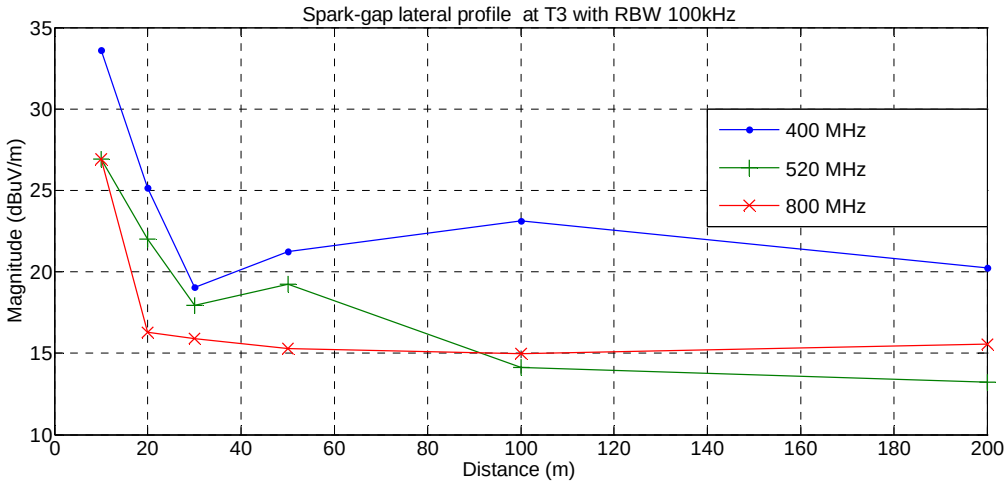

Figure 4-19: Sparking noise lateral profile at specific frequencies

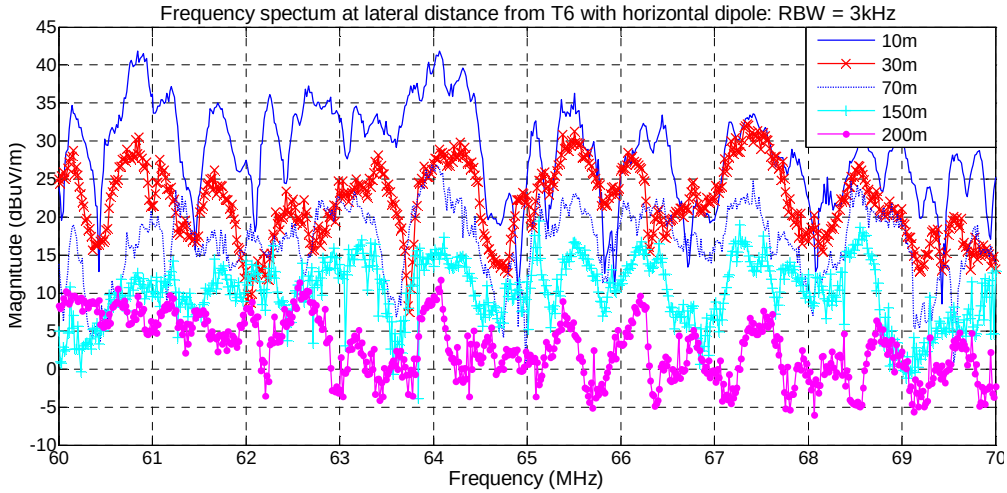

Figure 4-20: Spark-gap frequency spectrum taken at given distances away from the line with horizontal dipole

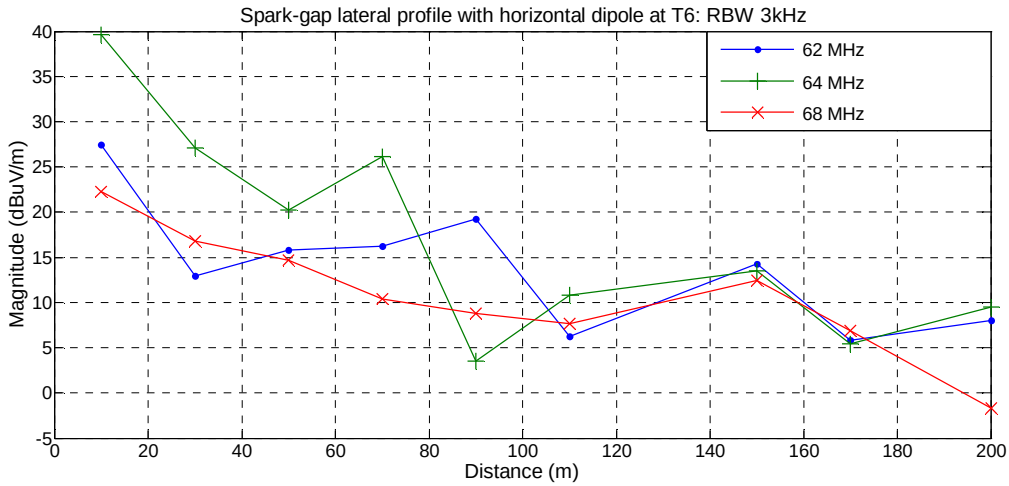

Figure 4-21: Sparking noise lateral profile at specific frequencies

4.2.4 Sparking noise height profile

The sparking noise height profile depicts how the radiated field levels from the power line vary with measurement height above the ground at specific frequencies. This is done by recording the variation of the frequency spectra as the measuring antenna is perpendicularly raised from the ground. In this case measurements were taken at point R2 (see Figure 3-8),

which is 50 m away from the line. The measurement height was varied from 1 m to 13 m above the ground with the help of a crane (a cherry-picker).

Typical results taken using an LPDA antenna are given in Figure 4-22 and Figure 4-23. It can be seen that the sparking noise field levels increase as the antenna is elevated above the ground and peaks at a height of about 10 m. Since the line was about 12 m above the ground, this implies that the noise levels are highest at heights approximately equal to that of the line. This field variation is also affected by direct and ground reflected waves arriving at the antenna and by the interference due to the cherry-picker used. These measurements results show that much of the radiated energy is within or above the height of the power lines. Measurements on the ground level using hand held antennas would definitely underestimate the actual radiated emissions from these lines. The actual radiation would have significant implication on receiving antennas that are higher than the power lines such as those of MeerKAT, which will be about 20 m high.

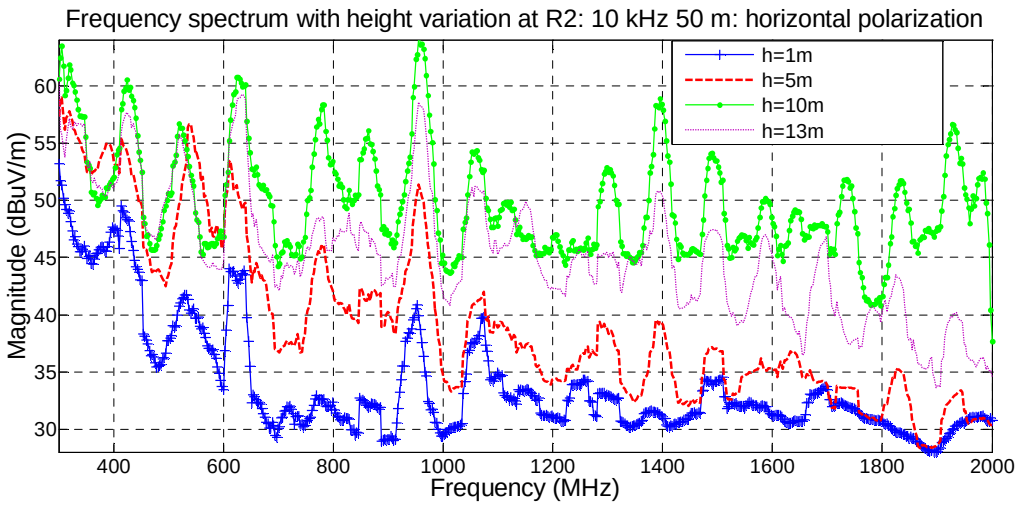

Figure 4-22: Sparking noise frequency spectrum as a function of antenna height

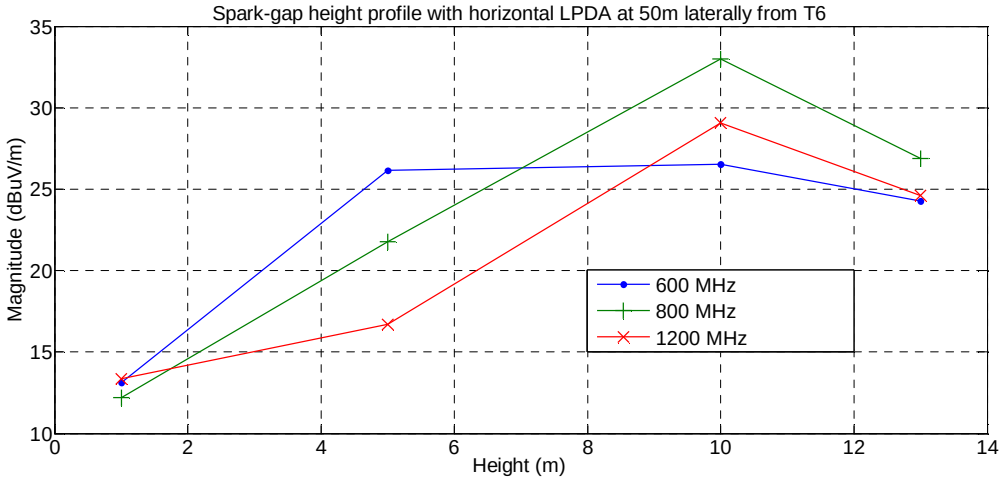

Figure 4-23: Sparking noise field profiles at three frequencies as a function of antenna height

4.3 Time domain characteristics

4.3.1 Radiated temporal results

The radiated sparking noise temporal characteristics were measured using the oscilloscope and with the SA set to single frequency (zero-span mode). As stated earlier, the oscilloscope used has a limited bandwidth of 500 MHz and a sampling rate of up to 2.5 GS/s. The measured results are used to evaluate the radiated single pulse shape, pulse repetition rate and pulse inter-arrival times (the spacing between pulses). It is also important to consider the influence of measurement factors, such as variation of gap length and voltage levels, on these pulse properties.

A typical radiated sparking noise pulse train pattern from a 2 mm gap length measured using the SA is given in Figure 4-24. This was taken at point T2 at the Klerefontein site. The SA was set to zero-span mode at a centre frequency of 50 MHz and the broadband dipole was used. This plot shows a consistent trend of 2 pulses occurring on each of the power-line frequency half-cycles. Due to the magnitude response of the SA's detector, the pulses are displayed here as positive-going pulses. The strong pattern shows no intermittency for the 2mm gap length at the 22 kV line-to-line voltage level. This suggests that any gap, up to 2

mm in size, occurring on such lines due to poor contacts or insufficient spacing between line hardware, would cause a strong radiated sparking phenomenon.

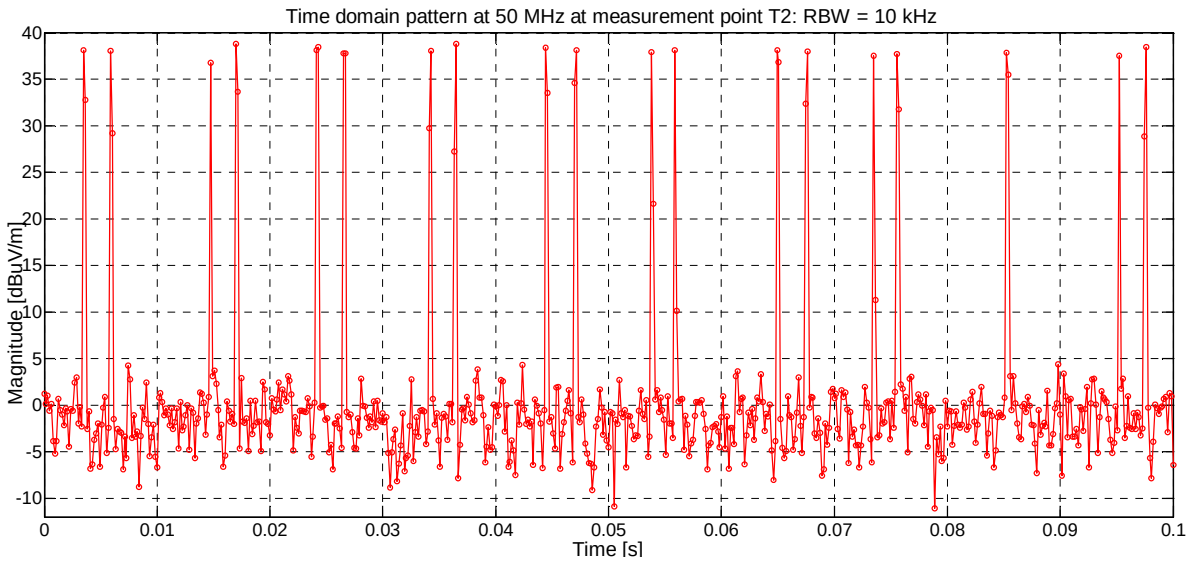

Figure 4-24: Typical radiated time domain pattern taken at the Klerefontein site

The variation of time domain sparking pattern was also measured along the line and the typical observations are as given in Figure 4-25 and Figure 4-26 for the low and high frequencies respectively. The SA was set to 50 MHz and 650 MHz respectively. A consistently strong sparking pulse pattern occurred at the low frequencies along the entire line length. The high frequency pattern on the other hand radiated weak pulses and although the amplitudes of these pulses were randomly varying, generally these amplitudes improved as the measurement position got nearer to the spark-gap source.

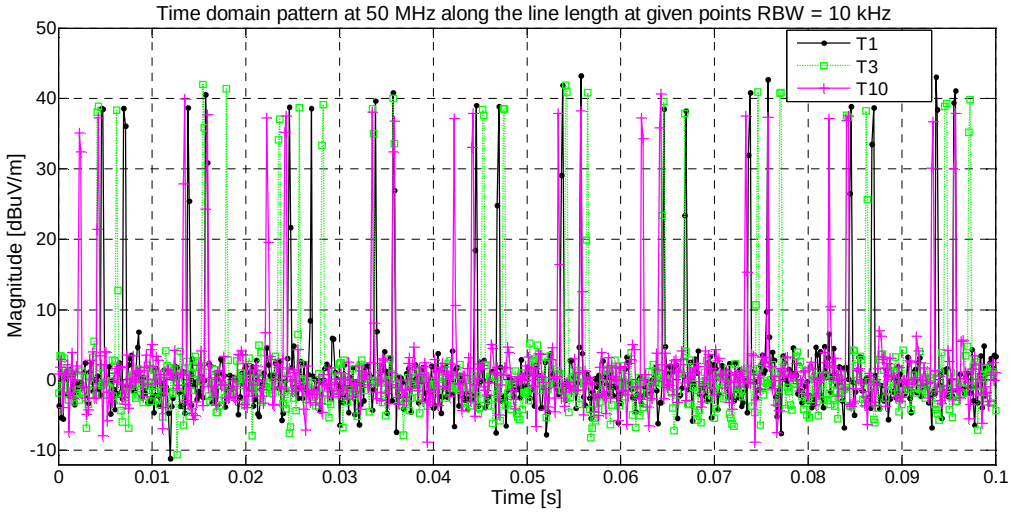

Figure 4-25: Radiated time domain patterns taken along the line length at the Klerefontein site

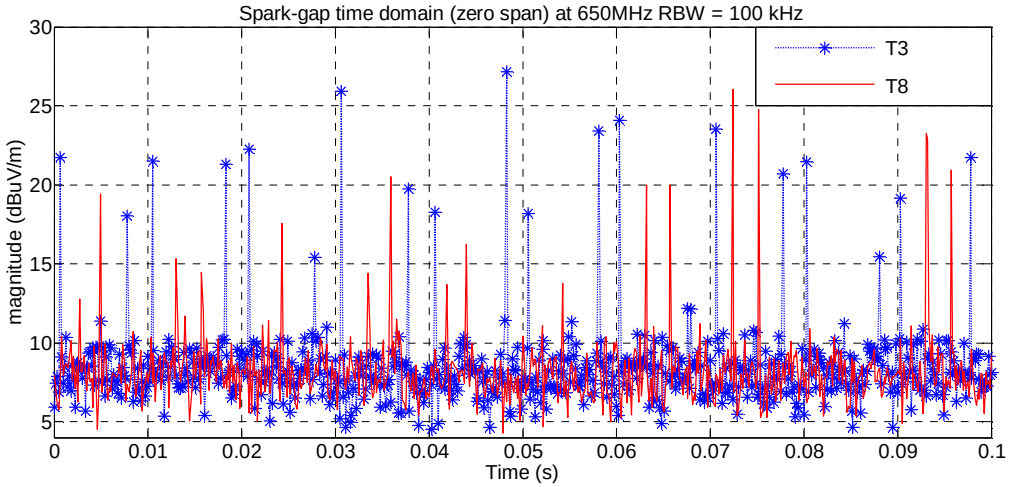

Figure 4-26: Radiated time domain patterns taken at the given points along the line length at the Klerefontein site

The pulse pattern at different frequencies from the same sparking source at similar measuring conditions was also evaluated. Figure 4-27 shows a typical observation taken for a 2 mm gap size under 21 kV line to ground supply voltage in the high voltage laboratory. The pulse trains at the two frequencies of 1 GHz and 600 MHz are seen to retain a similar pattern.

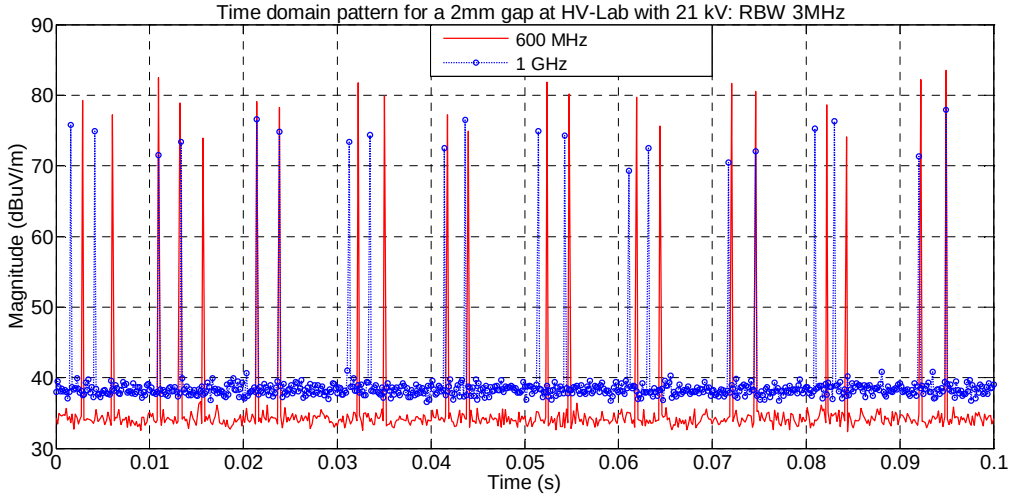

Figure 4-27: Typical radiated time domain patterns at different frequencies taken at the HV-Lab

Figure 4-28 shows the variation of a number of pulses as the line to ground voltage applied to a 2 mm gap length is increased from 13.5 kV to 30 kV. These results were obtained from measurements taken at the HV-Lab using an LPDA antenna and an oscilloscope. Similar results were observed from the measurements taken on the short test line. These figures clearly show that there is a group of sparking pulses, which vary with voltage level, occurring after every 10 ms (power-line frequency half-cycle). The number of pulses in each group increases with the supply voltage level. In parallel, the time spacing between these groups decreases.

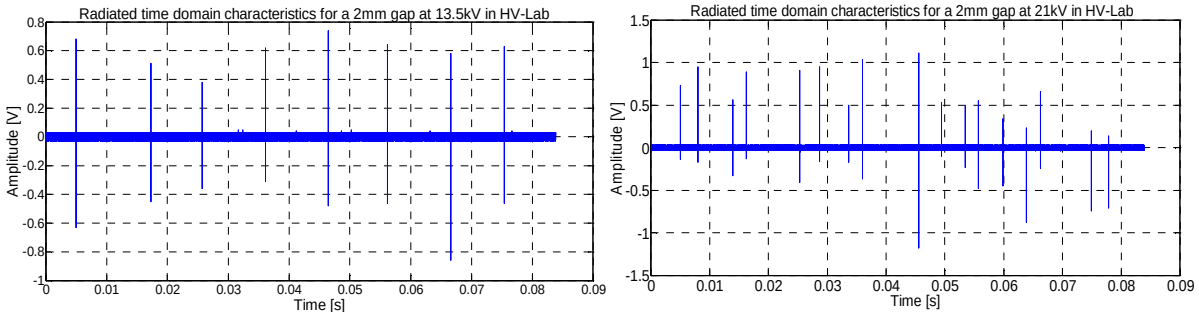

(a) (b)

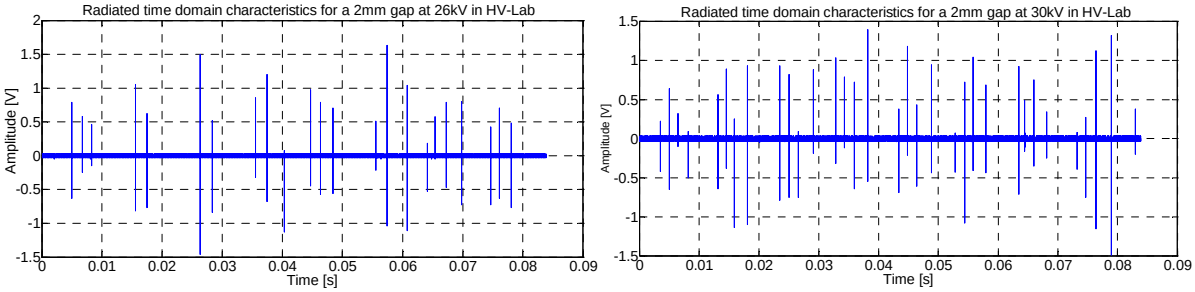

(c) (d)

Figure 4-28: Radiated sparking pulse repetition variation with voltage (a) 13.5 kV b) 21 kV, c) 26 kV and d) 30 kV

This was also confirmed from the zero-span measurements from the SA as shown in Figure 4-29, taken at 600 MHz for a 4 mm gap length. The results for 2 mm and 6mm gap lengths are given in Figure B-1 – Figure B-5 in appendix B.

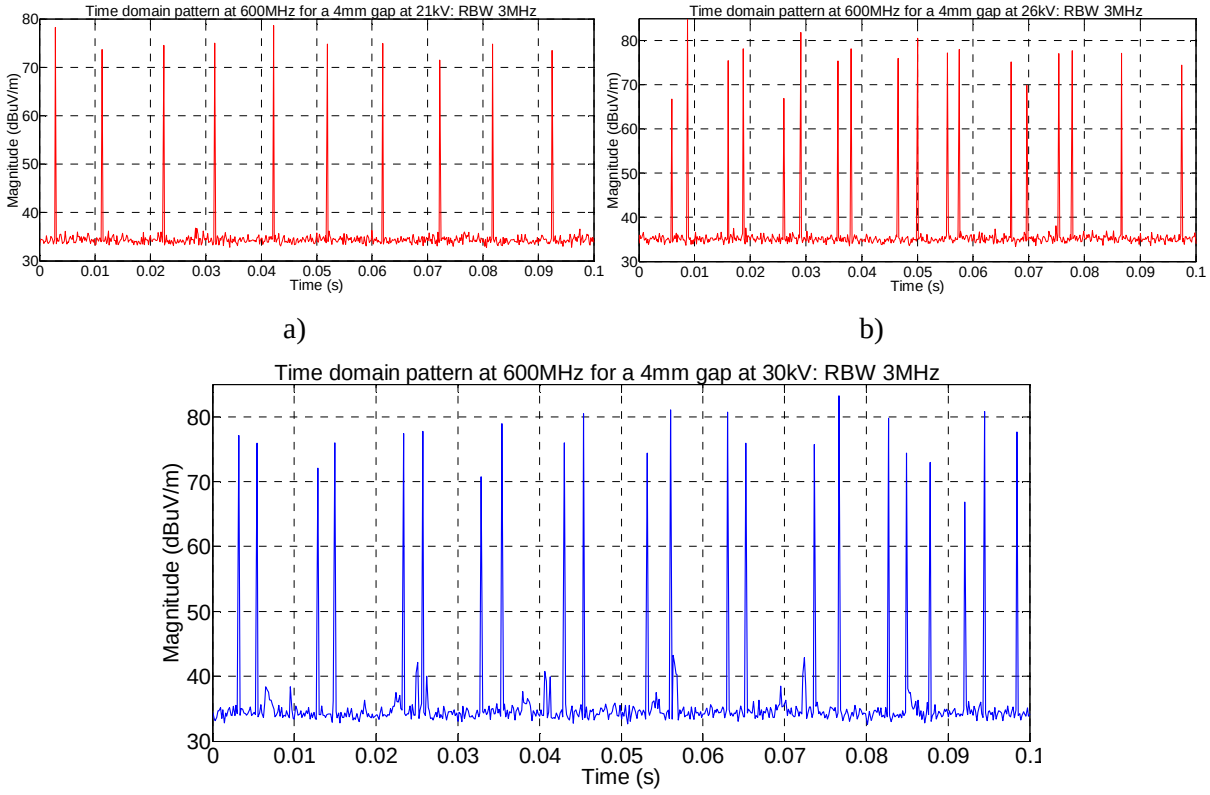

a) b)

c)

Figure 4-29: Radiated sparking pulse repetition variation, for a 4 mm gap, with voltage (a) 21 kV b) 26 kV, and c) 30 kV

As was found from Figure 4-9 that an increase in voltage level resulted in an increase in the magnitudes of the frequency spectrum, Figure 4-28 and Figure 4-29, as expected, indicate that an increase in the pulse repetition rate results in an increase in the interference level.

If the line voltage is known to be at a certain level and the resultant time domain characteristics are observed, a rough estimate of the gap size can be determined. This is because the pulse repetition rate for the smaller gaps is higher as compared to that from larger gaps at the same supply voltage level. This is illustrated by Figure 4-30 where a voltage of 26 kV was applied to 2 mm, 4 mm and 6 mm gap lengths and the time domain pulses measured using a SA. These plots show that the repetition rate is directly dependent on the gap length and the supply voltage.

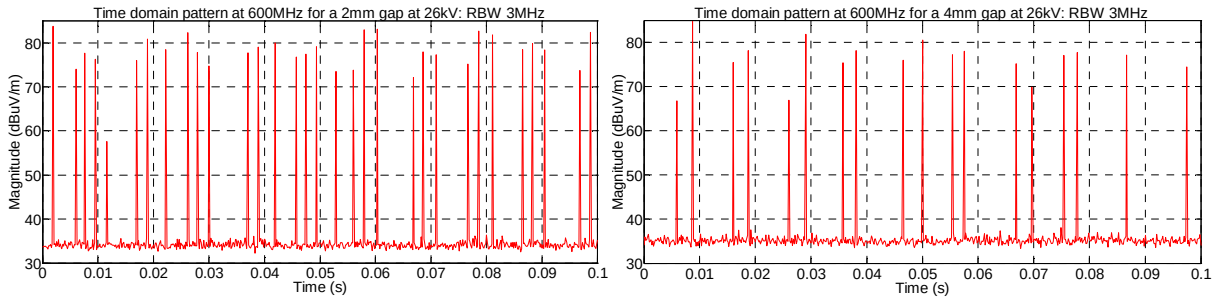

a) b)

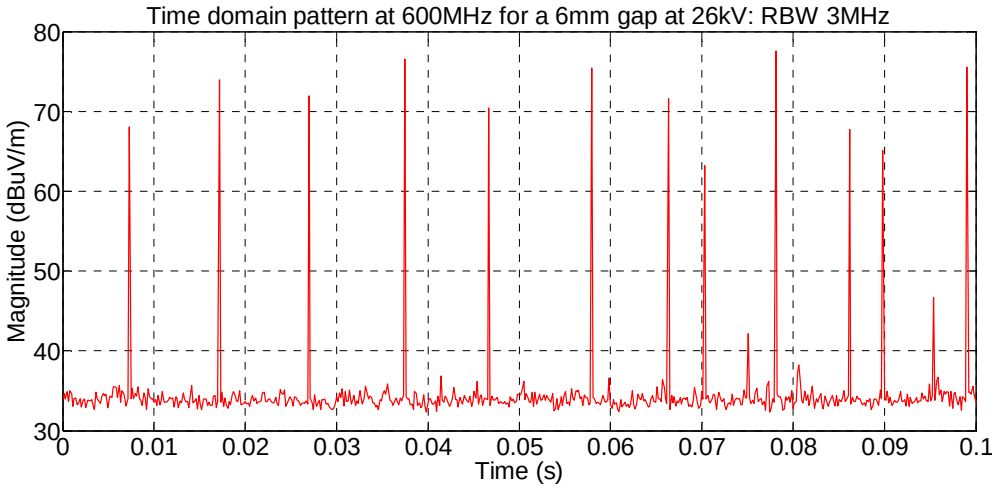

c)

Figure 4-30: Radiated sparking pulse repetition variation, at 600 MHz, with gap length (a) 2 mm b) 4 mm, and c) 6 mm

4.3.2 Conducted noise temporal properties

The conducted sparking noise time-domain characteristics were measured using the oscilloscope from the setup given in Figure 3-11. As for the radiated noise measurements, the results obtained here were used to evaluate the single pulse shape, pulse repetition rate and pulse inter-arrival times. The gap length and the supply voltage level were the measurement variables used to determine their influence on the pulse properties. Several measurements were recorded while changing each of these variables.

Figure 4-31 shows the typically change in the pulse repetition rate as the line to ground supply voltage applied to a 4 mm gap length is increased. This correlates well with the results obtained for the radiated measurements given by Figure 4-29, where the number of pulses per group increases with supply voltage. Each pulse group starts at approximately 10 ms from the previous one, as would be expected from the 50 Hz frequency. One group of pulses is associated with the gap breakdown in the positive power half-cycle, while the consecutive group is associated with the negative half-cycle breakdown.

With the pulse groups that have more than one pulse, the pulse inter-arrival times (the spacing between pulses) was found to vary randomly. This is due to the variable breakdown voltage needed to form each individual sparking event. It was also noted that the number of pulses in each group varies randomly. The pulse amplitudes also increase with an increase in the voltage level and these amplitudes randomly vary from one group to the other and from one pulse in a group to another in the same group.

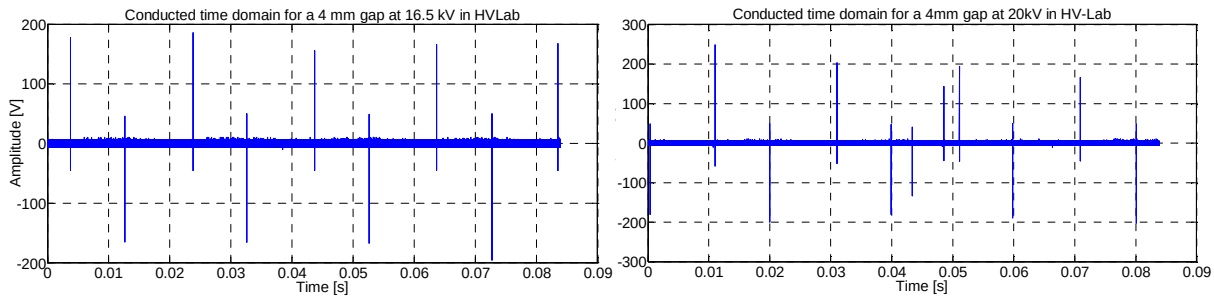

a) b)

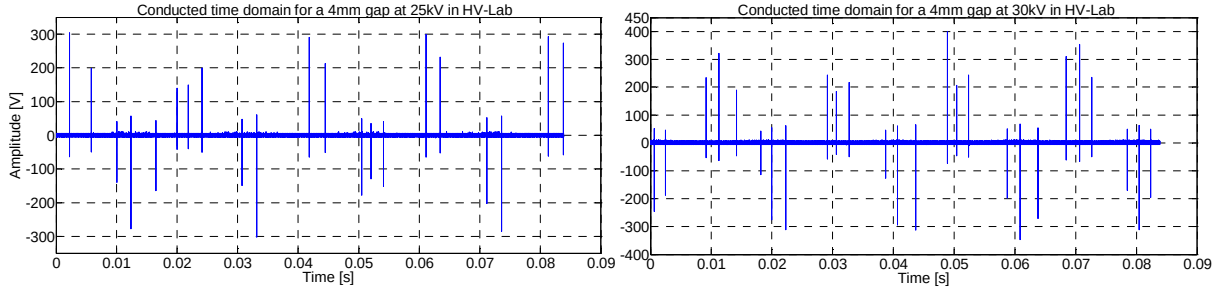

c) d)

Figure 4-31: Conducted pulse repetition variation, for a 4 mm gap, with voltage (a) 16.5 kV, b) 20 kV, c) 25 kV and d) 30 kV

A single pulse was recorded for both radiated and conducted measurements and their observations on the oscilloscope are given in Figure 4-32 and Figure 4-33 respectively. These plots show both positive and negative going pulses. The radiated pulses captured on the measurements taken at the short test-line and on the HV-Lab showed similar shapes. Each of the radiated pulses exhibited a sharp rise time followed by a damped oscillation, which is largely attributed to reflections from various metallic components in the laboratory and the line mismatches.

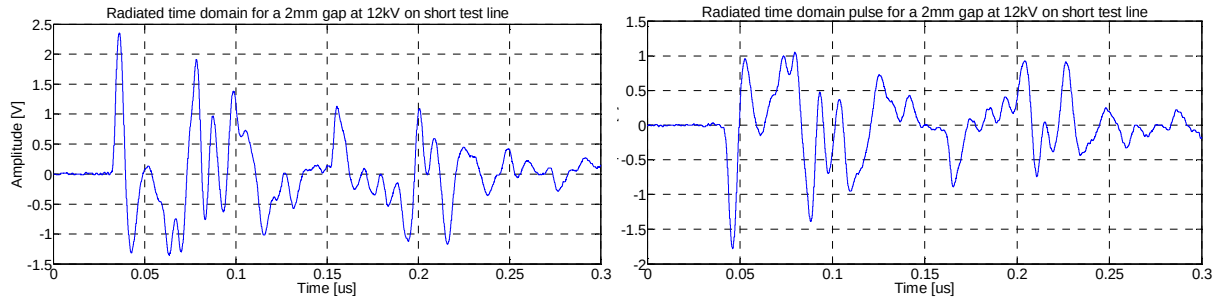

Figure 4-32: Radiated time domain single pulse for a 2mm gap length

Reduced reflections reach the measuring system for the conducted tests. The pulses still exhibit damped oscillations. The pulse rise time can be read from these recorded conducted pulses and it was found to be about 7.8 ns. This is the amount of time the pulse takes to go from low to high voltage and it is computed from 10% to 90% of the full voltage of the pulse.

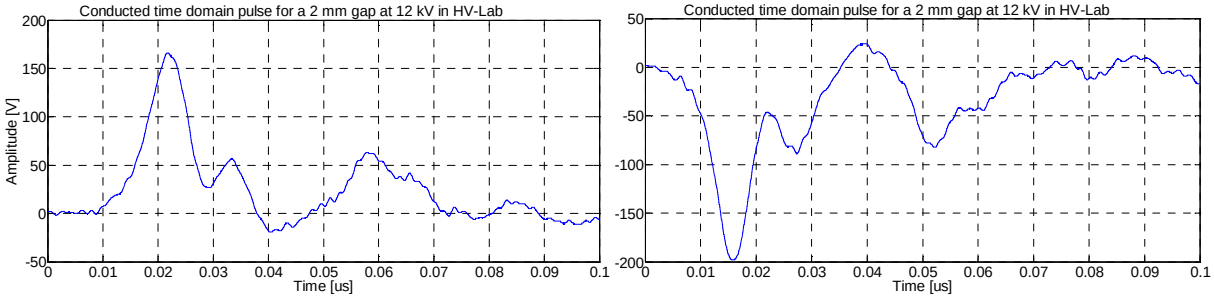

Figure 4-33: Conducted time domain single pulse for a 2mm gap length

4.3.3 Computed time-domain pulse characteristics

The sparking noise frequency spectra given in section 4.2.1 are shown to be wideband. To further investigate the time-domain pulse that gives rise to these spectra, a typical frequency spectrum measured on the short test line, such as that given in Figure 4-6, was converted to the time domain using the inverse Fast Fourier transform (IFFT). It should be noted that there was no significant difference between the measured sparking frequency spectra taken in the HV-Lab and on the short test line for the same gap length and voltage level. The SA only records the magnitude information of the measured EMI, but phase information is also required to obtain the time domain data. The following procedure describes how phase information was recovered. The theoretical voltage pulse, represented by equation 4-2 with voltage amplitude of 1 *V*, was first Fourier transformed to obtain its frequency spectrum data with both the magnitude and the phase information.

$$V(t) = 2.334V_g(e^{-0.51t} - e^{-1.76t}) \qquad 4\text{-}2$$

This expression is similar to the double exponential current pulse given by equation 2-7 and plotted in Figure 2-5. The phase information, which is shown in Figure 4-34, was then used together with the SA-measured magnitude data in the corresponding frequency range. The resultant complex data was converted through an IFFT resulting in a time-domain pulse given in Figure 4-35.

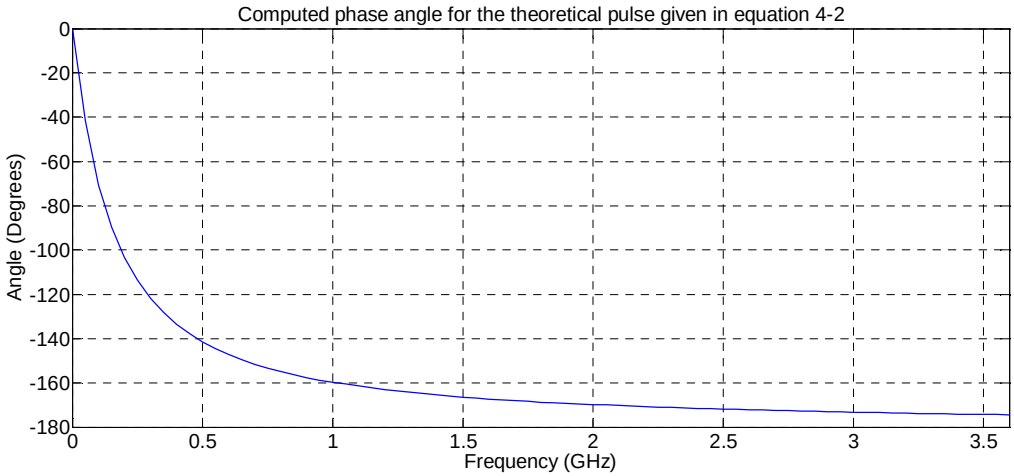

Figure 4-34: The phase angle for the theoretical voltage pulse given in equation 4-2

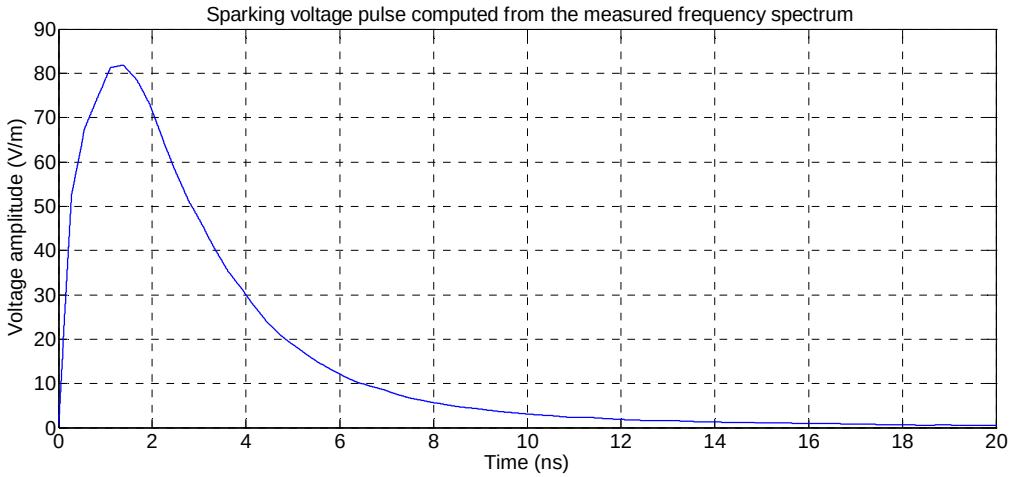

Figure 4-35: Typical sparking pulse computed from the measured frequency spectrum and the phase from the previously reported double-exponential sparking pulse.

It can be seen that the pulse has a double exponential shape, which can be expressed in the form of equation 4-3. To completely express this pulse, the quantities α, β, and K, of equation 4-3, have to be determined. This can be done using the known pulse parameters: the time t_t to 50% on the pulse tail, the time t_m to the pulse crest, and the crest value V_g [19]. From Figure 4-35, $t_m \approx 1.2$ ns, $t_t \approx 3.3$ ns and $V_g \approx 81$ V/m. These can then be used to calculate the unknown quantities through the equations [19]:

$$V(t) = KV_g\left(e^{-\alpha t} - e^{-\beta t}\right), \qquad t \geq 0 \tag{4-3}$$

$$\alpha = \frac{\ln(x)}{t_m(x-1)} \tag{4-4}$$

$$\beta = x\alpha \tag{4-5}$$

and

$$K = \frac{1}{e^{-\alpha t_m} - e^{-\beta t_m}} \tag{4-6}$$

where *x* is solved through a trial and error of the expression

$$\frac{2(x^y - 1)}{x^{\frac{xy}{x-1}}} = \frac{(x-1)}{x^{\frac{x}{x-1}}} \tag{4-7}$$

where $y = \frac{t_t}{t_m}$. From equations 4-4 – 4-6, the resulting pulse waveform can be expressed as

$$V(t) = -0.5630V_g(e^{-1.1379t} - e^{-0.5931t}), \qquad t \geq 0 \tag{4-8}$$

Normalizing equation 4-8 results in an idealized pulse shape given by Figure 4-36, which also presents the normalized pulse of Figure 4-35. The newly-proposed double-exponential pulse was then transformed into the frequency domain. Its phase was then re-applied to the original SA-measured frequency spectrum data. The IFFT'ed time domain was then compared to the double exponential of equation 4-8 and found to make little difference. The phase choice for the measured data thus appears to be consistent and realistic. The double-exponential pulse is thus proposed as an improvement on previously-reported sparking pulse phenomena.

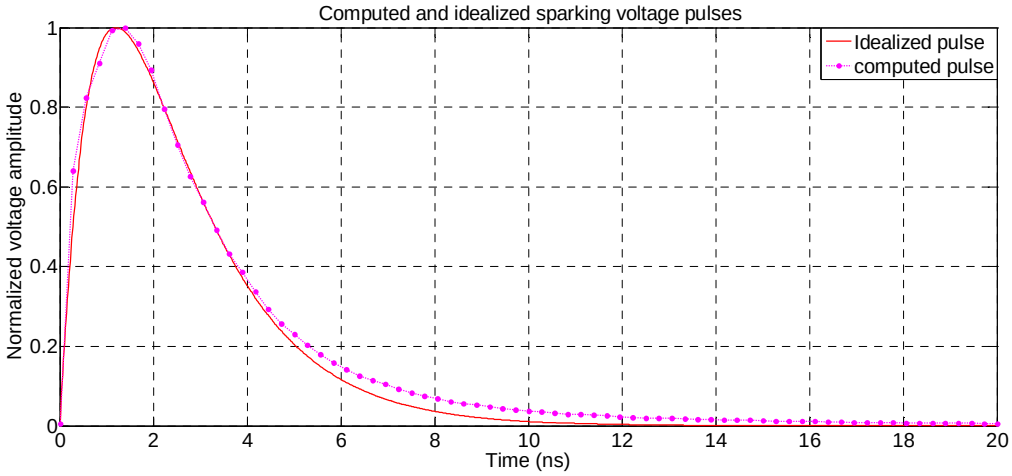

Figure 4-36: Computed and idealized sparking voltage pulses

4.4 Conclusions

A detailed investigation of the measured characteristics of sparking noise has been provided in the present chapter. One of the important findings of this study is the wide radiated frequency spectrum of this noise, which was found, with our measurement instruments, to extend well beyond 3.6 GHz. This spectrum, which was found to be relatively flat across the considered frequency band, was also shown to be dependent on the RBW of the measuring receiver. The effect resulting from the variation in gap length, supply voltage levels, and the measurement environment on the noise frequency spectrum was also investigated. The noise propagation properties, in the form of lateral, longitudinal, and height profiles, were also studied. The measured time domain properties of both radiated and conducted sparking noise pulses have also been reported. A double-exponential pulse computed from the measured radiated sparking frequency spectrum has been proposed, which is an improvement on previously-reported sparking pulse phenomena. Since sparking pulses get injected onto the associated power lines it is necessary to evaluate the antenna radiation characteristics of these lines. This evaluation is carried out in the following chapter.

Chapter 5

Power line simulation and scale modelling

5.1 Introduction

The preceding chapter presented the measured sparking noise characteristics due to a source on active power lines. The presence of such a source on the line causes the line conductors and its associated conducting hardware to act as radiators. An investigation of the radiation pattern characteristics of the power line network needs to be investigated. For the MeerKAT system, the supply lines will be laid out from a substation to the site located in a remote area. It is necessary to consider the possible interaction between the radiated fields from the lines and the receiving antennas located near such lines. This chapter evaluates the radiation characteristics of a line through numerical simulation and measurement of physical scale-modelled lines. The material is extensive and will be presented in these principal sections:

- Analytical and computational analysis of single long-wire geometry to test the ability of the simulation code to characterise the radiation properties of electrically large power-line structures.
- Computational far-field radiation pattern analysis of a multiconductor configuration as a function of the line parameters such as length, topology, ground properties and termination impedance.
- Final analysis of the far-field and near-field radiation characteristics.

5.2 RFI propagation on power lines

The sparking noise sources, as discussed in Chapter 2, are mainly found on the line hardware located at the poles. The pulses from these sources get injected onto the directly attached line conductors. The current may or may not be injected to the other line conductors depending on their association with the EMI source. For example, if the source is an imperfect connection between a tie wire and one line conductor, the resulting sparking pulses will get injected onto, and propagated by, that conductor. These currents may be reactively coupled to the other nearby conductors and their magnitudes are lower than those in the main conductor.

Depending on the location of the source on the line, a current pulse injected onto the conductor divides into two pulses of equal magnitudes and travelling in opposite directions along the conductor [21]. These pulses get attenuated and distorted as a result of radiation and also dispersion of their spectral components as they travel along the conductors. The sparking noise frequency components resulting from these current pulses will get attenuated. Noise attenuation is related to frequency; the higher frequency components will fade out more rapidly than the lower frequencies as distance from the sources increases.

The EMI generated by these time-varying current pulses propagates in one or more of the following modes [44]:

- Direct radiation at the source, where the source hardware and/or the attached line conductor act as an antenna.
- Conduction or guided mode, where the noise pulses are transported along the surface of the line conductor.
- RF inductive coupling, where the noise current pulses in one line conductor get induced on the other nearby phase conductors. The resulting EMI can then be conducted down the line or radiated by these conductors.

- Secondary radiation especially due to the conducted and/or induced RF currents encountering line irregularities such as line bends, insulators, etc. making these points secondary radiators.

All these propagation modes usually occur at the same time from a single sparking source on a line [44]. The EMI associated with the conduction mode decays slowly along the length of the conductors but more rapidly in directions perpendicular to the line conductors, approximately inversely proportional to the square of the distance [45]. On the other hand the EMI from the radiation mode decreases relatively slowly, approximately inversely proportional to the distance, in directions perpendicular to the line conductors. The radiation mode from the lines is of great interest since the detrimental effect caused by the resulting interference could affect the location and/or the operation of the MeerKAT antennas. Since these lines and the associated sparking source hardware act as radiating antennas, it is therefore necessary to evaluate their radiation characteristics due to a source present at an arbitrary location along the line. The aim here is to determine the propagation of radiated EMI as a function of distance from the lines and also their radiation patterns.

By considering the line wires and other conducting hardware as radiators, and due to their long dimensions with respect to the noise wavelength, the problem will have the properties of a long-wire antenna. A long-wire antenna is an antenna made of a long conductor whose length is at least one wavelength at the operating frequency [46]. Generally, power lines are not designed for signal propagation at high frequencies and therefore they are poorly matched due to the presence of grounded conductors, transformer taps on individual phases, junctions, a change in the direction of the line and conductor spacing that often varies from pole to pole. These impedance mismatches may cause direct radiation or radiation by reflections of the currents being propagated along the line, which form standing waves that are radiated from these line conductors. However, since the line is very long (in terms of wavelength), the radiation and ohmic losses in the wires reduce the strength of reflected wave as compared to that at the source. The radiating line thus behaves dominantly as a travelling wave antenna.

The EM radiation characteristics of such a line problem can be analysed using the EM and the antenna theory. The radiating elements can be subdivided into successive sets of small electric dipoles radiating in free space above a lossy ground plane having finite conductivity [47]. The current distribution along each dipole is computed and the resulting radiated EM fields can then be approximated by summing all the contributions.

5.3 Problem analytical approach [46]

To help illustrate the radiating behaviour of such a long line, an analysis of the radiation characteristics of a simple single-line long-wire antenna is considered in this section. In this case, the radiated field patterns in the far-field region are evaluated. The radiation pattern is either a 2- or 3-dimensional plot of the antenna's radiated energy as measured at various angles at a constant radial distance from the antenna [48]. The far-field region is one of the three regions surrounding the radiating wire antenna. The other regions are the reactive near-field and the radiating near field. The far-field region is the region in which $r > 2D^2/\lambda$, where D is the largest linear dimension of the wire antenna, r is the radial distance from the radiating wire antenna, and λ is the wavelength. In this region, the angular field distribution does not vary with the distance from the radiating wire and the field level decays according to the inversely proportional to the distance.

The geometry of such a single wire line is as shown in Figure 5-1. This line has a length l and is placed at a height h, in free space, above an infinite perfect electric conductor (PEC) ground plane. The radiated fields can first be determined by considering the line to be situated in free space. Then the image theory, where an image of the structure is introduced as shown in Figure 5-2, is used to account for the presence of the ground plane. For the purpose of the analysis, the wire is assumed oriented along the y-axis with the z-axis being perpendicular to the interface plane formed by PEC and air. The x-axis is parallel to this interface plane. The line is fed at one end and terminated at the other with its characteristic impedance, which can be obtained using the expression:

$$Z_0 = 60cosh^{-1}\left(\frac{h}{a}\right) \qquad 5\text{-}1$$

where *a* is the radius of the wire.

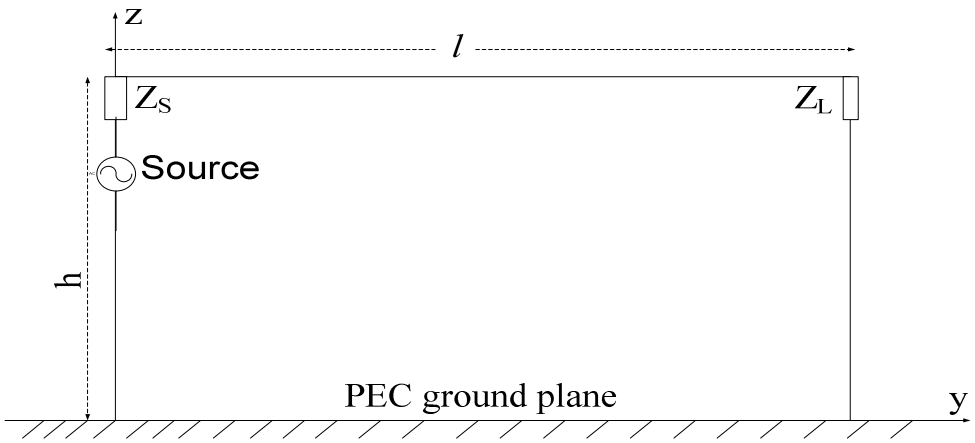

Figure 5-1: Geometry of a long wire line above an infinite PEC ground plane

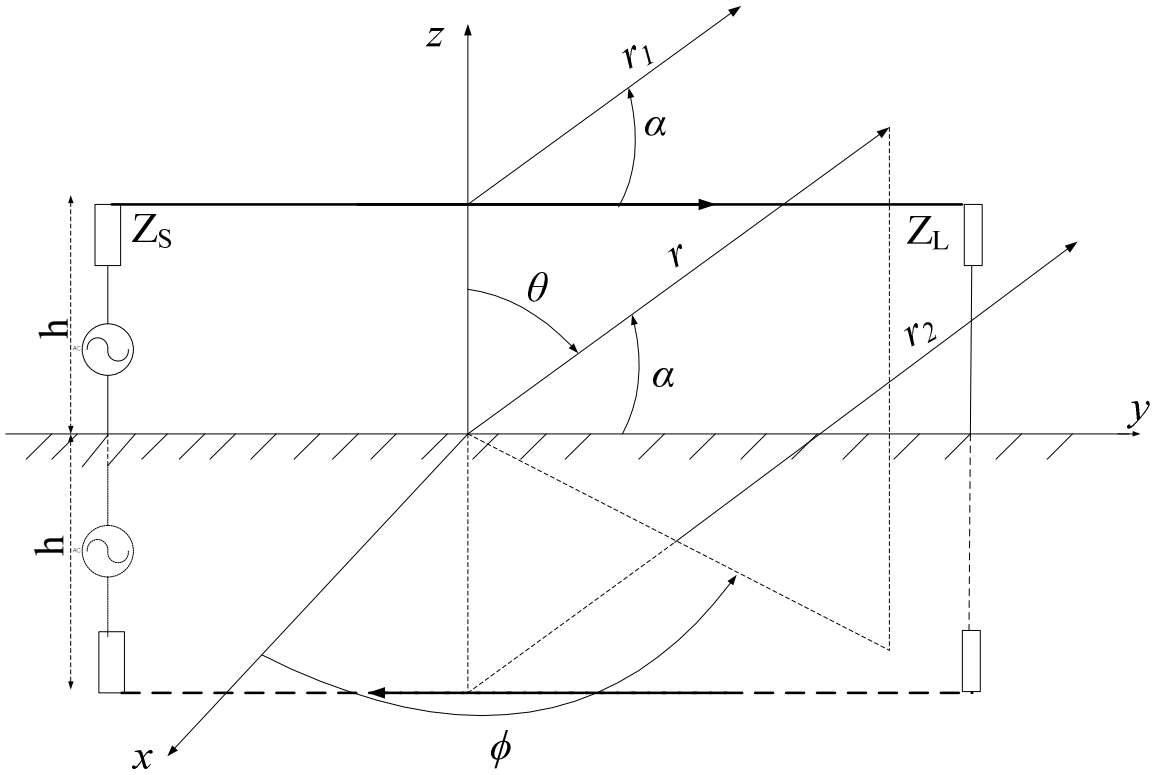

Figure 5-2: Horizontal long wire line, and its associated image, above a PEC ground plane

The angles ϕ and θ and *r*, in Figure 5-2, are the coordinates of the spherical coordinate system. The arbitrary angle α is the angle between the spherical radial direction *r* and the wire- axis. It should be noted that at $\phi = 90^0$, $\alpha = 90^0 - \theta$.

The analysis of the radiation characteristics of this wire starts by considering the current distribution induced along the wire. For an electrically long wire, the current distribution varies along the line length since the travelling wave leaks energy as it travels along the wire. However, this leakage is usually small if the radiating medium is air and can be neglected. An approximation of the current distribution for a y-directed travelling wave can be given as

$$\bar{I} = I(y')e^{-j\beta y'}\hat{a}_y = I_0 e^{-j\beta y'}\hat{a}_y \qquad 5\text{-}2$$

where β is the phase constant associated with the travelling wave, *y'* is the *y* coordinate at the source i.e. the value of *y* along the line, and I_0 is an assumed constant amplitude for the current waveform.

To establish the fields radiated from the wire, the magnetic vector potential, ***A***, due to the approximated current distribution needs first to be determined. For an end-fed wire placed along the y-axis, this magnetic vector potential is given by

$$\bar{A} = \mu \frac{e^{-jkr}}{4\pi r} \int_0^l \bar{I}(y')e^{jky'cos\alpha}\, dy' \qquad 5\text{-}3$$

where *l* is the length of the wire, *k* denotes the free space wave number, and *r* is the radial distance from the source point to an observation point. Substituting equation 6-2 in 6-3 leads to

$$\bar{A} = \mu I_0 l \frac{e^{-jkr}}{4\pi r}\hat{a}_y e^{j\frac{l(kcos\alpha-\beta)}{2}} \frac{sin\left[\frac{l}{2}(kcos\alpha-\beta)\right]}{\frac{l}{2}(kcos\alpha-\beta)} \qquad 5\text{-}4$$

where, based on the definition of the dot product, *cosα* can be written as

$$cos\alpha = \hat{a}_r \cdot \hat{a}_y = sin\theta sin\emptyset \tag{5-5}$$

Inserting equation 5-5 in 5-4 and using the transformation between the rectangular and spherical components, the radiated far fields are then written as

$$E_r = H_r = 0 \tag{5-6}$$

$$E_\theta \approx -j\omega A_\theta = -j\omega\mu I_0 l \frac{e^{-jkr}}{4\pi r} e^{j\frac{l(ksin\theta sin\emptyset-\beta)}{2}} \frac{sin\left[\frac{l}{2}(ksin\theta sin\emptyset-\beta)\right]}{\frac{l}{2}(ksin\theta sin\emptyset-\beta)} cos\theta sin\emptyset \tag{5-7}$$

$$E_\emptyset \approx -j\omega A_\emptyset = -j\omega\mu I_0 l \frac{e^{-jkr}}{4\pi r} e^{j\frac{l(ksin\theta sin\emptyset-\beta)}{2}} \frac{sin\left[\frac{l}{2}(ksin\theta sin\emptyset-\beta)\right]}{\frac{l}{2}(ksin\theta sin\emptyset-\beta)} cos\emptyset \tag{5-8}$$

$$H_\theta = -\frac{E_\emptyset}{\eta} \tag{5-9}$$

$$H_\emptyset = \frac{E_\theta}{\eta} \tag{5-10}$$

Due to the large electrical height of the wire above the PEC ground plane, the phase constant $\beta \approx k$ and therefore equations 5-7 and 5-8 become

$$E_\theta = -j\omega\mu I_0 l \frac{e^{-jkr}}{4\pi r} e^{j\frac{kl(sin\theta sin\emptyset-1)}{2}} \frac{sin\left[\frac{kl}{2}(sin\theta sin\emptyset-1)\right]}{\frac{kl}{2}(sin\theta sin\emptyset-1)} cos\theta sin\emptyset \tag{5-11}$$

$$E_\emptyset = -j\omega\mu I_0 l \frac{e^{-jkr}}{4\pi r} e^{j\frac{kl(sin\theta sin\emptyset-1)}{2}} \frac{sin\left[\frac{kl}{2}(sin\theta sin\emptyset-1)\right]}{\frac{kl}{2}(sin\theta sin\emptyset-1)} cos\emptyset \tag{5-12}$$

To determine the fields that are valid only above the infinite PEC ground plane, each of the equations 5-9 to 5-12 are multiplied by an array factor given by

$$F = e^{jkhcos\alpha} - e^{-jkhcos\alpha} = 2j\left(\frac{e^{jkhcos\alpha} - e^{-jkhcos\alpha}}{2j}\right) = 2jsin(khcos\alpha) \tag{5-13}$$

The resulting field equations can then be used to determine the time-average radiated power density according to the definition of the Poynting vector i.e.

$$\bar{S} = \frac{1}{2}\bar{E} \times \bar{H}^* = \frac{\left(E_\theta H_\emptyset^* - E_\emptyset H_\theta^*\right)}{2}\hat{a}_r$$

$$= \frac{\eta|I_0|^2}{2\pi^2 r^2}\sin^2(khcos\alpha)\sin^2\left[\frac{kl}{2}(sin\theta sin\emptyset - 1)\right]\left(\frac{\cos^2\theta\sin^2\emptyset+\cos^2\emptyset}{(sin\theta sin\emptyset-1)^2}\right)\hat{a}_r \qquad 5\text{-}14$$

From equation 5-14, a normalized pattern function can be written as

$$s = \sin^2(khsin\theta sin\emptyset)\sin^2\left[\frac{kl}{2}(sin\theta sin\emptyset - 1)\right]\left(\frac{\cos^2\theta\sin^2\emptyset+\cos^2\emptyset}{(sin\theta sin\emptyset-1)^2}\right) \qquad 5\text{-}15$$

which, when plotted as a function of ϕ and θ, gives the azimuthal and elevation radiated power patterns for the simple long-wire antenna. Far-field radiation patterns are defined according to the spherical coordinate system. The azimuth patterns are obtained at a given elevation angle θ with a variation of azimuthal angle ϕ ($0 \leq \phi \leq 2\pi$), which is measured from the *x*-axis towards the *y*-axis on the *x*-*y* plane. The two-dimensional elevation patterns, on the other hand, are plotted at a specific azimuthal angle ϕ as a function the elevation angle θ ($-\pi/2 \leq \theta \leq \pi/2$), which is measured from the *z*-axis towards the *x*-*y* plane.

The analysis that has been presented here only considered a very simple long-wire antenna above an infinite PEC ground plane. However, in some cases, such as the power-line radiation problem, the physical geometries are quite complex due to, for example, the presence of both vertical and horizontal wire conductors, multi-conductor configurations *etc*. Their pattern functions become too complex to be mathematically expressed in closed form like that of a single wire case. Numerical electromagnetic computational models are ideal for analysing the radiation characteristics of such configurations.

5.4 Power line simulation/computation

A commercial EM simulation software FEKO [14] solves the integral equations using Method of Moments (MoM) incorporating the Rao–Wilton–Glisson (RWG) basis functions [49]. This is a standard tool for handling numerical integration of the Maxwell's equations with appropriate boundary conditions on wire structures and lossy ground planes [50]. It has been applied here to evaluate the current distribution along the power lines to obtain the radiated fields. The radiation characteristics of these lines depend on such factors as the frequencies of the source, line length, spacing between the conductors, line impedances, line topology, presence or absence of grounding conductors, ground properties and type of terrain, position of the source along the line, measuring antenna heights *etc*. Quite often, most of these factors will vary throughout the length of a long line and thus affect the interference levels of the radiated noise. Various line configurations were modelled to understand their radiation characteristics. This was done while varying the above-mentioned parameters to determine their contribution to the far field radiated energy from the lines.

5.4.1 Single wire radiation over a PEC ground plane

To test the reliability of this computational code in analysing the radiation properties of long wires such as those of overhead power lines, a simple configuration was simulated. The resulting far field patterns were then compared to the analytical ones as were computed in the previous section. An example of the configuration of the simulated problem involved a single wire above a PEC ground plane. The wire was placed horizontally along the y-axis, parallel to the ground plane at a height of 2λ, with a diameter of 2 cm and a length of 16λ. λ is the free space wavelength at the simulation frequency. The line is terminated at one end with its characteristic impedance Z_L and fed at the other end through a voltage source. The source is defined on a discrete port with a driving port impedance of Z_s as illustrated by Figure 5-3.

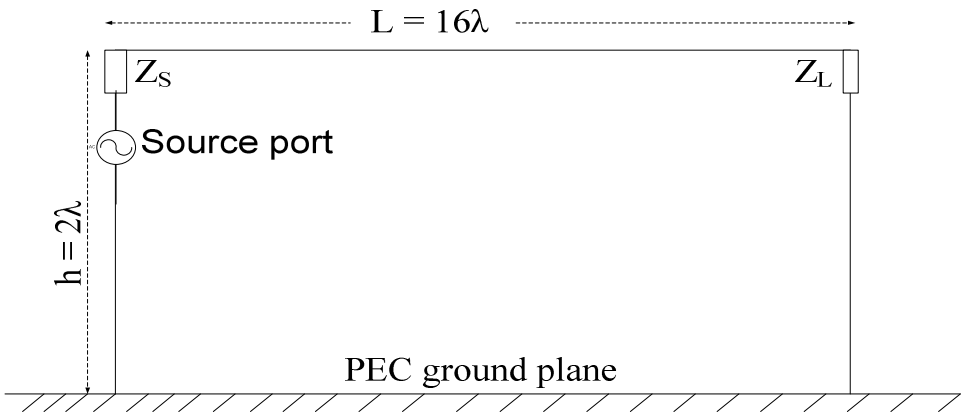

Figure 5-3: Simulated single wire configurations above an infinite PEC ground plane

In this example, since the height of the line above the ground is greater than the wire radius, the thin-wire approximation would be suitable for describing the currents along the wire. Briefly, in this simulation the line is subdivided into small segments, the size of which depends on the shortest wavelength used for field calculation, which in turn affects the computation time. The infinite PEC ground is modelled using the method of reflection coefficient approximation [14]. The currents on each wire segment are numerically calculated and used to derive the radiated fields.

The radiated field generated by this wire configuration is given in the form of the far-field pattern as shown in Figure 5-4. This figure shows the normalized radiation pattern on the elevation plane at $\phi = 90^0$ as a function of elevation angle θ. This pattern is also compared to that obtained analytically through the procedure derived in section 5.3. Both results show clear pattern lobes and nulls with the peak of the main lobe being at about 85^0. The comparison of the normalized azimuthal patterns, obtained from the simulation and the analytical calculation, is given in Figure 5-5. The difference in the azimuthal patterns is attributed to the vertical grounding conductors, which are not included in the analytical approach. The agreement achieved between the analytical and simulated results for a simple problem of a long wire above a PEC ground plane gives an indication that the use of the EM

code can also be extended to other problems such as those involving multiple conductors above PEC ground planes.

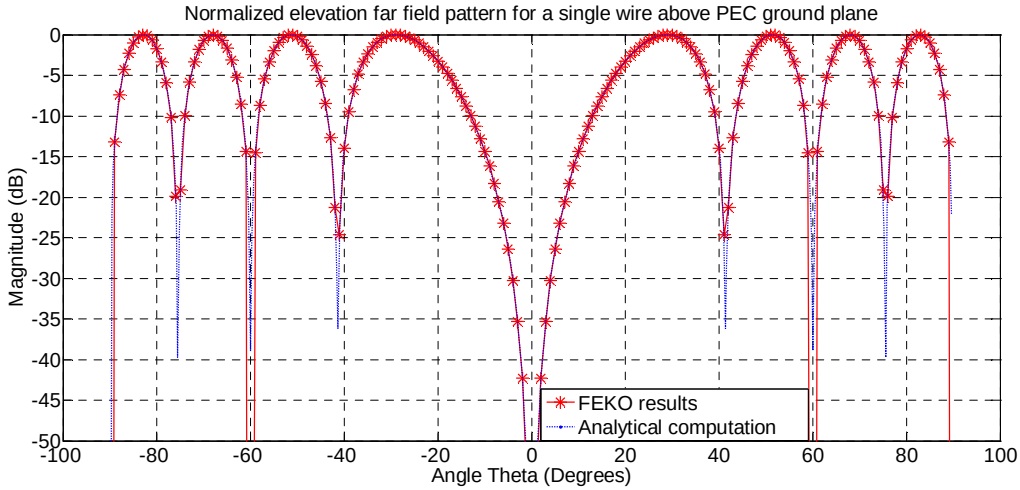

Figure 5-4: Normalized elevation pattern for a 16λ long single wire above an infinite PEC ground plane at $\phi = 90^0$

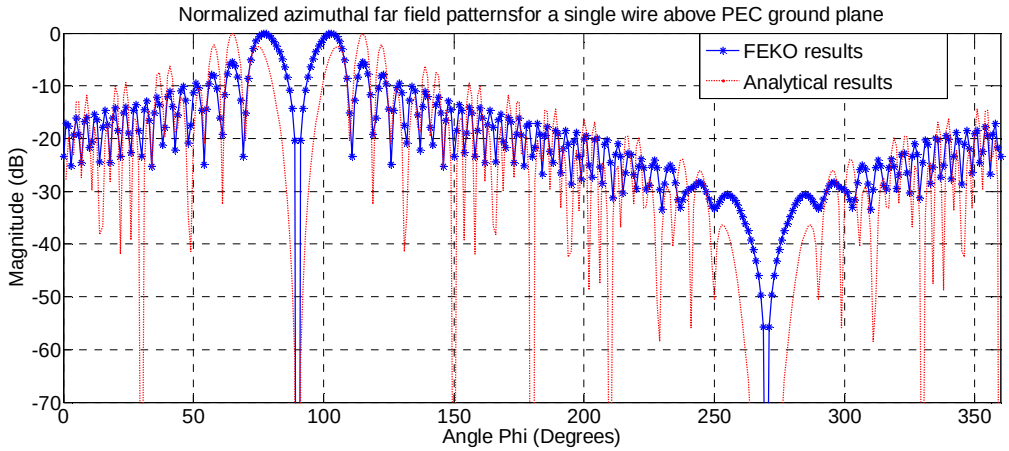

Figure 5-5: Normalized azimuthal far-field pattern for a 16λ long single wire above an infinite PEC ground plane at $\theta = 89^0$

5.4.2 Single wire radiation over a Lossy ground plane

To further demonstrate the reliability of the code in analyzing electrically large structures, a comparison between simulation and analytical results for a long horizontal line above a lossy ground plane is made. Here, the analytical computation, done by Taheri *et al* [51], of radiated electric field from an overhead transmission line, having a geometrical configuration shown in Figure 5-6, located above a lossy ground is used. The line length is 100 m and is horizontally placed at 5 m above the ground that is characterized by $\sigma = 0.04$ S/m and $\varepsilon_r = 4$.

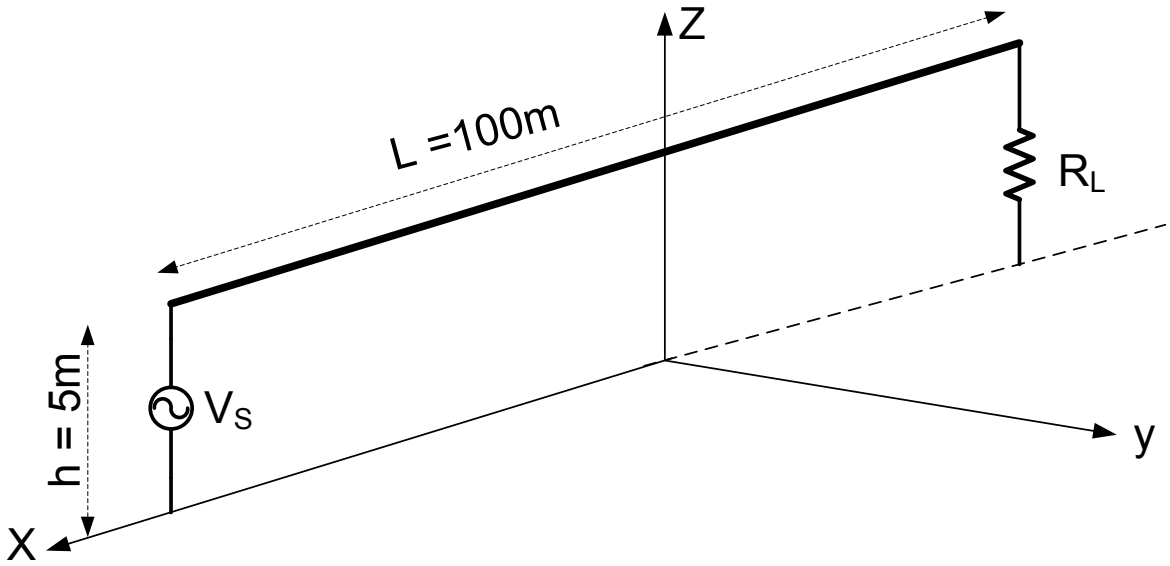

Figure 5-6: Geometry of an overhead transmission line analysed by [51]

Taheri *et al* [51] calculated the components of the radiated electric field along the line axis at the observation points located at y = 6 m, z = 2 m and x varied from -20 to 20 m. The voltage source V_S has a magnitude of 1 V and the termination resistor R_L = 10 kΩ. Complex image theory was used in the calculation where the finitely conducting ground is replaced with a perfectly conducting one that is at a complex depth of $d/2$, where $d = 2/\gamma = \delta(1 - j)$. δ is the ground's skin depth, while γ is the propagation constant in the ground. Typical magnitudes of the electric field components, at the given observation point and at a frequency of 10 MHz, which are combined contributions by the line and its image, are as shown Figure 5-7.

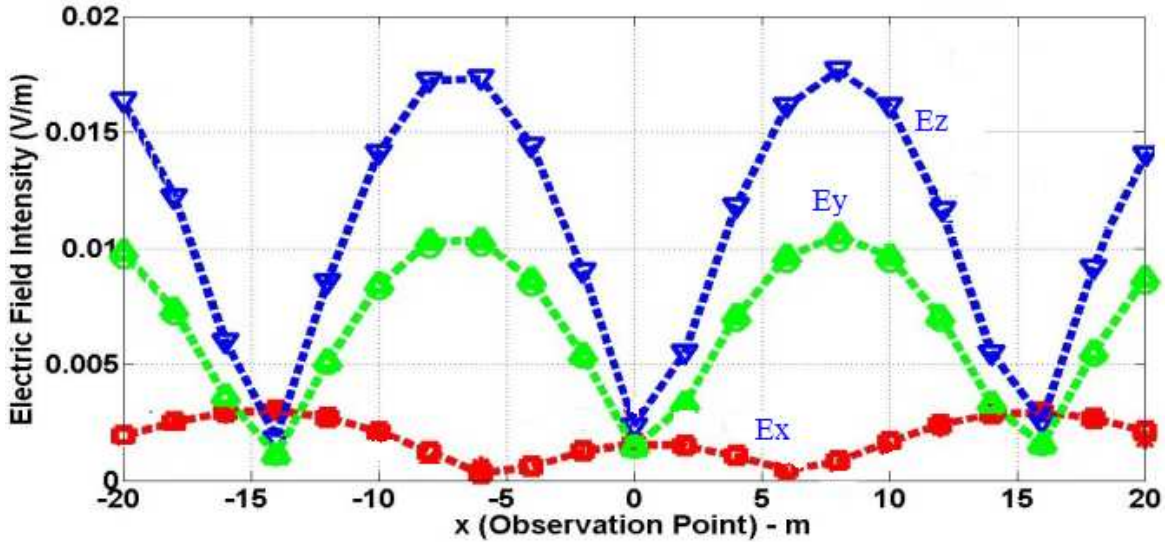

Figure 5-7: Radiated electric field components as computed by Taheri *et al* [51]

A model similar to that given in Figure 5-6 was replicated and simulated in FEKO at a frequency of 10 MHz and the resulting field components are as shown in Figure 5-8. The ground plane was defined using a Sommerfeld integral method with characteristics as for the above model. The Sommerfeld method solves exact boundary conditions of a defined structure using the appropriate Green's function to determine the exact solution for the radiated fields in the presence of the ground plane [14].

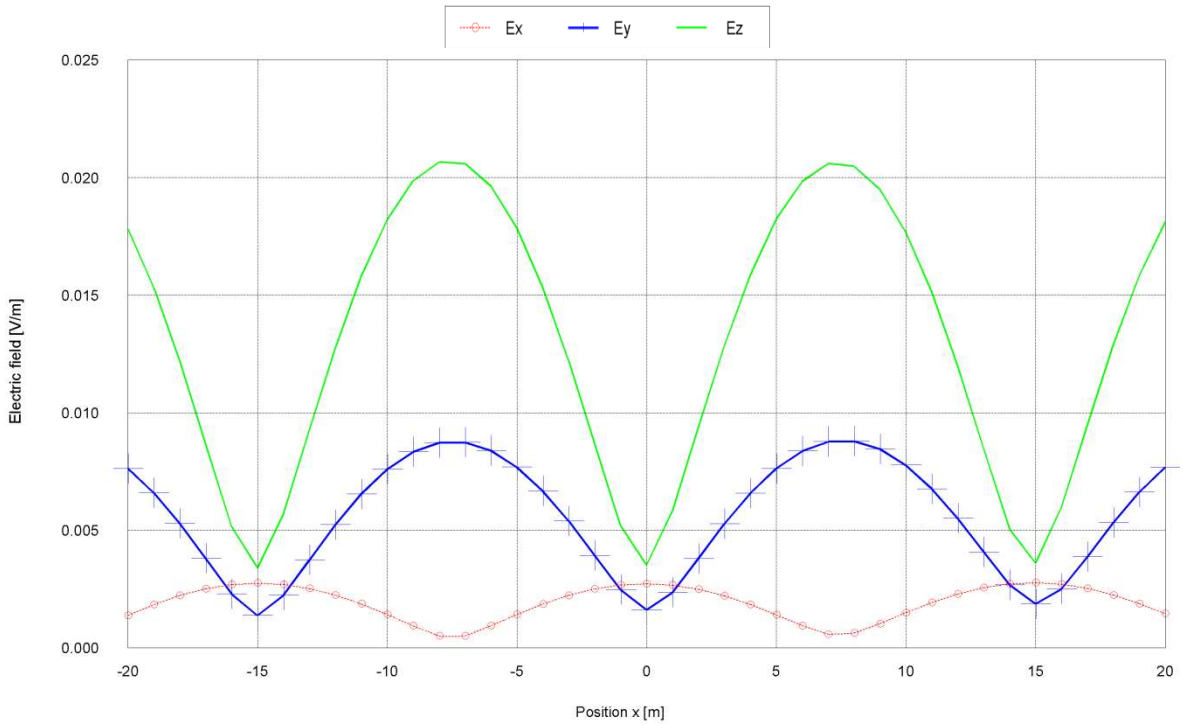

Figure 5-8: FEKO simulation of the electric field components distribution along the line axis (y = 6 m, z = 2 m) for the line geometry given in Figure 5-6

Both Figure 5-7 and Figure 5-8 show similar electric field distribution results. This correlation between the analytical results and the FEKO simulations for a similar long-wire configuration provides confidence in the use of the EM code to determine the radiation characteristics for even more complex problems. For the purpose of this research, the code is applied to analyse the radiation characteristics of a three-wire configuration to simulate the behaviour of a power line due to the presence of a sparking source.

5.4.3 Multi-conductor radiation over a ground plane

In this subsection, the radiation characteristics of a multiconductor configuration located above a ground plane are evaluated through FEKO simulation. This is aimed at examining the radiation behaviour of a multi-wire system due to a signal source such as sparking. A 3-wire line, representing a power line located above either a PEC or a lossy (Sommerfeld) ground

plane, is used. The simulation investigates the line radiation properties, focussing on the effect on the far-field radiation patterns due to such factors as the ground properties, line length, line impedances, position of the source along the line, frequencies of the source, line topology, *etc*.

5.4.3.1 Power line electromagnetic model description

The power-line was modelled computationally as an antenna radiator and was configured with three equal length PEC wires placed on the z = h plane in the air above the surface, z = 0, of the ground. The conductors were oriented along the *y*-axis and placed horizontally parallel to each other, as shown in Figure 5-9a, to represent a simplified version of a horizontal type power line. Various line lengths were considered to evaluate their influence on the radiation patterns. A perfectly conducting ground plane, PEC, was used in this instance. At the Karoo site, the power lines are located above real earth, which is a non-ideal conductor. The effect of this finitely conducting ground has to be investigated. This was considered using a dielectric medium as a ground and applying the Sommerfeld integral method. The relative permittivity (ε_r) and the electric conductivity (σ) of the ground plane can be defined computationally for the problem to be simulated. For the case of the earth as the ground, it is often represented as homogeneous and flat with typical values in the range of $\varepsilon_r = 5 - 100$ and $\sigma = 10^{-4} - 1$ S/m [46,52]. Generally, ε_r is a complex quantity that has both real and imaginary parts and the absolute permittivity ε ($\varepsilon = \varepsilon_0\varepsilon_r$) can be represented by the following convention [53]:

$$\varepsilon = \varepsilon' - j\varepsilon'' \qquad 5\text{-}16$$

where ε' and ε'' are the real and imaginary parts, respectively, and the constant $\varepsilon_0 = 8.854$ pF/m.

According to the measurements made by Otto *et al* [54], the ground properties of the Karoo site can be approximated by a loss tangent ($\tan\delta$) of 0.076 and $\varepsilon' = 3.8$ with imaginary $\varepsilon'' = 0.9$. A unity relative permeability is assumed. The values of $\tan\delta$ and ε_r can be inserted into the computational model that use earth as the ground plane.

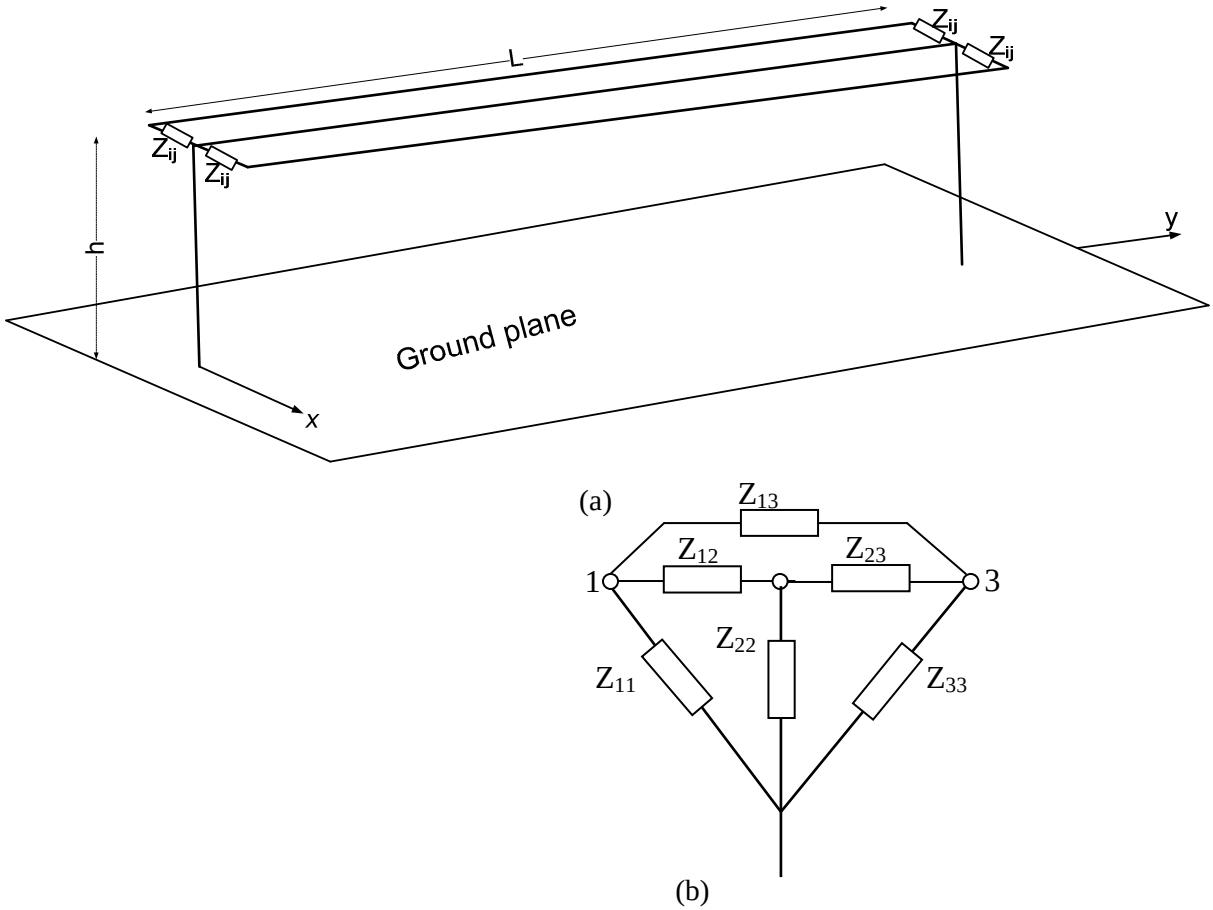

Figure 5-9: (a) Sketch of computational configuration of the modelled power line and (b) a schematic of the end terminations

The excitation point of the modelled line was varied along one of the conductors and also from the middle wire to one of the outside ones. This simulates the line radiation characteristics due to a source from the line hardware, which could be located at one of the power line poles along the line length. For the purpose of the simulation, a voltage source of 1 V is used as an excitation at these various positions along the line.

To simulate the presence of mismatched conditions on the line, various impedances were placed at the end of each conductor with vertical ground wires, which in the real-world run up an electric-utility pole, as shown in Figure 5-9b. These impedances were connected either

differentially between two conductors or in common mode (between one conductor and the ground). The latter is the self-surge impedance of each of the conductors in the absence of the other conductors while the former is the mutual surge impedance between the corresponding conductors. For a multi-conductor line such as that of Figure 5-9a, these impedances can be calculated from the geometrical configuration of the line.

Consider a geometrical model of an *n*-conductor line given in Figure 5-10, with the n^{th} wire located in free space at $z = h_n$ above a homogeneous earth and at a horizontal position $x = x_n$ relative to a reference plane that is perpendicular to the ground plane. Each of the conductors has a radius of *a*, and they are parallel to each other and to the *y*-axis. The homogeneous earth and the conductors have, respectively, permittivity ε_g, ε_c, conductivity σ_g, σ_c, and permeability μ_0.

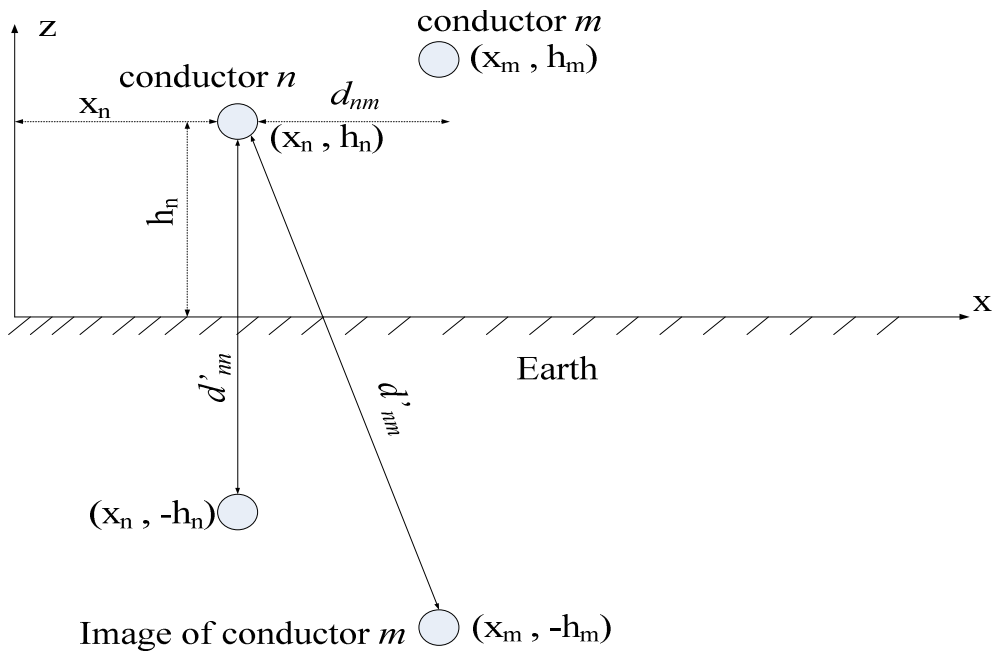

Figure 5-10: Geometric model for an n-conductor line above a homogeneous earth

The self and mutual per-unit-length (p.u.l) ground impedances for this configuration can be approximated in a matrix form using the following expression, which is an approximation of the Carson's integral equation [55,56,57]:

$$Z_{nm} = \frac{h_n + h_m}{\pi\left(d_{nm}^2 + (h_n + h_m)^2\right)} \sqrt{\frac{j\omega\mu}{\sigma_g + j\omega\varepsilon_g}} \qquad 5\text{-}17$$

Here, Z_{nn} (for $n = m$) are the self impedances, Z_{nm} (for $n \neq m$) are the mutual impedances, while d_{nm} is the horizontal distance between two conductors n and m. From equation 6-18, the series ground impedance reduces to:

$$Z_{nm} = \frac{1}{2\pi h_n} \sqrt{\frac{j\omega\mu}{\sigma_g + j\omega\varepsilon_g}} \qquad 5\text{-}18$$

These expressions were developed by Semlyn [55] and can be applied within the limits of transmission line approximations. According to [56], the limiting condition is given by $\lambda \geq 2(h+\delta)$, where h is the height of the wire above the ground and δ is the ground's skin depth. λ is the wavelength of the EM wave propagating, at a given frequency, in the wire. Above this frequency, the line current does not have an earth return but the return is confined within the region surrounding the wire thus exciting radiation modes. The following subsection presents the influence of varying the line terminating impedances on the radiated field patterns.

5.4.3.2 Effects of terminating impedances on power line radiation patterns

To simulate the influence on the radiation characteristics by the degree of impedance mismatches and line discontinuities, various impedances were connected at the ends of the line conductors. Since, in general, power lines are not matched for the propagation of high frequency signals, this simulation is to evaluate the effect due to line impedances, which could be very high, very low or matched cases depending on the interconnections along the line. Four similar models using infinitely long PEC ground planes were considered. Each model had 200 m long conductors at 12 m above the ground and the excitation voltage source port was placed at the end of the middle conductor. Three models had their termination

impedances set to Z = 500 Ω (which is approximately equal to the characteristic impedance each conductor), 1 MΩ, 10 kΩ, respectively, while the fourth one was short circuited at its ends.

Simulations were done at some discrete frequencies and typical results for the non-normalized azimuth and elevation far-field patterns at a frequency of 100 MHz are given in Figure 5-11. The various impedances introduce different degrees of mismatches in the line causing reflection of the propagating wave, which creates components of standing waves. These impedances will cause changes of the radiated field levels, as depicted in Figure 5-11, but the pattern lobes' maximums and nulls remain substantially at the same angular positions. Based on this, the subsequent simulations will use models with termination impedances of 500 Ω.

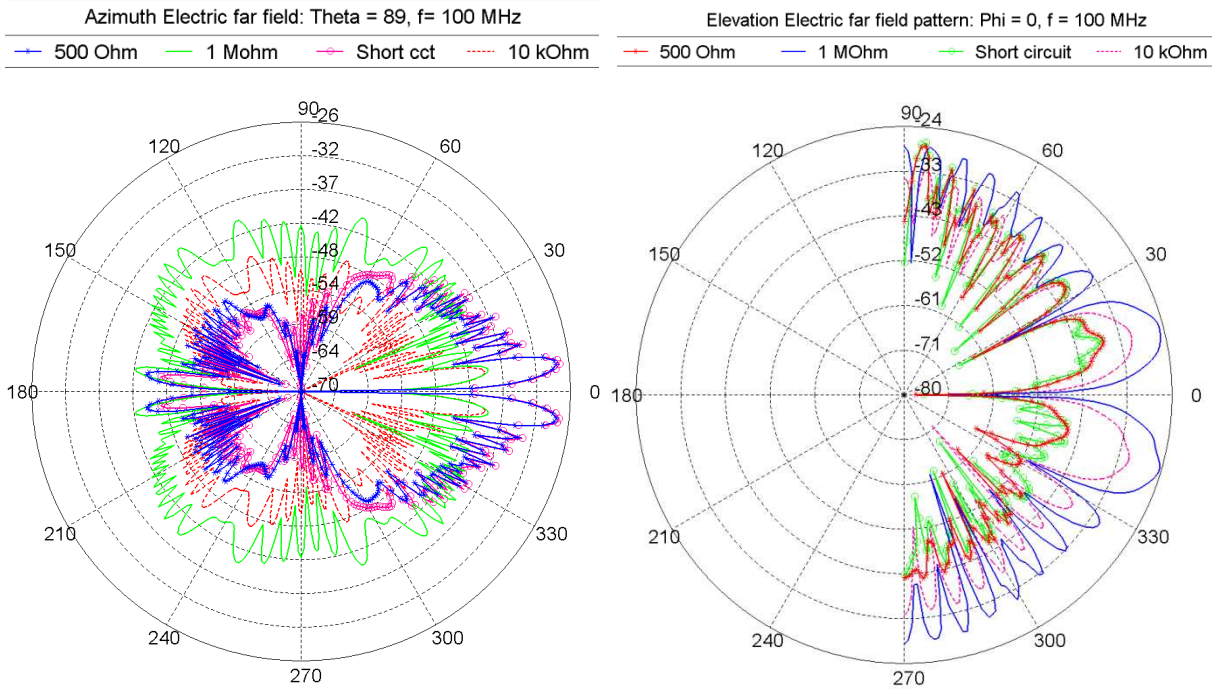

(a) (b)

Figure 5-11: (a) Azimuth and (b) Elevation electric far-field radiation patterns variation with termination impedances

5.4.3.3 Effect of ground plane properties on simulated power line radiation patterns

The effect of the ground plane on the line radiation properties was evaluated for the 3-wire model. Here, the conductors used were 200 m long and were placed 12 m above either a PEC or a lossy (Sommerfeld) ground plane. The simulation is used to check the effect of the real ground properties on the radiation patterns of the line in comparison to the PEC ground. The ends of the wires were terminated with impedances of 500 Ω and an excitation port, with a discrete voltage source of 1V, placed at the end of the middle conductor to simulate a sparking source on the line. The characteristics of the lossy ground used were $\tan \delta = 0.076$ and $\varepsilon_r = 3.8$. The radiation characteristics from the line models for the two different ground planes were compared. This was necessitated by the huge computation resource requirements for simulating a large problem above a Sommerfeld ground plane. The comparisons are used to determine whether subsequent models need to use the real ground simulation or not.

Two similar models were considered representing the lines with PEC and lossy ground planes, respectively. Simulations were done at various discrete frequencies and typical azimuth and elevation far-field patterns are given in Figure 5-12 for the two models at 100 MHz. In these cases the conductors were oriented along the x-axis, i.e. the conductors lie along the $\phi = 0^0 - 180^0$ axis with the source point on the 180^0 side. The ground effects are evidently shown on these patterns, which are not normalized. The PEC ground model has a unity reflection coefficient but that of the lossy ground varies depending on the angle of the radiated wave and the ground parameters. Since the radiating conductors are in horizontal orientation, the horizontal reflection coefficient for most of the observation angles approaches that of the PEC. This results in the two models having similar patterns. This can be seen from the shape of the azimuth patterns as given in Figure 5-12 and can also be confirmed from the simulations results shown in Figure 5-13 and Figure 5-14, for 500 MHz and 20 MHz representing high and low frequencies, respectively. The corresponding normalized patterns overlaid on each other shows that the lossy ground used does not significantly affect the azimuthal patterns.

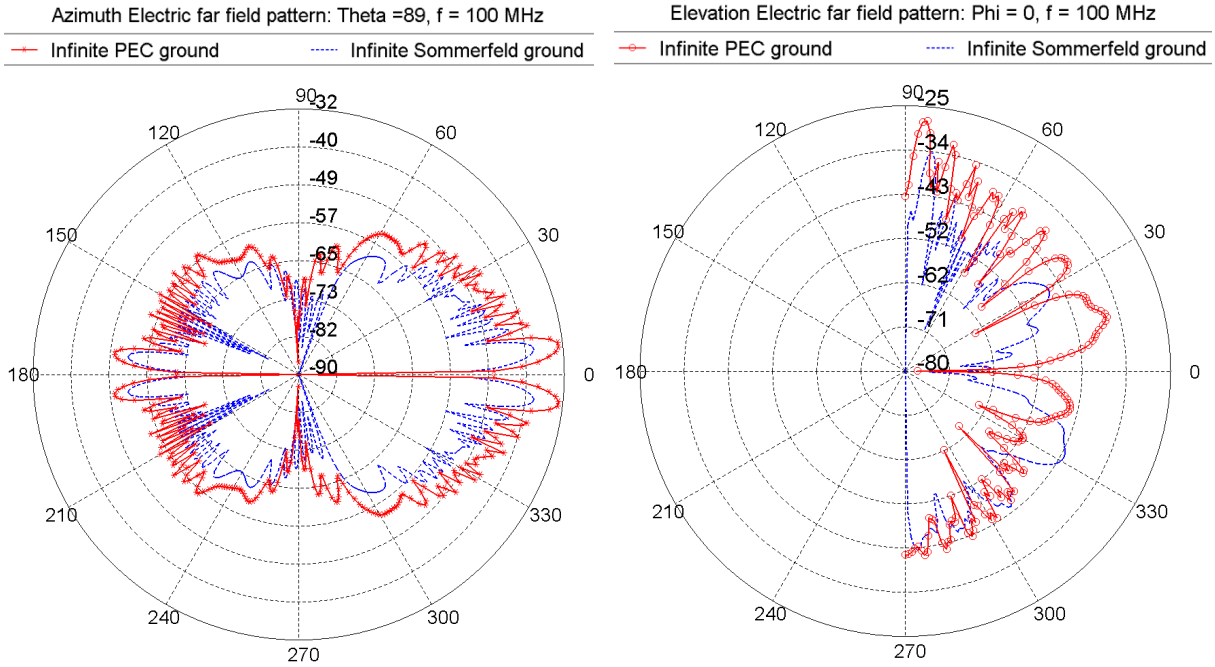

Figure 5-12: Azimuth (left) and elevation (right) electric far-field patterns for 3-wire lines above PEC and Sommerfeld ground planes at 100 MHz.

The elevation patterns given in the three figures show the radiation viewed looking at the end of the line i.e. at $\phi = 0^0$ with the line oriented in the $\theta = 270^0$ to 90^0 direction. The in-phase out-of-phase effect from the combination in the vertical plane of the reflected and the direct waves can be seen. At some elevation angles the direct and the reflected waves are in phase, i.e. their maximum field strengths arrive at the same distant point at the same time and in the same direction. Their combination will result in the reinforcement through addition of their intensity at the given angle. At other elevation angles, these waves are totally out of phase i.e. they arrive at a distant point at the same instant with the same amplitudes but different directions. Their combination will result in the cancelation of the field intensities at the given angle. The field strengths will be at intermediate levels at other angles where the waves are not completely in- or out-of-phase. Depending on the electrical characteristics of the ground, the waves will undergo a change in both phase and amplitude in the reflection process. The

difference in the ground properties will result in the varied angular positions of the lobes and nulls and also the change in the field strength levels.

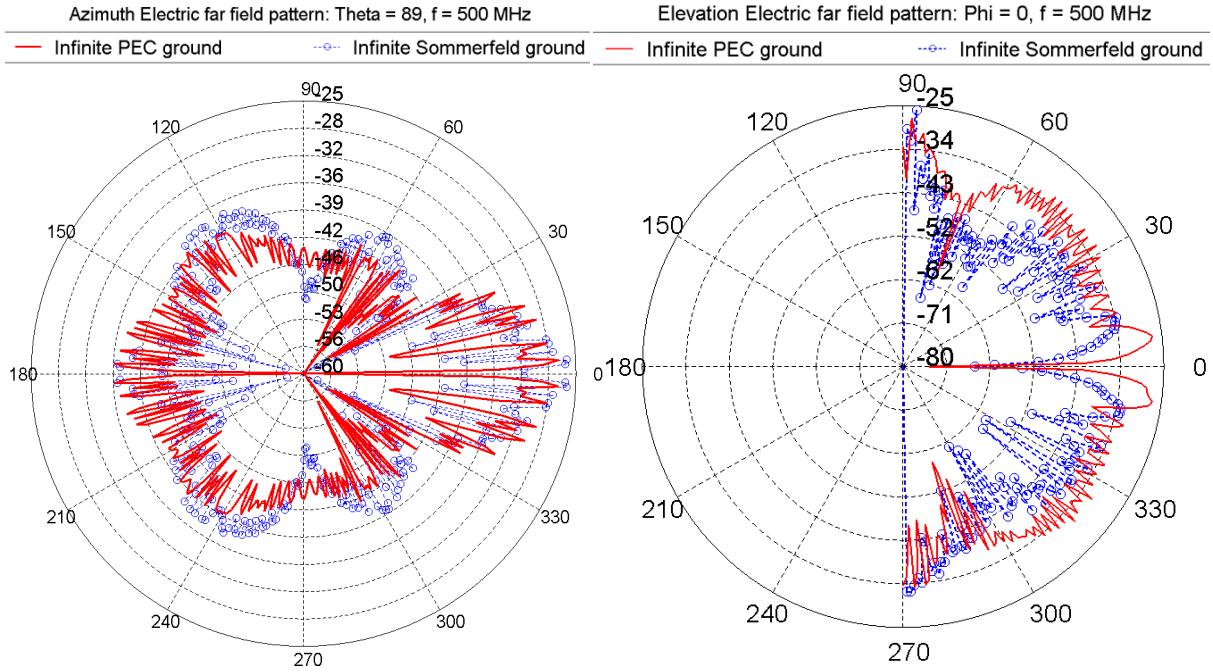

Figure 5-13: Azimuth (left) and elevation (right) electric far-field patterns for 3-wire lines above PEC and Sommerfeld ground planes at 500 MHz.

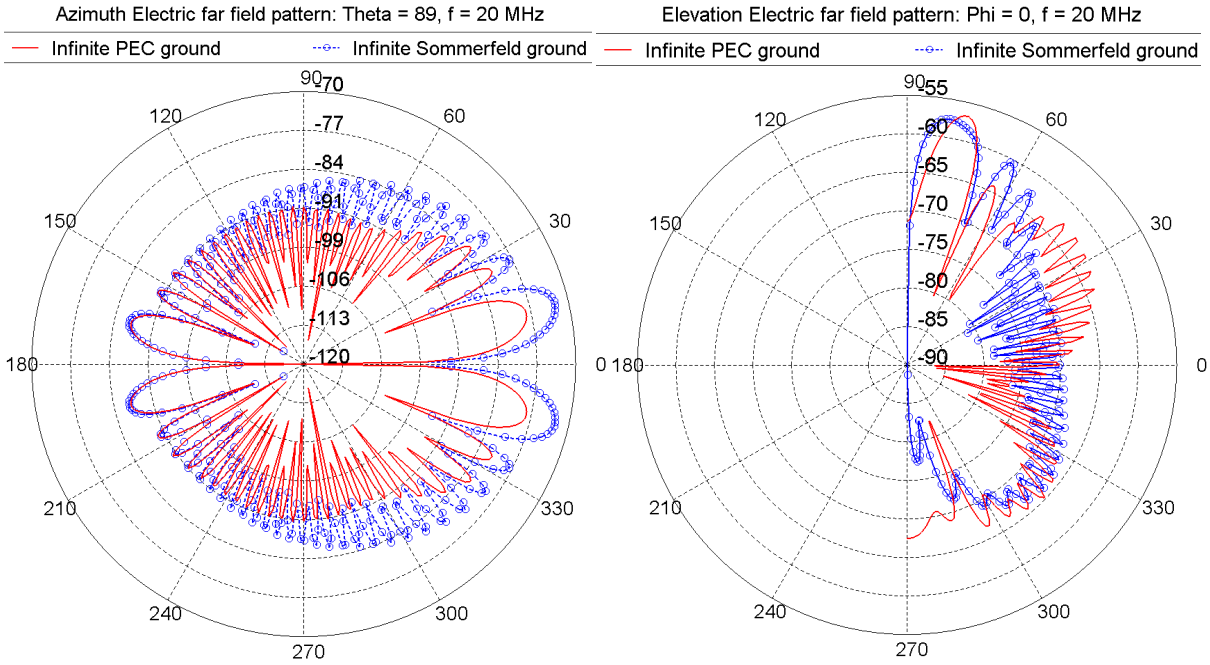

Figure 5-14: Azimuth (left) and elevation (right) electric far-field patterns for 3-wire lines above PEC and Sommerfeld ground planes at 20 MHz.

5.4.3.4 Effect of source position on the radiation patterns

The far-field radiation patterns were evaluated for cases where the excitation position was varied along the line. This is to simulate a sparking source occurring at an arbitrary position on the line. Similar 200 m long conductor models as previously defined, above infinite PEC ground planes, were used with an excitation position at the centre, at one end and at 50 m from one end of the middle conductor. The position of the source was also moved to one of the outer conductors. The radiation characteristics of the latter line configuration were compared to that with the source at the same position on the middle conductor. This gives an indication of the how the radiation patterns are affected when a noise source is attached to either the middle or one of the outer conductors. In all these cases, the source port was connected between the line conductor and the ground via a vertical wire.

Figure 5-15a shows typical azimuth far field patterns for the models, with the source on the middle conductor, simulated at 100 MHz. These graphs show that the field strength levels are more symmetrical on both sides (top & bottom) of the plot due to the symmetry about the line axis, which is along 0^0 – 180^0. It can also be seen that there is symmetry on both sides (left and right of the graph) for the model with the feed at the centre of the line as compared to the offset one. The model with its source at the end of the middle conductor, for example, has its maximum field strength pushed in the direction away from the source end resulting in an unsymmetrical pattern.

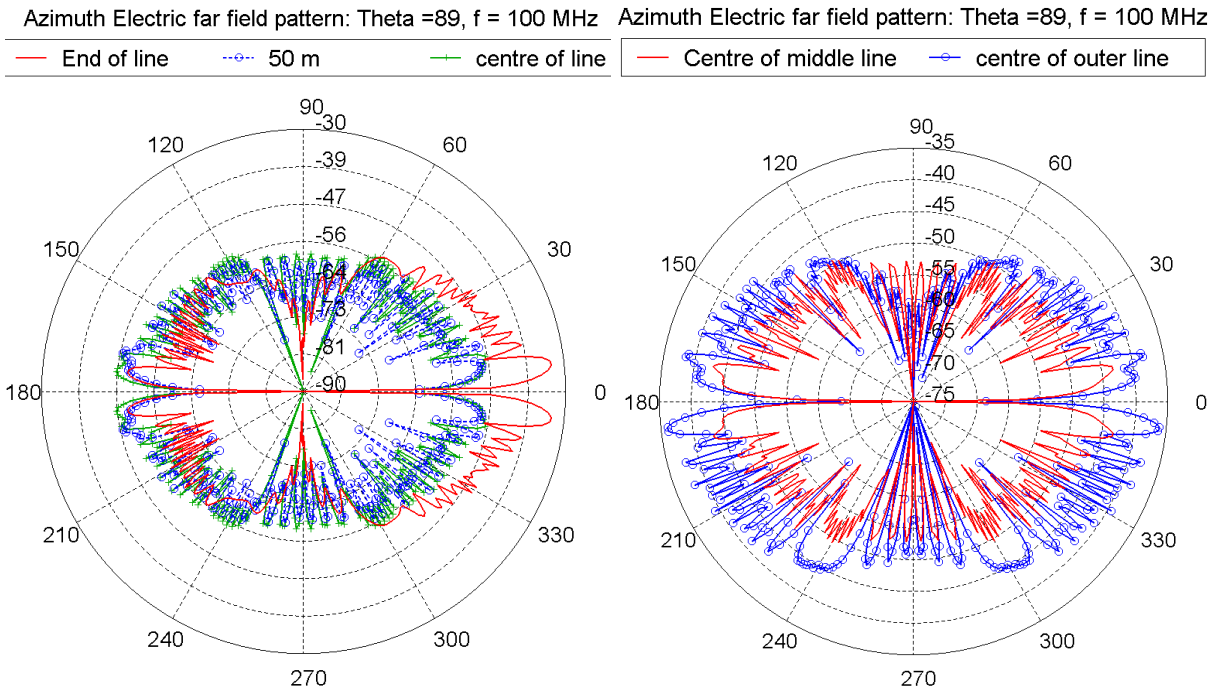

Figure 5-15: Azimuth far field patterns variation with excitation position on the line at 100MHz

In Figure 5-15b the typical azimuth far field patterns for the models with the source at the centre of the middle and outer conductors, simulated at 100 MHz are plotted. At the plotted elevation angle of 89^0, the source port is on the upper side of the plot for the model with its feed on the outer conductor. The wires are oriented along the 0^0 – 180^0 axis. It can be seen that there is a higher field strength level on the side of the outer conductor opposite to where

the source is attached. This geometry of three conductors forms an antenna array with the wire attached to the source being the main radiator while the others, which are coupled to the main one either reactively or through the mutual impedances, act as parasitic radiators. The radiation from these parasitic elements will reinforce that from the main radiator. This occurs in the direction of the main elements' pattern resulting in a beam that is pulled to one side as depicted in Figure 5-15b. The symmetrical environment around the centre conductor for the model with source on the middle conductor makes the radiation patterns balanced on both sides of this conductor, i.e. the upper and the lower portions of the plot.

5.4.3.5 Effect of line configuration (with bends) on power line radiation patterns

The far-field characteristics were evaluated for a line that has bent sections, and compared to a straight line of the same length and a similar source position from one end. The real-world power-line installations are more complex having bends and branches from at least one of its phases. Two line configurations, shown in Figure 5-16, were considered in this simulation. The total length of each of the three conductors in each model is 1135 m and an excitation source is placed at 205 m from one end of the middle conductor. The line with bent sections represents the Klerefontein test-line shown in Figure 3-8 with the excitation position at point SG. PEC ground planes were used for these models.

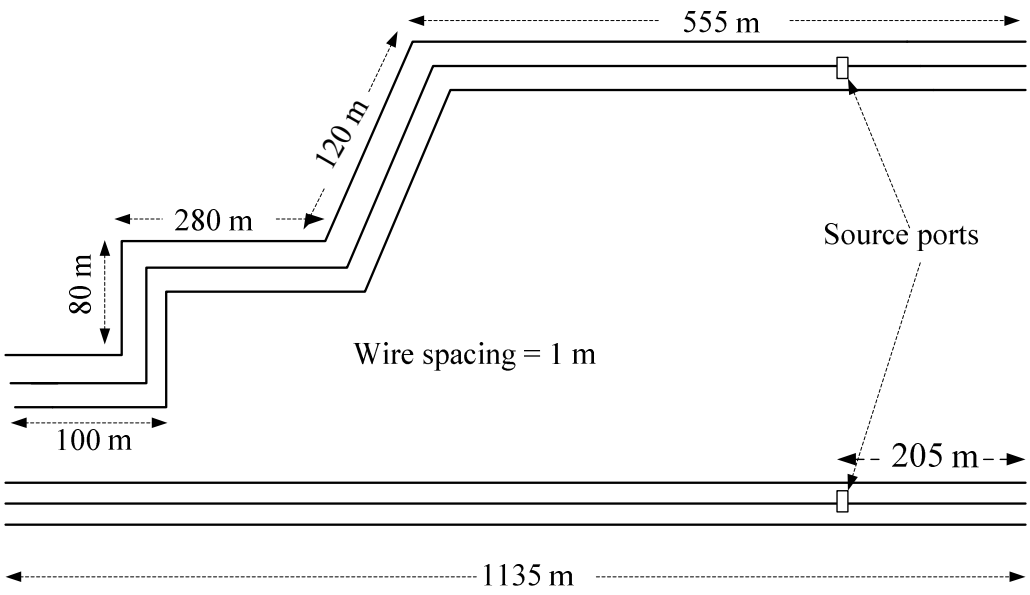

Figure 5-16: Straight (lower section) and bent (upper section) line configurations. The configuration of the upper section reflects that of the Klerefontein test line.

The typical azimuth and elevation far field patterns for the two models are given in Figure 5-17 (left and right, respectively) simulated at a frequency of 100 MHz. It can be seen that changing the configuration of the line greatly varies the radiation pattern shape and field strength, especially on the azimuthal axis. The line model with bent sections shows a complex azimuth pattern. The bending of the line changes the direction of the propagated currents causing radiation in different directions from each of the bent line sections. This results in the combination, through reinforcement and subtraction, of the field strength at a distant point in a manner that will be different from that of the straight-line geometry. The main beam, however, follows the general orientation of the entire line as depicted in Figure 5-18 where the azimuth pattern of Figure 5-17 has been reproduced in 3-dimensional.

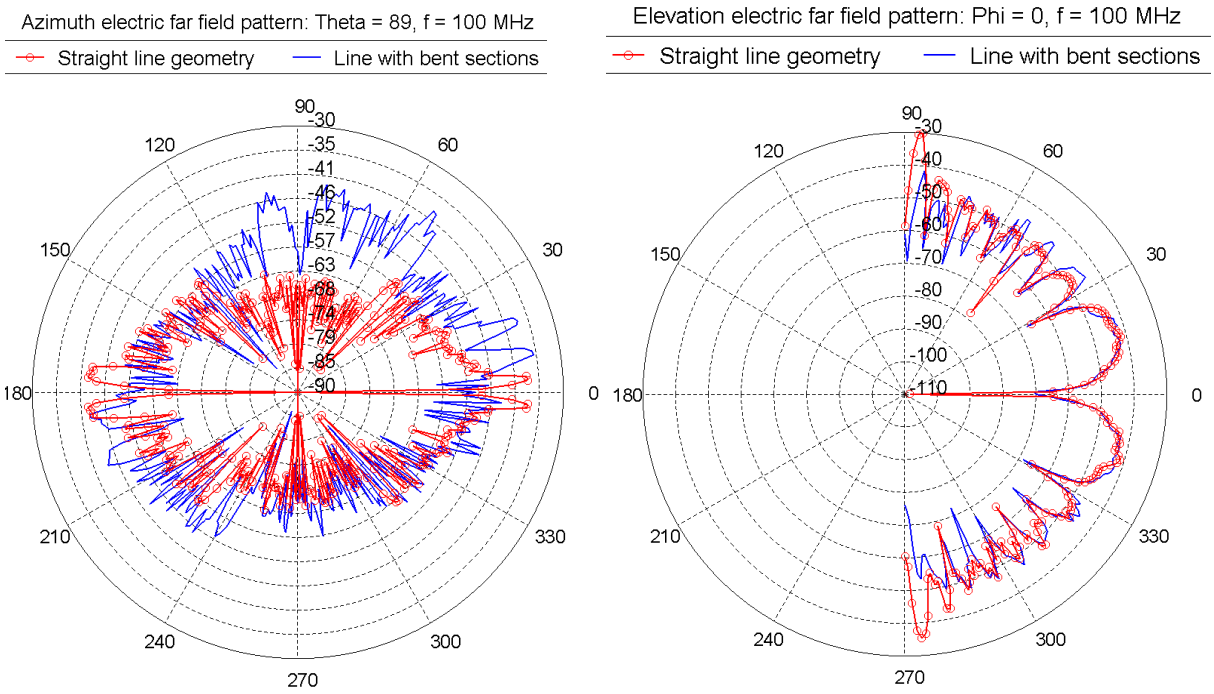

Figure 5-17: Radiation pattern variation with change in power line configuration

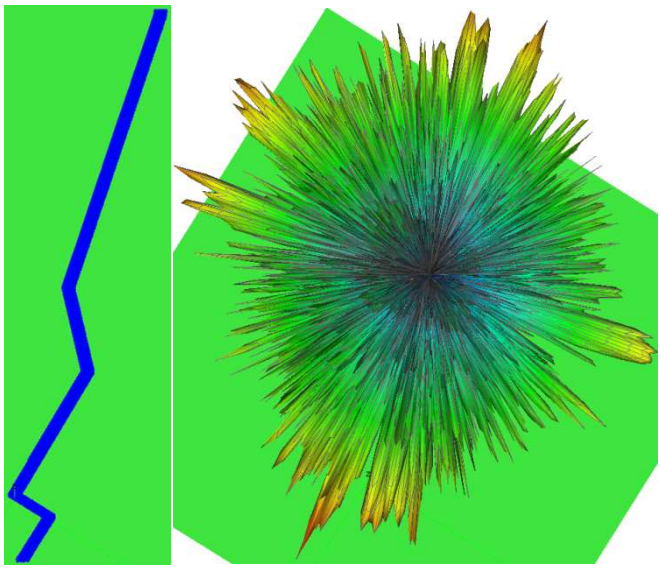

Figure 5-18: A 3-dimensional representation of the radiation pattern due to line with bends

5.4.3.6 Variation of radiated electromagnetic field with line length

The influence of the variation of the radiating line length on the radiation patterns was investigated. This was done by using a 200 m and a 100 m long power line models with a source at the end of the middle wire. Both models use an infinitely long PEC ground plane with equal impedances of 500 Ω terminating the lines. The simulated azimuth and elevation radiated patterns for these two lines are given in Figure 5-19. From this it can be seen that although the longer line has slightly more side-lobes than the shorter line, they both have similar pattern shapes. This is because at 500 MHz the two line lengths are $L >> \lambda$. From the azimuth and the elevation patterns, the maximum radiation for the longer line is more directed towards the line as compared to that of the shorter line. As the line length increases, the intensity of the main lobe, which is in form of a cone around the line, increases and gets sharper, resulting in the narrowing of the angle of maximum radiation, which is formed between the line axis and the main lobe. This can be seen in Figure 5-20 where radiation patterns for two lines, 1 km and 100 m, are compared at 100 MHz. The azimuth patterns of Figure 5-20 shows that the maximum radiation forms about 3^0 and 10^0 with the line axis for the 1 km and 100 m lines, respectively.

The vertical conductors used as ground wires contribute to the skywards radiation which is seen as the lobes near $\theta = 0^0$ on the elevation patterns. This radiation is seen on all the frequency points considered and the angle of elevation (from the horizontal axis) for this radiation increases with frequency (since the vertical conductors get electrically longer as the frequency increase).

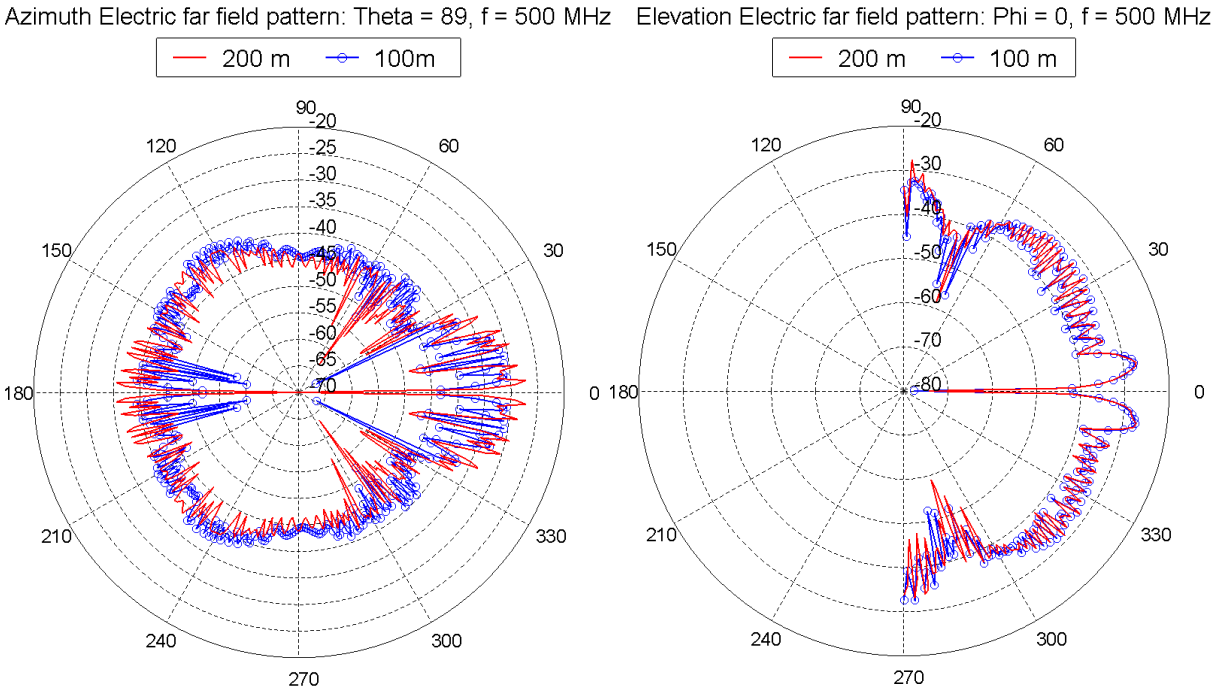

Figure 5-19: Azimuth and elevation electric field patterns for 100m and 200m long lines at 500 MHz with the source at the end of the middle conductor

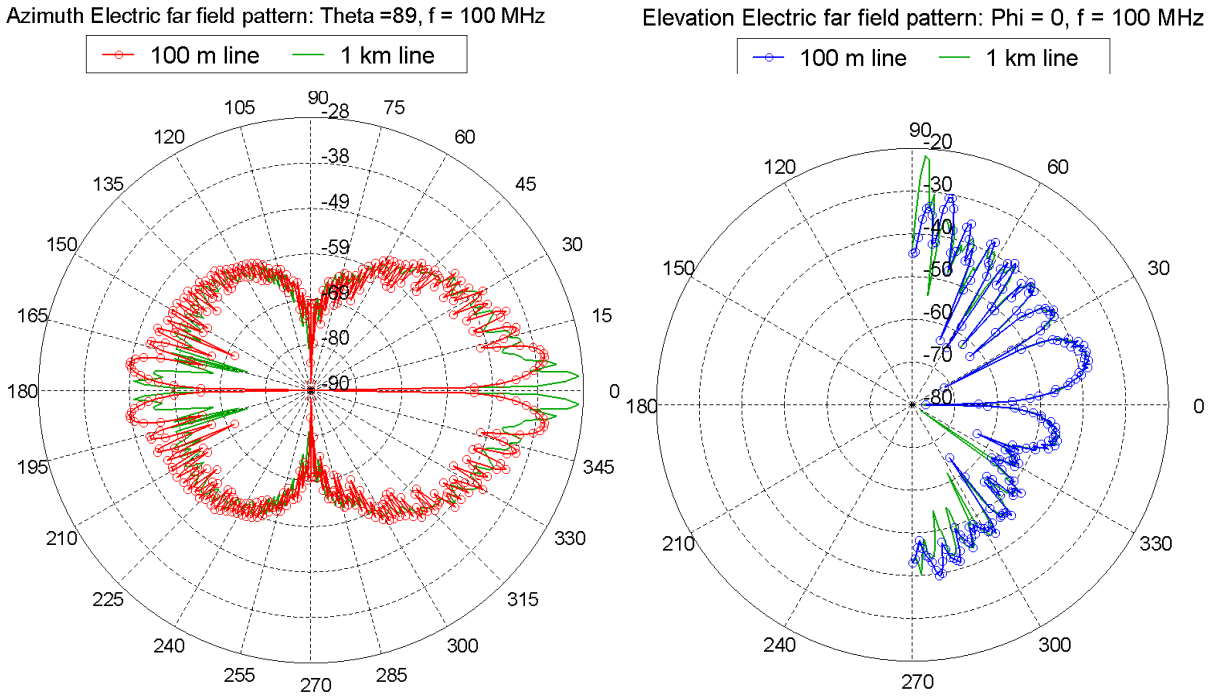

Figure 5-20: Azimuth and elevation far-field patterns for 100 m and 1 km long lines at 100 MHz

Similarly, varying the source frequency, and hence the line length in terms of wavelength, has an effect on the radiation patterns. Figure 5-21 gives the azimuth and elevation far-field patterns for a simulated line model as a function of frequency. The model used here had 200 m long conductors, above an infinitely long PEC ground, with a source point at the end of the middle conductor and the termination impedances of 500 Ω. The simulations were done at various discrete frequencies. Typical patterns for the frequencies of 20, 100 and 500 MHz are plotted here.

The pattern shape, level and orientation vary with source frequency. With the line getting electrically long (in terms of wavelength) with frequency increase, the total amount of radiated energy increases with frequency. The main lobe also splits to form a series of minor lobes, which grows in number and intensity with the frequency increase. Many points along the wire carry currents in different amplitudes and phases and as the line length increases the radiated far field patterns get more complex due to some of the lobes merging to form one envelope.

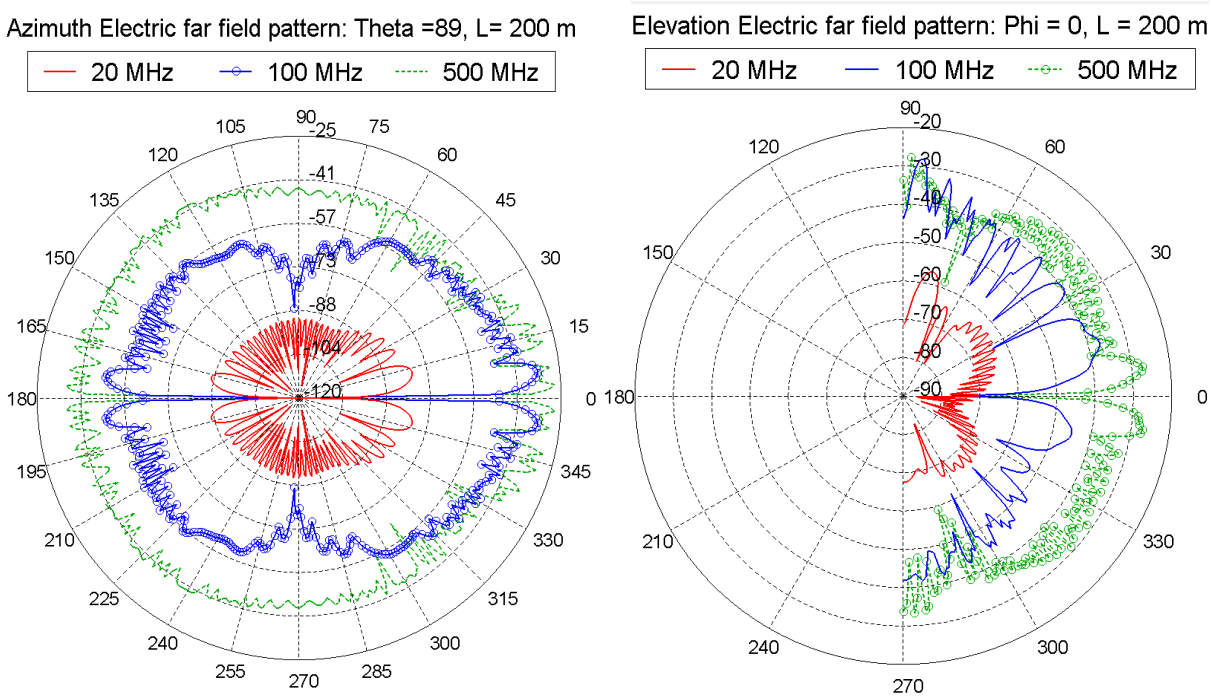

Figure 5-21: Azimuth and elevation electric far field patterns at various frequencies

This section has presented the numerical evaluation of the influence that the line parameters such as the length, impedance, topology, ground properties, and the position of the source along the line, have on the radiation patterns. Most of these factors are expected to vary throughout the length of a long line and these investigations have been performed to determine their effect on the radiation characteristics of the line. In general, it has been shown that, due to their long dimensions and depending on the source frequency, the radiation patterns from these lines exhibit end-fire pattern characteristics. The main lobes for the maximum radiation are found to be more directed towards the line as its length is increased. With a source position offset from the middle of the line, the maximum radiated field strength gets pushed in the direction away from the source end resulting in an unsymmetrical pattern. Although the far-field pattern was found to follow the general orientation of the line with bent sections, the pattern is far more complex than that of a straight line with similar dimensions due to different radiation direction from each of the bent parts.

5.5 Physical scale models

The variation of simulated radiation characteristics of power-line models when line parameters are changed was discussed in the preceding section. To verify the simulations, physical scale modelled lines for some simple configurations were constructed and their radiated fields measured in an anechoic chamber. These scale models are useful since it would be impractical to perform proper radiation pattern measurements for a real-world power line network. This is limited by the line's complex configurations and long dimensions which would traverse inaccessible areas such as farms with vegetation and fencing. Measuring of the skyward-direction vertical patterns is limited by the logistics of supporting a receiving antenna at different heights. The influence of the receiving antenna's supporting structures, such as a cherry picker if used, on the line radiation properties also needs to be accounted for in the experimental data analysis.

5.5.1 Physical scale model description for far-field pattern evaluation

Physical scale model lines on finite sized ground planes were constructed. One consideration in building such models is their size with respect to the chamber's frequency capability. An appropriate scaling factor thus must be chosen. A 1/200th scale-modelled line, shown in Figure 5-22a, was designed considering all the parameters and is henceforth referred to as PEC1 model.

The line configurations involved 3 horizontal copper wires of 1.5 m in length supported 60 mm above an aluminium ground plate by wooden structures. These wires were 5 mm apart. The adopted dimensions correspond to a full-scale system of 300 m overall length (equivalent to 3 spans of 100 m each), 1 m spacing between the wires, placed 12 m above the ground. The PEC plate, whose dimensions were 2 m x 0.6 m, was fixed to a wooden board to support the entire model, as shown in Figure 5-22a. The ends of the lines (except at one end of the middle conductor) were terminated with 500 Ω chip resistors to represent the surge impedance of the lines above the ground. A metallic strip, in form of an L-plate, was used to ground these terminations. A sub-miniature version A (SMA) connector was used at one end of the middle conductor to act as the input excitation point of the signal from the VNA. Although this makes the line to have a 50 Ω termination, a computational comparison between lines with 50 Ω and 500 Ω impedances did not show any effect on the radiated pattern shape and symmetry. This model is used to evaluate the radiation properties of the horizontal wires, and will be compared to the computational predictions, with possible effects of a finite sized PEC ground plane considered.

(a) (b)

Figure 5-22: Physical scale modelled power lines (a) on PEC and (b) on equivalent dissipative ground planes measured in an anechoic chamber

To approximate the effect of a real ground on the radiation patterns, a scale-modelled line on an absorbing material was also constructed. Due to its availability in our laboratory, a dissipative block medium, whose properties are $\varepsilon_r = 1.70$ and $\sigma = 147$ mS/m [58], was chosen to act as a finitely conducting ground plane. This medium, shown in Figure 5-22b, is made from polystyrene beads that are covered with lossy graphite phenolic. The actual dimensions of this block were 200 cm x 80 cm x 30cm. The dimensions of this block dictated the choice of the scaling factor to be used, which in this case was chosen to be $1/120^{th}$. In a similar manner to the PEC1 model, the line configuration used 3 horizontal copper wires of 2 m in length and raised 100 mm above the top surface of the block. This represented an actual line of 2 spans of 100 m each, suspended at 12 m above the ground. The terminations of each conductor are the same as those of the PEC1 model.

5.5.2 Physical scale model measurements

Due to the models being electrically large and involving finite ground planes, their simulations require substantial computing resources. The required discretization of the finite ground plane and long wires in FEKO, with the available resources, limits the higher simulation frequency range. This frequency range is further limited by the scaling factor used

together with our measuring equipment and environment. The absorption of the anechoic chamber operates best at frequencies between 2 GHz and 18 GHz.

The far-field radiation pattern measurements for the two models were performed in the chamber with a 2-port VNA as shown in Figure 5-22. The VNA was first calibrated using a short-open-load-through (SOLT) scheme whose reference plane was set at the far ends of the phase stable cables connecting the two ports. The calibration was done between the frequencies of 2 GHz and 8 GHz, which represents a scaled frequency band of 10 – 40 MHz, with 201 equally- spaced discrete points. The PEC1 model was then placed on the turn-table and fed with an input signal from port 1 of the VNA through an SMA connector attached to the middle conductor.

A ridged-horn antenna was connected to port 2 of the VNA and was used as a receiver of the radiated far fields as illustrated by Figure 5-23. This antenna, which operates between 2 – 18 GHz with an average gain of 12 dB, was placed on the far end of the chamber and raised to the same height as the scale model. Automated S_{21} measurements were then taken with the PEC1 model being rotated on the turn-table through azimuthal angles of -90^0 to 90^0. Here, the azimuthal angle of 0^0 is the angle at which the far end (the end without the source point) of the scale model points directly at the antenna.

By contrast, the equivalent earth block could not be rotated due to its weight. The block was placed on the walk-way of the chamber and the measurements were made by horizontally moving the receiving antenna on the other far end of the chamber. This limited the measurement azimuthal angles to between 0^0 and 30^0 with respect to the centre of the model.

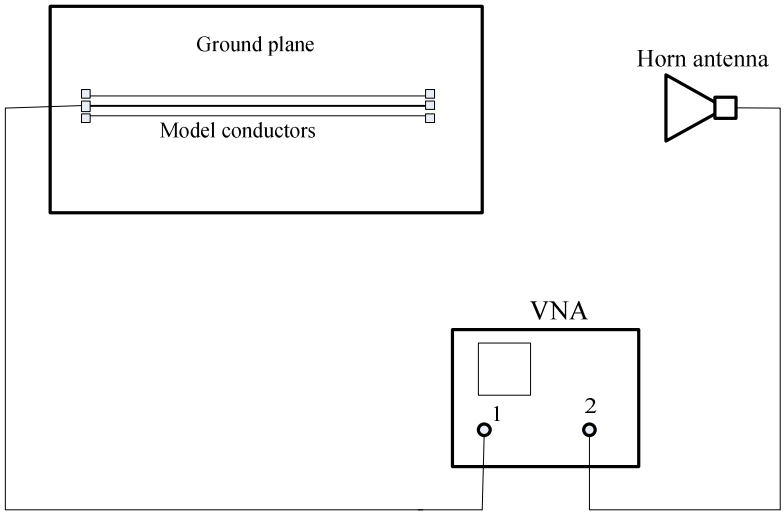

Figure 5-23: A sketch of the measurement setup for the three-phase, power-line, scale models at the anechoic chamber

5.5.3 Computational Scale Models

The physical scale models were replicated and simulated in FEKO and the simulated and measured results compared. The model setups on the computational domain were reproduced up to the calibration planes of the physical models, i.e. the input points. Wire structures, as opposed to the cylindrical volumetric structures, were used in FEKO for the radiating conductors of the model. This reduces both the computational time and memory space requirements without affecting the current approximation on the conductors. Finite ground planes in the form of a PEC and a dielectric medium to represent the corresponding physical models were used in the simulations. Discrete ports were defined with impedances of 500 Ω used for the terminations at the end of the wire structures in same way as the physical model. The excitation source at the input of each model was set to 1 V.

The model discretization was achieved by subdividing the wires into segments and the surfaces of the ground planes into triangles. The sizes of these elements depend on the wavelength in the medium surrounding the structure. The long wire lengths and the large

surfaces of the models' ground planes resulted in a great number of mesh elements at the higher frequencies. To simulate these structures on a single four-core machine with 4 GB of memory would require several hours of run time and enormous amounts of out-of-core memory to complete the computation. A High Performance Computing (HPC) platform, which is available to students and staff at Stellenbosch University, was used for these simulations. The facility has 21 nodes, each with 2 quad-core processors and 16 GB of memory. The distribution of the mesh elements was varied in order to further reduce the run time without compromising the accuracy of the computed results. This was done by defining shorter segments for the wires and larger local mesh sizes for the ground planes. Since the physical PEC ground plane used had a thickness of about 2 mm, replicating this in FEKO requires a definition of volumetric structures. A comparison of results between structures using PEC sheets and metallic cuboids did not show any significant difference. The simulations were therefore undertaken with PEC ground planes of thin rectangular plates. This eliminated the need to mesh whole volumes, which results in less memory and computation time requirements.

Far-field radiation patterns were computed for the PEC1 and block models for frequencies between 2 GHz and 4 GHz. The scaled highest frequency of 4 GHz corresponds to 20 MHz and 33.3 MHz for the PEC1 and the block models, respectively.

5.5.4 Far-field Measurement and Simulation Comparisons

The measurements obtained for both PEC1 and block models gave the azimuthal far-field radiation patterns for the models after accounting for the horn's antenna factor. The typical azimuth patterns are given in Figure 5-24 for the PEC1 model for both FEKO simulations and the measurements at a sample frequency of 17.5 MHz (scaled to 3.5 GHz). The two patterns show a deep null, as expected, along the line axis, that is, along $\phi = 0^0$. The largest radiation lobes, which lie between the line axis and the first null, have a maximum radiation level at about 10^0 for both patterns. These patterns, which are not normalized, also have successive

minor lobes whose amplitudes regularly decrease away from the main lobe and are tilted, in the considered angular plane, in the direction of the radiation from the line. This can clearly be seen in the 3-dimensional images given for both the azimuth and elevation patterns in Figure 5-25. These patterns confirm the direction of the main lobes, i.e. towards the line axis, for long wire lines, which for this case at the given frequency are 17.5λ long.

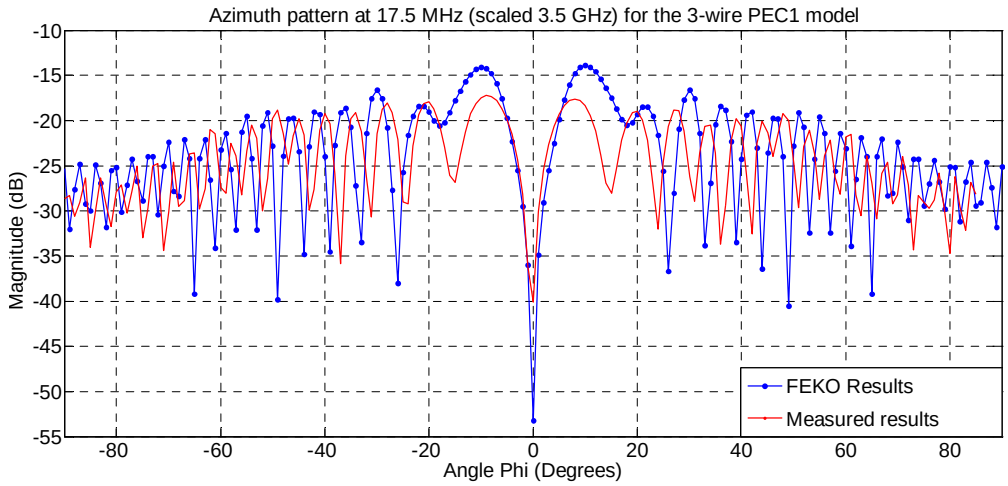

Figure 5-24: Azimuthal far-field patterns for the PEC1 model at 17.5 MHz (scaled 3.5GHz)

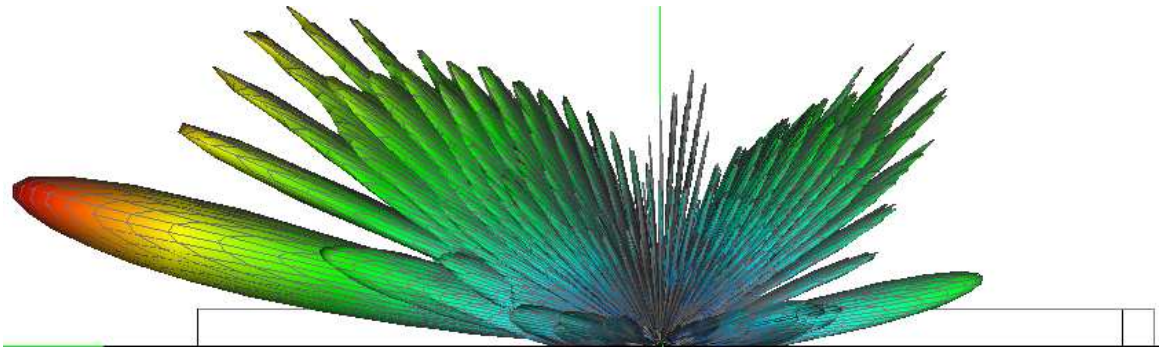

(a)

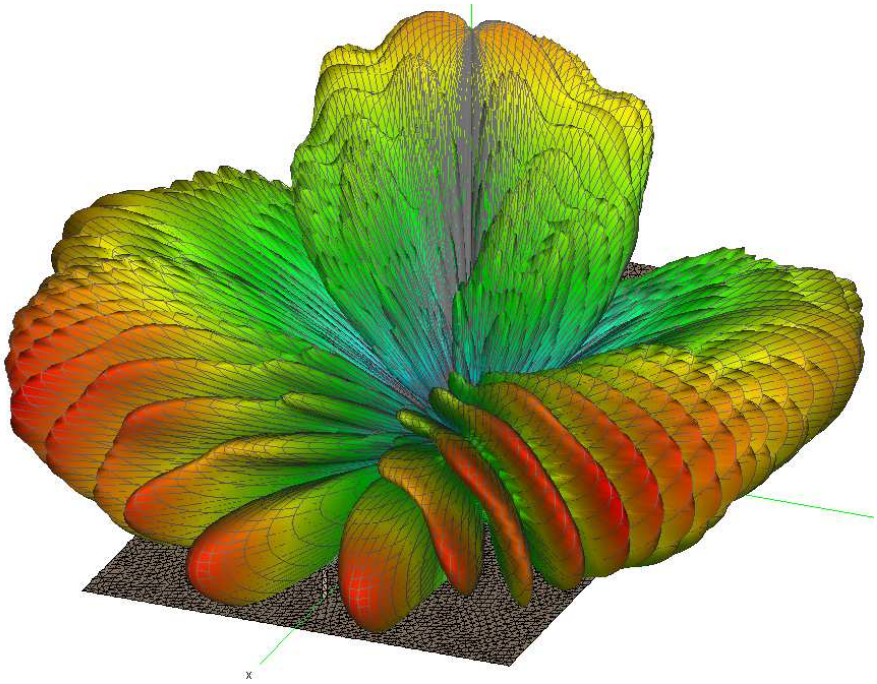

(b)

Figure 5-25: Simulated 3-D representations of (a) elevation and (b) azimuth radiation patterns for the PEC1 model at 17.5 MHz (scaled 3.5GHz)

The typical normalized azimuth far-field patterns obtained for the block model are given in Figure 5-26a and Figure 5-26b for sample frequencies of 25 MHz (scaled to 3 GHz) and 32.5 MHz (scaled to 3.9 GHz), respectively. As mentioned earlier, the measurements on this model were taken for the azimuthal angles of only between 0^0 and 30^0 with respect to the centre of the model. The simulated results were also generated at these angles where the line axis lies along the 0^0 angle. The angle of radiation of the main lobe with respect to the line axis decreases with frequency. This can be seen on Figure 5-26a and Figure 5-26b where the main beam for the 25 MHz case is directed at about 10^0 but about 8^0 for the 32.5 MHz case. Similar trends can be observed on both the measured and the simulated patterns. The differences in the patterns can be attributed both to the simulation of the model with the volumetric dielectric ground medium and the measurement complexity.

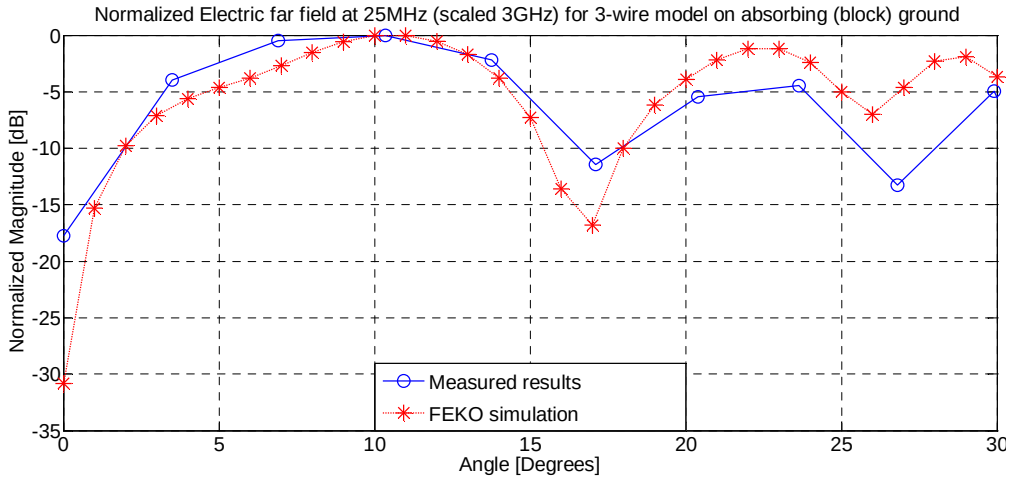

(a)

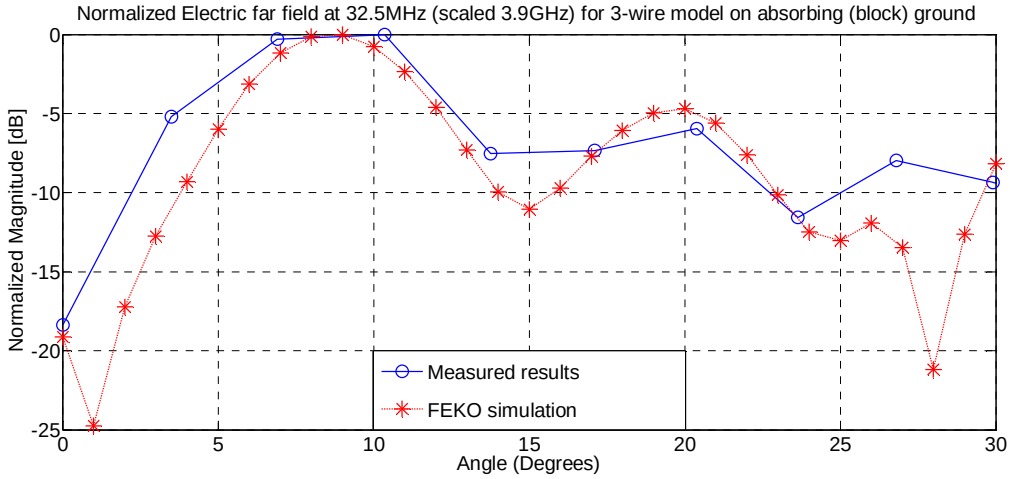

(b)

Figure 5-26: The normalized azimuth far field radiation patterns for the absorbing block model at (a) 25 MHz and (b) 32.5 MHz

5.5.5 Near-field radiation measurements and simulations

Proper far-field radiation measurements from real-world power lines are not viable. This is because the far-field observation points *r*, which depend on the line the dimensions according to the relation $r > 2D^2/\lambda$, would extend across a very wide area depending on the line length and the noise frequency of interest. Here, D is the largest dimension of the radiator and λ is the wavelength. The radiation measurements from such lines are most often undertaken in the

vicinity of the radiating conductors. It is valuable to check how the computation code presents the radiated near field at an observation point that is in the far-field region. In general, near-field computation gives an exact solution of the radiated field at a given observation point, while the far field approximates that field at a Raleigh distance greater than r from the radiator.

A comparison between the near fields and the far fields at a point in the far-field region was done through an example in the form of a single wire line, given in Figure 5-3, above a PEC ground plane. This is shown in Figure 5-27 and Figure 5-28 for the azimuthal and elevation patterns, respectively, where both the near and far fields were calculated in the spherical surface enclosing the line. From Figure 5-27, the line in the $\phi = 90^0 - 270^0$ axis with the source being in the 270^0 side. The near fields were computed at sample distances of 100 and 6000 m from the line centre. The 6 km distance is in the far-field region which, for the given line length, is beyond 3072 m from the radiator.

It can be seen from the two figures that the correspondence between the near-field and far-field computations improves, as the observation distance gets further away from the line. There is clearly a distance dependence of the near field at positions close to the line as can be seen in the near-field plots for 100 m from the radiating line. The near-field computation correctly reproduces the far-field pattern at distances that are in the far-field region. With this good correlation, the near-field computation of the code can therefore be applied to determine the radiated fields near the line, such as the measurement points at the Klerefontein site, to evaluate the lateral and longitudinal propagation characteristics.

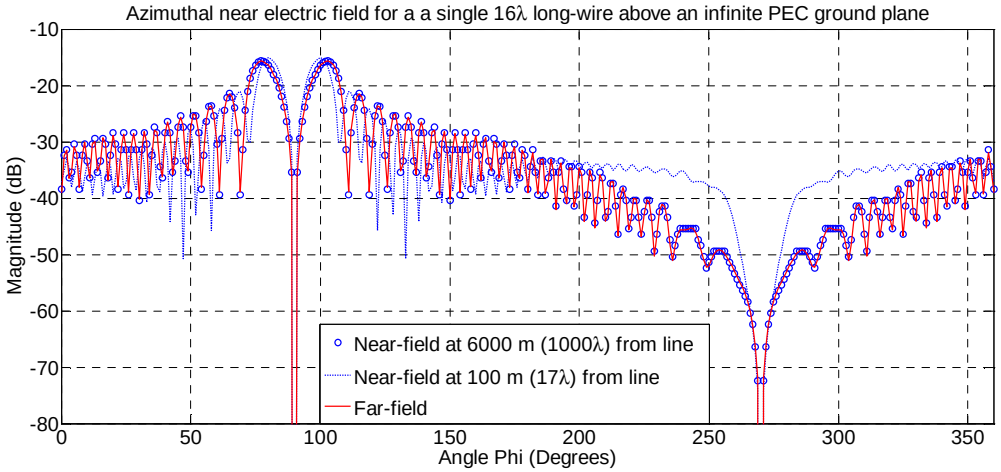

Figure 5-27: Comparison of azimuthal far- and near-fields for a single 16λ long-wire above a PEC ground plane.

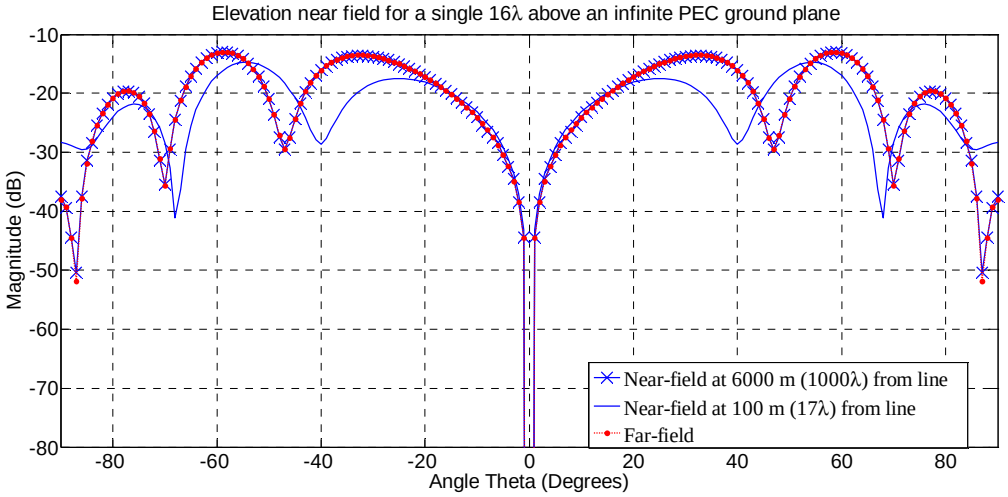

Figure 5-28: Comparison of elevation far- and near-fields for a single 16λ long-wire above a PEC ground plane.

To evaluate the lateral and longitudinal radiation characteristics of the radiated field from a power line, a 1/200th scale model with identical dimensions and terminations to the PEC1 model described above was constructed. This model, which is henceforth referred to as the PEC2 model, used a 2 m x 1.5 m aluminium ground plane. This helped to position the measurement points along and away from the line axis as illustrated in Figure 5-29. These

points were made by threading 4 mm holes on the ground plane to hold a female/female SMA adapter. The latter was fitted with a 5 mm long pin to act as a pick-up antenna element. The ends of the ground plane were in the form of L-plates to reduce the unwanted common-mode (CM) currents excited on the rear side of the plate from interfering with the measurements.

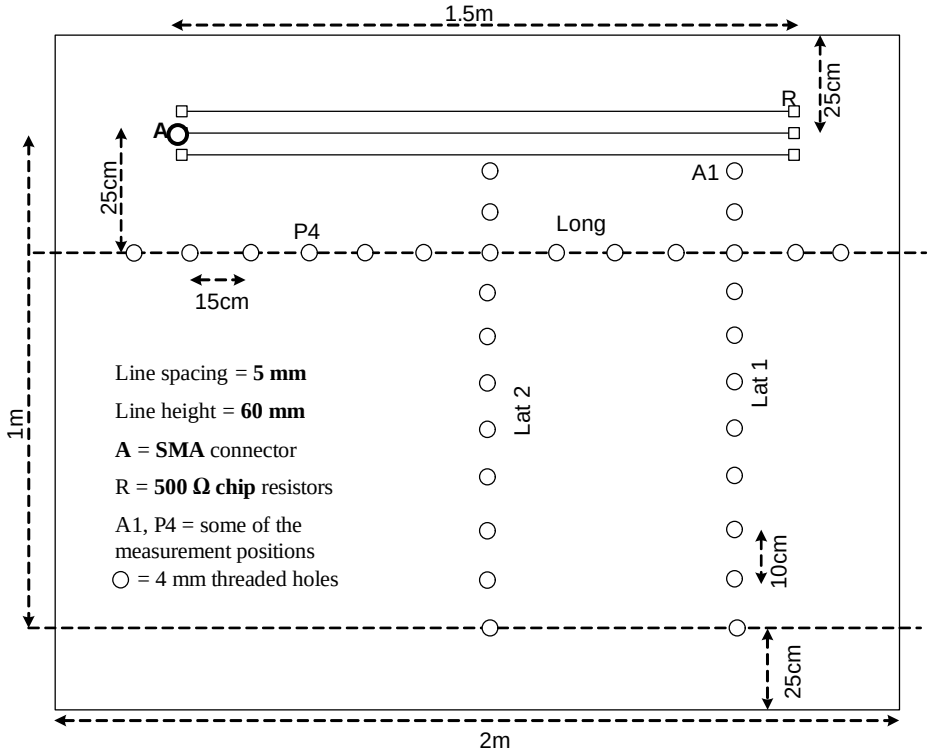

Figure 5-29: A sketch of the 1/200th scale model (PEC2 model) physical layout showing near-field measurement positions

As with the other scale models, the measurements were in the anechoic chamber, shown in Figure 5-30. Here an input signal with a power level of 10 dBm, at 8 discrete frequency points between the frequency range of 2 GHz and 4 GHz, was injected from port 1. The model's input point was through an SMA connector connected to the middle wire (point A on Figure 5-29). The near field at each of the measurement positions was measured using a SA, which was connected through a phase stable cable to the SMA adapter that was fitted with the pin probe, at each frequency point. The measured results were recorded in dBµV format.

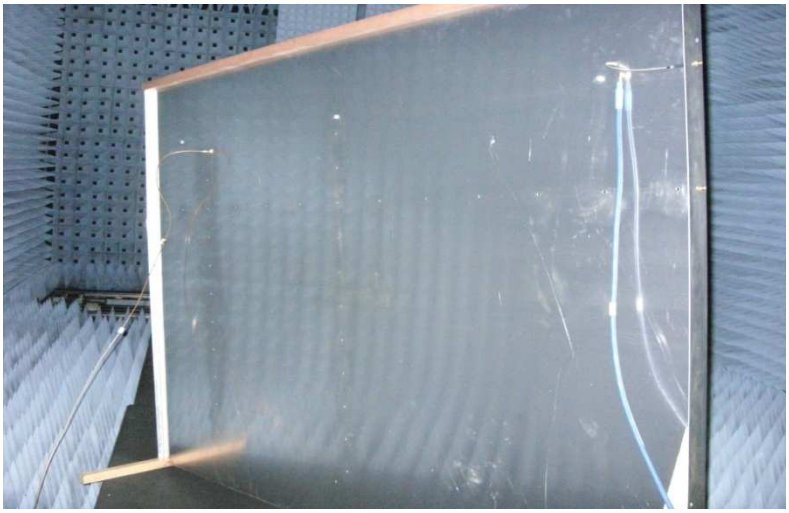

Figure 5-30: The anechoic chamber measurements of the 1/200th scale-model (PEC2 model). The line wires are behind the visible part of the plate. The phase stable input and measurement cables used are visible on right and left, respectively.

To verify the above measurements, another set of tests were performed on the same model. Here, the VNA was calibrated with a full 2-port SOLT calibration scheme at 401 discrete frequency points between 1 GHz and 3.5 GHz. Then, with the VNA set to 10 dBm input signal, the complex S-parameters were recorded at some of the measurement positions on the model using the pin probe connected to port 2 of the VNA. To compare the measured S_{21}, recorded by the VNA, with the magnitude level measured by the SA at a given probe position, the voltage level delivered by port 1 of the VNA has to be known. This is because the measured S_{21} is a ratio of signal at port 2, V2, to the injected signal at port 1, V1 i.e.

$$S_{21} = 20 * log_{10}\left({}^{V2}/_{V1}\right)dB \qquad 5\text{-}19$$

The magnitude of port 1 signal was deduced at the calibration reference plane using the SA and the required V2 (in dBμV) at the probe measurement position was obtained by adding this measured V1 (in dBμV) to the measured S_{21} (in dB).

The typical measured V2 for the longitudinal profile is given in Figure 5-31 and Figure 5-32 for two sample frequencies of 2 GHz and 3.43 GHz, respectively. Similar trends were also observed on the results from other considered frequency points.

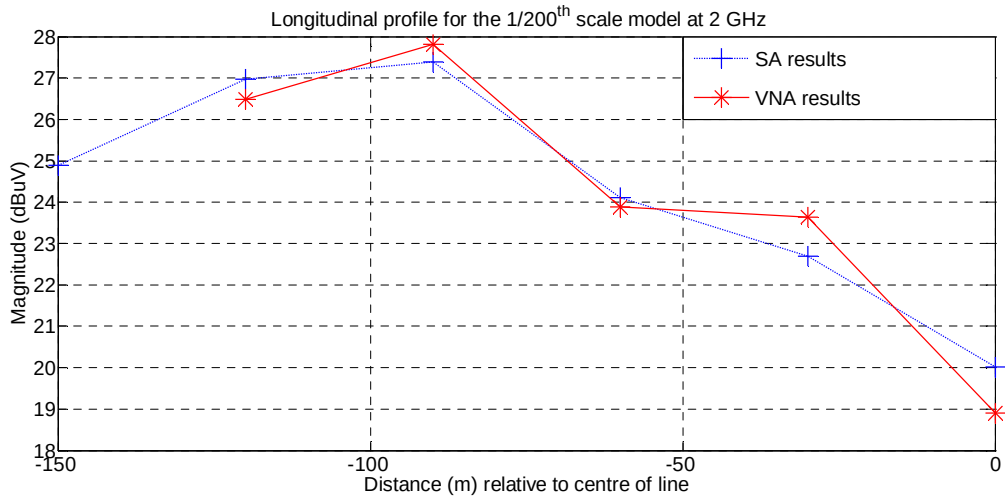

Figure 5-31: Comparison of the voltage magnitude measured with SA and VNA on the longitudinal profile of the 1/200th scale model (PEC2 model) at 2 GHz

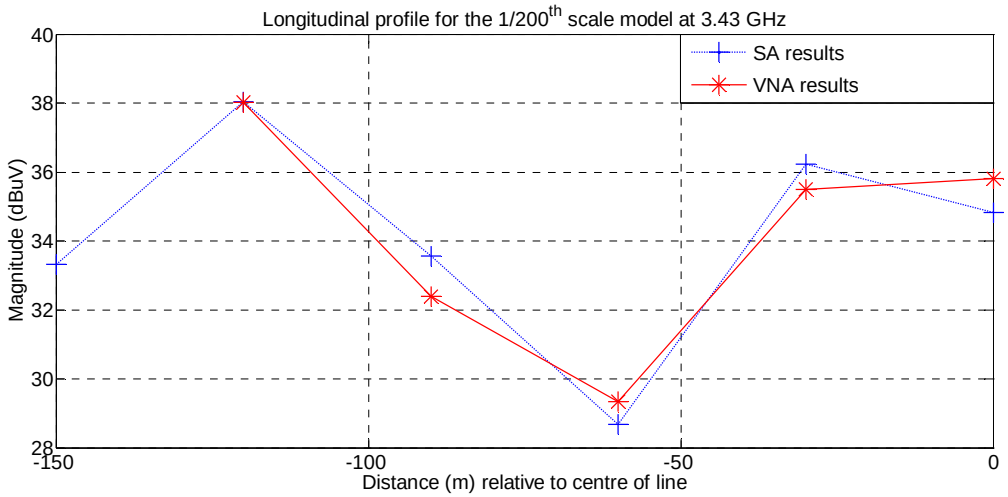

Figure 5-32: Comparison of the voltage magnitude measured with SA and VNA on the longitudinal profile of the 1/200th scale model (PEC2 model) at 3.43 GHz

These correlations show the repeatability in performing such measurements, which are taken in the vicinity of the radiator. For a case such as this model, the results from any of the two setups can be used to analyse both the longitudinal and lateral radiation characteristics of the radiated field. At the same time, the measurements from any of these setups can be used to verify the computational code of the model. It was important to undertake this exercise as it was not certain whether or not CM currents, with the truncated ground plane, would influence the results.

Verification of the computational code was done through the comparison of the S_{21} results from both the VNA and FEKO simulations. To do this, the input voltage for both cases need be known. The excitation for the simulations was defined as 1 V, which is equivalent to 120 dBµV. To compare the two S_{21}, the simulated S_{21} was compensated for by adding it with the difference between the FEKO and the VNA inputs. The typical resultant S_{21}, with V2 taken at point A1 of Figure 5-29, is given in Figure 5-33. The variation of the S_{21} from both cases follows a similar trend. Similar correlation was also obtained for other considered measurement points.

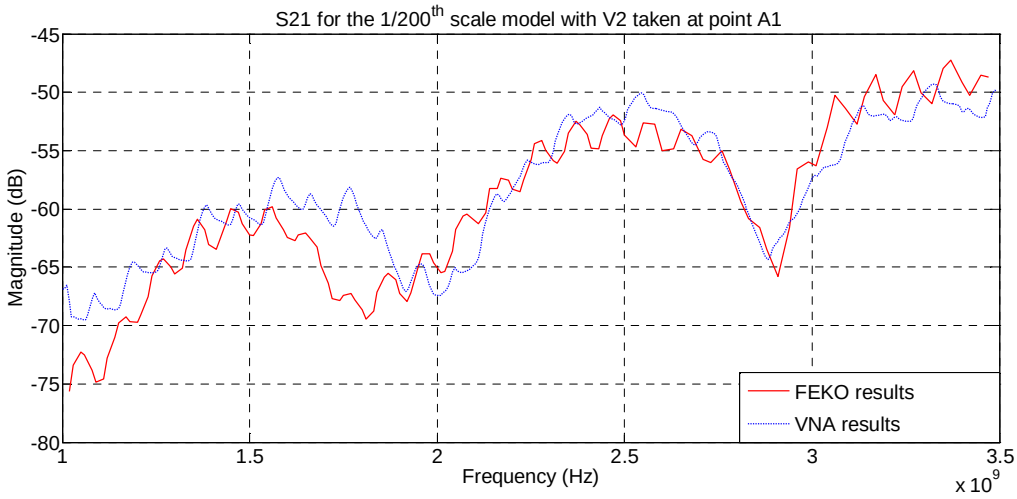

Figure 5-33: Comparison of the S_{21} from the simulation and measurements at point A1of the PEC2 model

With this verification of the computational code, the analysis of the line propagation characteristics can be undertaken with the simulation results. The lateral profiles computed for the PEC2 model along Lat1 and Lat2 of Figure 5-29 are given in Figure 5-34 and Figure 5-35, respectively, for a frequency of 2 GHz. The measurement positions along Lat1, such as point A1, are 30 m (in real scale) away from the near end of the line. Those of Lat2 are located at the centre of the line axis. The longitudinal profile, along the measurement positions given as Long, for the same model at 2 GHz is given in Figure 5-36. These results were obtained by computing the near field at the corresponding points at a height of 1 m (scaled to 5 mm) above the ground. This enables the evaluation of the variation of the radiated field as a function of distance from the simulated line structure. Similar results computed at 2.5 GHz are provided in Figure C-1 to Figure C-3, respectively, in appendix C. From Figure 5-34, the rapid reduction of the field levels away from the line can be observed. The significant peaks emanating from the radiated field and encountered along the computation path away from the line are also visible. Up to 101 points, at each frequency, along the considered lateral path were used to compute the electric field. The number of these peaks increases with frequency as observed in Figure C-1.

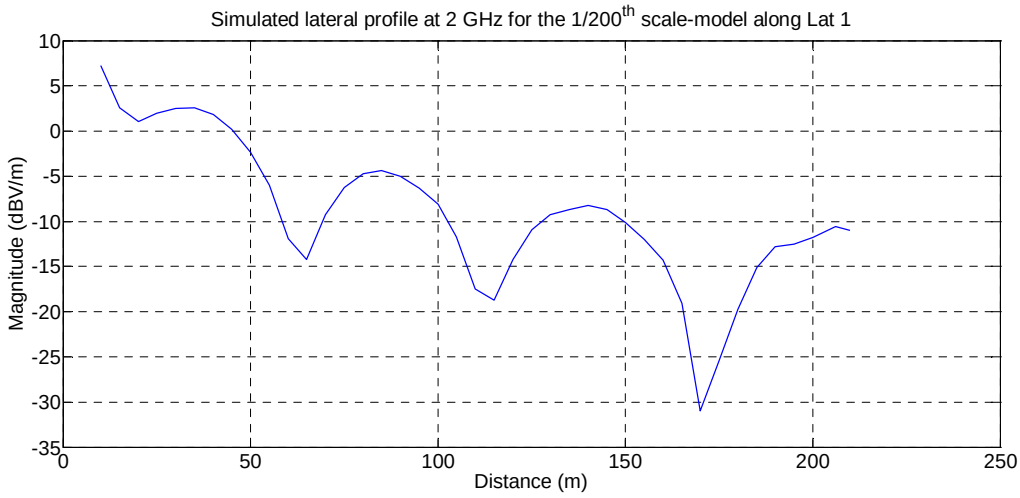

Figure 5-34: The simulated near field lateral profile along Lat1 of PEC2 model at 2 GHz

The lateral profile given by Figure 5-35 illustrates a continuous decay of the field strength with no peaks being encountered. These results were obtained from the computation of the fields along a perpendicular path to the line, which is at the centre of the line. This is in line with the results obtained in the simulation of lines of different configurations given in section 5.4, where lobes of the radiated azimuthal far field are directed at an angle towards the line and not along its broadside direction.

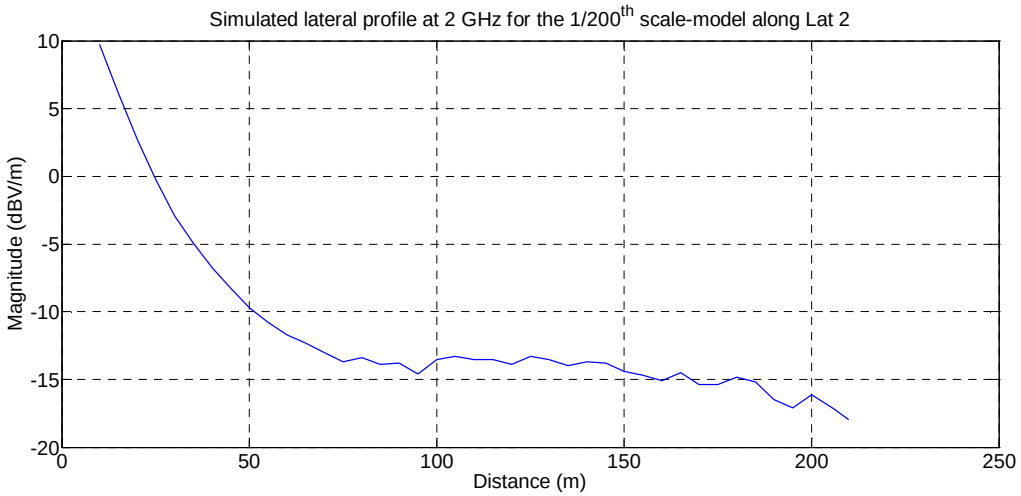

Figure 5-35: The simulated near field lateral profile along Lat2 of PEC2 model at 2 GHz

The longitudinal profile of Figure 5-36 was computed along the positions given as Long, which are parallel to the line axis and are located at 50 m (in the real scale) away from the line. The line extends from -150 to +150 m with the source point being at the +150 m side of Figure 5-36. The radiation along the line is, on average, fairly constant demonstrating that the injected signal will not be radiated in a point source form but along the line length i.e. a line source.

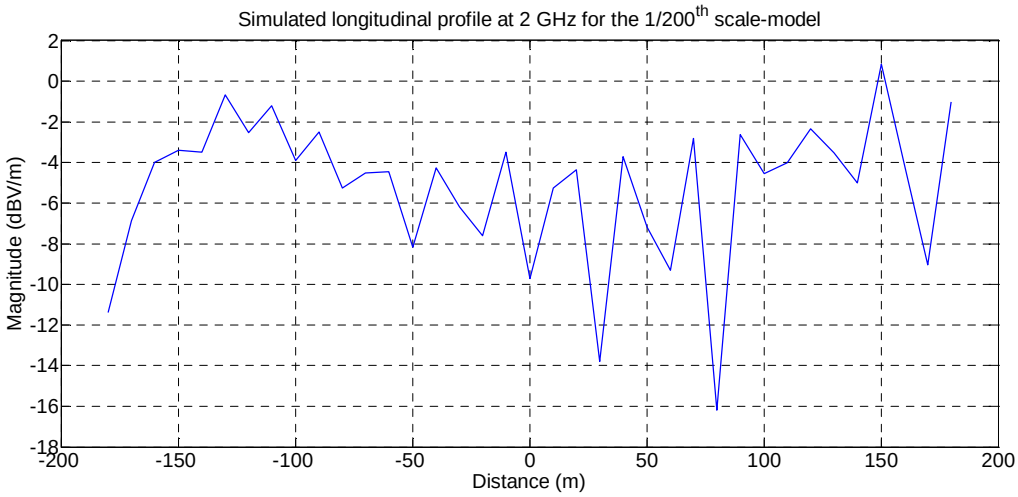

Figure 5-36: The simulated near field longitudinal profile along Long of PEC2 model at 2 GHz

5.6 Pulse generator measurements

To further verify the above simulated and scale model power-line propagation characteristics, pulse generator measurements were undertaken on a wooden-pole section of the main power line that runs from Carnarvon sub-station to the core-site. This is the line, as discussed in section 6.5, which has been designed to supply energy to the MeerKAT facilities. At the time of measurements, the line was still under construction and a 9-span straight section that was open on both ends was available for our use. The measurements taken here were to enable us study the propagation characteristics of a radiated pulse injected onto a line.

Figure 5-37 shows a pulse generator being connected to one end of an open section of an un-energized line. This open line section had 9 spans of approximately 100 m long each. On one end of the line, the 3 line conductors were first grounded, and then the generator, which was powered by a battery-driven inverter, was capacitively coupled to the centre conductor. The generator was set to output an 11.7 MHz repetitive pulse. The radiated pulse frequency spectrum was then measured along the points P1 – P9 and P6 – L9, as given in Figure 5-38a, using a dipole antenna (see Figure 5-38b).

Figure 5-37: Pulse generator being coupled to one end of the open line section

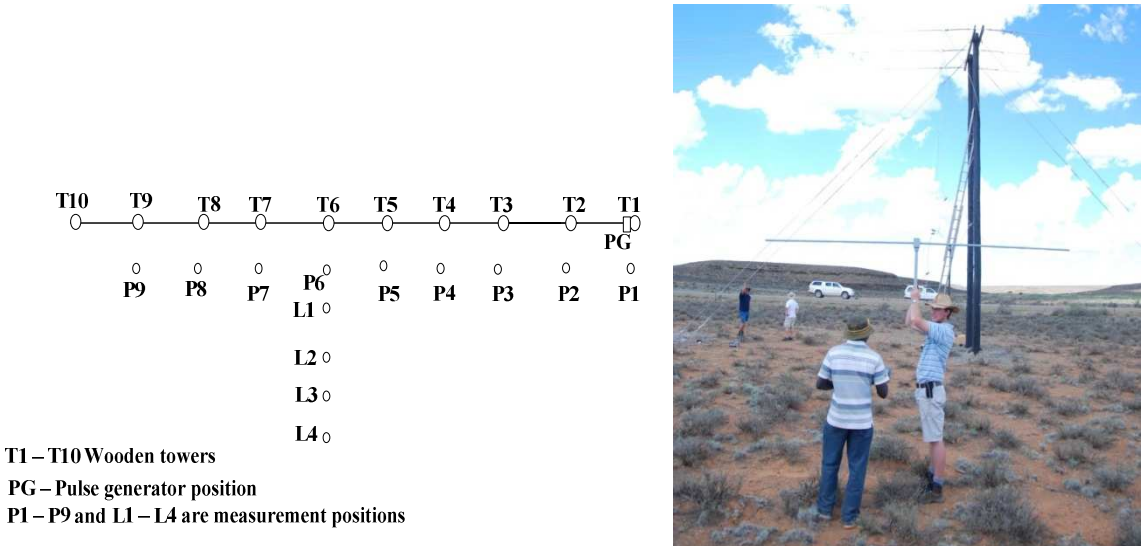

(a) (b)

Figure 5-38: (a) sketch of the measurement site and (b) measurements taken with dipole antenna

5.7 Pulse generator lateral and longitudinal profiles

The maximum magnitude of the pulse frequency spectra were measured, using a SA and a broadband dipole antenna, along the points given in Figure 5-38a where the points P1 – P9 are parallel to the line axis and are about 10 m away from the line. The path given by the points P6 – L9 is perpendicular to the line at tower #6, T6, and these points are 20 m apart

with L4 being 90 m away from T6. From these spectra, the lateral and longitudinal profiles are extracted at 11.7 MHz, the fundamental frequency that was coupled to the line, and 23.4MHz, its second harmonic. As can be seen in Figure 5-39, the lateral profile shows that the signal strengths of the pulses decay with distance away from the line but remains fairly constant along the line length as seen on the longitudinal profile. These compare well with the results obtained in Figure 5-34 – Figure 5-36 where the computation was done at 2 GHz (which is equivalent to 10 MHz in real scale).

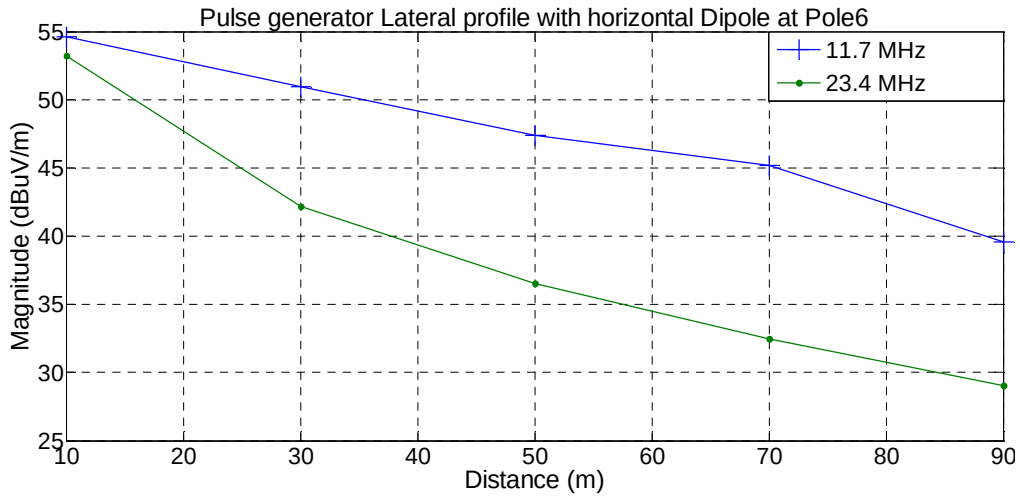

(a)

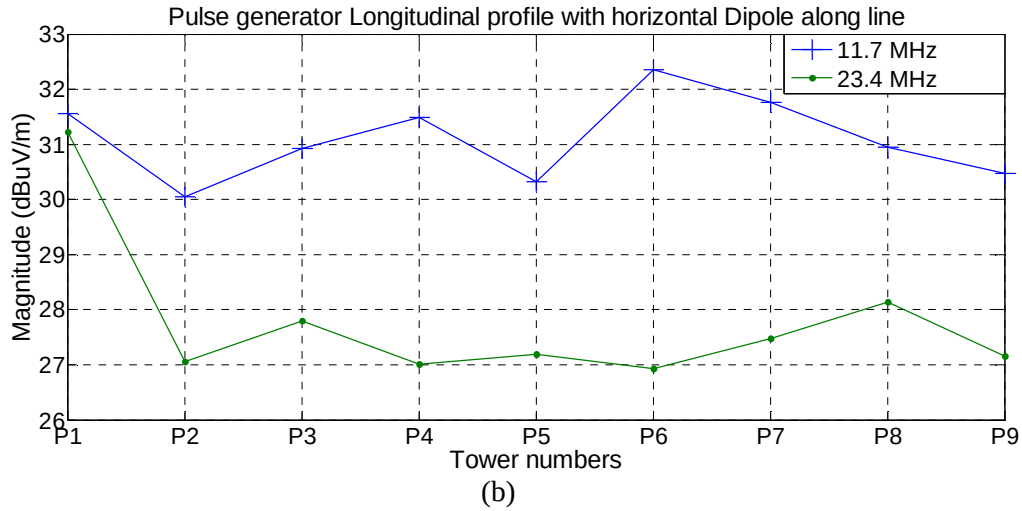

(b)

Figure 5-39: (a) Lateral and (b) longitudinal profiles for the pulses capacitively coupled to the line

In the longitudinal profile, the radiated emissions were measured at intervals of about 100 m. Close-enough measurement intervals would pick up points of maximum and minimum emissions showing the variation that would be encountered for a line such as the one used here. Since the measurement positions are within the near field region of the radiator, picking points with maximum radiation to estimate the line radiation pattern is impossible. The field strengths in this region decay rapidly with distance in the directions perpendicular to the line.

5.8 Conclusions

The radiation characteristics of the signals injected on power lines has been evaluated. This was done through both computational and physical scale modelling. The influence of factors such as the line length, geometrical configuration, frequency, impedance, and source position, on the power line far-field radiation patterns was analysed through FEKO simulations. The physical scale models of simple power line structures were constructed and their radiated field patterns measured in the anechoic chamber. These measured field patterns were compared with the simulation from the corresponding line configurations. The results show that identifiable characteristics can be attributed to power line radiation. The lobal behaviour associated with end-fire antennas is seen. The main lobes are directed towards the line axis at an angle that partly depends on the simulation frequency. Several minor lobes, which occur due to the line being electrically long and also the effect of the line radiation above a ground plane, are observed.

The variation of the radiated field as a function of the distance from the line in both longitudinal and lateral profiles was also investigated. This was done through simulations and measurements on a physical scale model and on a 9-span power line on which, in the latter case, a repetitive pulse was injected onto the un-energized line and the radiated field measured at various positions. The power line propagation properties obtained in this chapter together with the sparking noise characteristics given in the previous chapters can then the used during the location and mitigation processes of sparking noise that may occur on a given power line.

Chapter 6

Sparking Noise Location and Mitigation Measures

6.1 Introduction

Interference from power line sparking noise can adversely affect the operations of various nearby communication facilities. This effect can be minimized or eliminated by undertaking appropriate mitigation measures. Since sparking noise sources occur at hardware such as loosely bonded parts, the resultant interference can be eliminated by tightening the loose hardware or by adequately spacing the unbonded ones. If interference is suspected to be affecting the functions of the communication systems in a certain site it is necessary to determine the impact that it is causing to those facilities. Using suitable instrumentation, the background noise in that site should be measured to confirm the presence of sparking noise. The measured temporal and spectral characteristics must conform to the properties of the noise as had been discussed in the previous chapters. When the presence of this noise has been confirmed, the general direction of its source(s), which normally occur on power line poles, is then located and the specific hardware components that contain the noise sources are identified. Once found, appropriate corrective measures can then be applied to repair the noisy hardware.

6.2 Required instrumentation

To localize the sparking noise sources on a power line network, it is important to first measure the noise time and spectral characteristics to identify and distinguish them from the noise from other sources. This is accomplished through the use of appropriate equipment and being able to interpret these instruments' readings. These instruments should have sufficient dynamic range and sensitivity to detect present interfering signals. Since sparking noise is broadband, a wide bandwidth oscilloscope is necessary for measuring the time domain characteristics. Either an EMI receiver or a SA operating over a wide range of frequencies is adequate for measuring the frequency domain properties of the noise. As it was found in Chapter 4 that the sparking noise increases faster with receiver's RBW as compared to the thermal background noise, this can be exploited in isolating sparking phenomenon. The receiver should have a relatively wide IF bandwidth, preferably at least 1 MHz, to ensure that sparking discharges are not masked by the background noise and thus enabling better detection. A low noise wideband preamplifier will be useful in improving the sensitivity and dynamic range of the measuring receiver. Both the oscilloscope and the receiver should preferably be battery operated. This would make them easily portable and thus suitable for use in sections of the power line network that are inaccessible to vehicles such as on farms.

A wideband high-gain antenna(s), preferably a directional one, such as an LPDA antenna is needed for use with the above instruments. To trace a general location of a noise source along the line, a vehicle, preferably a four-wheel-drive, would be useful. Either this patrol vehicle should be radio-noise-quiet or the instruments need be shielded to reduce the impulses from the vehicle's ignition system from interfering with the noise measurements. It is, however, more convenient to have the vehicle's ignition system switched off while taking the measurements. The antenna can be mounted on the rooftop of the vehicle or used in a hand-held position.

6.3 Location for sparking noise on power lines

Before locating a sparking source or its direction on the power lines, it is necessary to note that this source injects noise current (conductively and/or reactively) onto the line conductors making these conductors, and the hardware associated to that source, act as antennas. The noise radiation mainly originates from these 'antennas' rather than from the sparking source itself [11], [30]. The noise is propagated along the electrically long line conductors and radiated in the process. The radiated noise covers a wide frequency range from the audio and ultrasonic band through to the RF band which is from below 1.0 kHz up to about 1 GHz [12], [59]. The low frequency components of the noise will propagate along the conductors for fairly longer distances away from the source. The higher frequency components get attenuated faster as they propagate along the line.

The initial step in locating a sparking source on a line is by first identifying its presence. This is done by visiting the site where it has been reported and observing the signature of the noise present at that site. With an antenna (preferably a directional antenna) connected to either an oscilloscope or a SA, the temporal characteristics of the noise are observed. This should indicate if a sparking interference is present. Due to its higher sensitivity, the use of a SA (or an EMI/radio receiver if available) is preferred. Here the SA is first set to detect the maximum peak of the received frequency spectrum, with at least 1 MHz of RBW. This is to examine the highest frequency range of the noise that can be detected above the system's noise floor at that site. It would be important to add an LNA between the antenna and the SA to improve the measurement sensitivity. The polarization of the antenna can be adjusted to achieve a maximum peak reading. If a directional antenna is used then it would be possible to determine the approximate direction from where the noise is strongest. An omni-directional or rod antenna would require moving from the initial test point to determine the direction of strong noise level. Since the higher frequency components of any noise or signal basically travel in a straight line, the detected noise will be mainly due to the radiation from the hardware associated to the source and the line conductors, which are in line-of-sight with the

measurement antenna. The SA can then be set to zero span (single frequency) mode centred at the highest detectable frequency component of the noise, on an unused frequency band, and noting the maximum amplitude at that checkpoint. Once the time domain patterns confirm the presence of the noise in the site then the next action is to trace the general location of its source.

In some cases, the affected site has more sensitive receiving systems than the afore-mentioned basic measuring system. This could be, for example, an SKA facility. Is such a case, the test equipment may not be able to detect the presence of the noise at the reported site. Swarup *et al* [60], [61] used the Giant Metrewave Radio Telescope (GMRT) antennas to measure RFI from gap discharges emanating from 11 kV power lines located near the telescope's antennas. A SA was connected to some of the GMRT antennas whose primary feeds were pointed towards the horizon in specific directions. The measurements were taken at specific frequencies with the SA set to zero span mode. With this method, the general direction of a strong noise level can be determined and the basic test equipment can then be used to locate the source.

To locate the noise source point on the line, one would then drive along the sections of the line in the direction showing strong noise strength. A map for the power line network in that vicinity, showing the pole numbers and identifying those, which are accessible by vehicle, and those which are not, would be useful. The power lines for the MeerKAT (described in section 6.5) and possibly SKA are routed along the road and therefore the survey for most of the poles will be accessible by a vehicle. If one then drives along the line, while stopping to take the readings near various poles, it can be determined whether the survey is done towards or away from the source. The noise amplitude level at that frequency point increases as one gets closer to the source but will be undetectable after a few spans if one is scanning in the direction away from the source. Not only is the noise amplitude level increasing as one approach the source but also the frequency at which it can be detected increases. At this point, the sensitivity of the SA can be reduced by disconnecting the LNA. This will reduce the

received noise level and the highest detectable frequency components to prevent the equipment from saturating. The survey can then be continued, while successively raising the centre frequency, until a point is reached when the highest detectable frequency component start to decrease. This would indicate that the pole containing the source has been passed and one has to travel back to scan at the nearby pole where the highest level was achieved. The exact location of the source pole can then be refined by doing the survey on foot while using a directional antenna to pinpoint the direction of highest noise level reading. The procedures and the basic instrumentation used in this research can be used for source location up to this point. It should be noted that the guidelines given here are part of already well-established techniques suggested in [30,59,62,63,64]. The general basic steps for location of this noise are illustrated in a flow diagram given in Figure 6-1.

Once the faulty pole has been located, the next step is to pinpoint the sparking hardware in that pole. This should be done by or with the help of power utility personnel. Since a power pole typically contains numerous hardware parts that can generate sparking noise, identifying the specific faulty hardware components can be tedious. A noise sniffer device has been used in [30] and [59] to pinpoint and identify the sparking hardware on a power pole. This noise sniffing device is mounted at the far end of a distribution-line rated hot stick and it contains both RF and ultrasonic detectors. It may be used from the ground to scan around the hardware on the pole to obtain the location with the strongest signal. One can, preferably, also operate it with the help of a bucket truck to locate the source components. The RF probe, with the ultrasonic sensor in inactive mode, is first used to scan the structure suspected of having the source. The noise amplitude increases when the RF probe gets closer to the source. To reduce the area of searching for the source hardware, the sensitivity of the probe can be reduced. This reduction can be done until the source is found.

If the source generates acoustic energy, the source point can also be located with the ultrasonic detector. Ultrasonic noise from a source that is contained within insulated objects or hidden inside metallic joints is difficult to be detected. An ultrasonic device utilizing a

parabolic dish does not require an attachment to a hot stick but it has to be used where there is a direct line-of-sight path between the sparking source and the dish. The source also has to be radiating strong acoustic energy [30] for this method to be effective. It is has been reported in [60] that defective connections and insulators on power line poles were regularly located using an ultrasonic device which consisted of a small dish and an ultrasonic detector.

6.4 Correction and prevention measures of sparking noise

Since sparking noise mainly originates from gaps formed by closely spaced conducting surfaces on a line structure, it can be reduced and/or eliminated by repairing these gaps. This involves tightening the loose hardware and bonding together closely spaced conducting objects to ensure a good electrical contact between these metal-to-metal surfaces. This will eliminate the potential difference formed between the gap surfaces. Insulated staples should be used instead of uninsulated ones to fasten the ground wires on wooden poles to avoid a sparking source from occurring between the wire and the staple when the latter becomes loose [30].

Maintaining adequate spacing between unbonded metallic structures is also useful. Keeping a spacing of at least 38 mm between unbonded metallic hardware would ensure elimination of noise sources on distribution lines with a capacity of up to 22 kV [30]. It is also reported is [65] that a spacing of at least 51 mm for a supply of 7.2 kV or a minimum of 204 mm for a 14.4 kV voltage supply should be maintained between the grounded and ungrounded metallic hardware parts and also between all ungrounded pole assemblies on a power pole. If line hardware is found to have deteriorated due to age or damage e.g. aged or rotten wood poles, damaged insulators or lightning arrestors etc. they need to be replaced. If bell insulators are in use in the line and are found to be the noise source the insulators in the pole where the source is located need to be replaced with polymer type of insulators [30]. Noisy pin-type insulators need be replaced with post-type insulators.

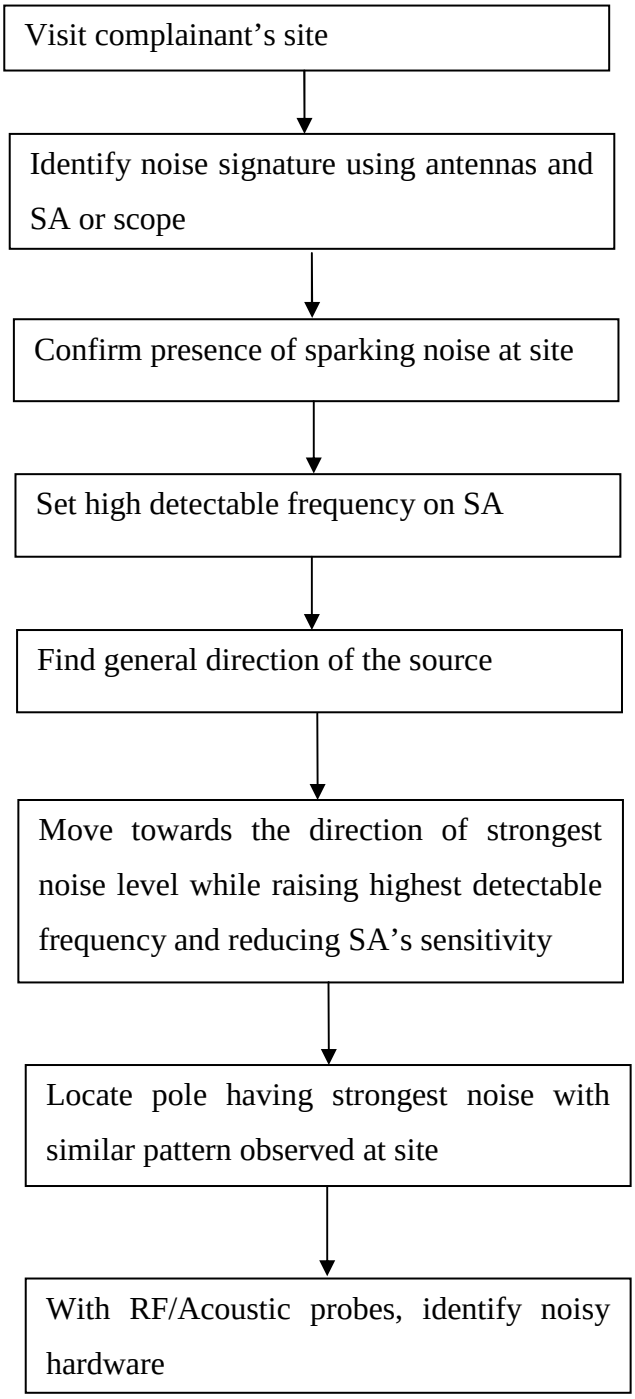

Figure 6-1: A flow diagram illustrating basic steps for locating and pinpointing of sparking noise on a power line

6.5 Power line design philosophy for mitigating sparking noise

The occurrence of EMI due to sparking gaps can be controlled and/or avoided largely through proper design policy of newly constructed power lines. This is done by ensuring the hardware is properly bonded together and also using specialized hardware that results in minimal EMI. In designing the MeerKAT 22/33 kV distribution power line at the SKA site, various design considerations and guidelines were applied to minimize the occurrence of this noise on that line. The line itself divided into an approximately 71 km overhead line suspended on wooden pole structures from the Carnarvon substation, an approximately 25 km overheard line suspended on steel monopole structures from there to a core site substation, and about 5 km underground cable from the substation to the MeerKAT antennas [66], [67]. Figure 6-2 gives the picture of part of the wooden pole section of this line.

Figure 6-2: A picture showing part of the wooden pole section of the line

To reduce sparking noise on the line the following are some of the hardware and design practices that have been utilized [66], [67]. For the wooden pole section of the line, silicon composite long rods have been used for the strain/tension insulators. Silicon composite post-type insulators with metal top have been used for the intermediate/suspension insulators, as shown in Figure 6-3. For the steel structured section, silicon rubber composite long rods have been used for tension insulators while silicon rubber composite post-type insulators are used for the line post insulators. These insulators are rated at 33 kV although the line will initially be energized at 22 kV. These would provide adequate separation between the pole and the line, due to their long current leakage path, to prevent the noise sources associated with the insulator support hardware from occurring. To reduce vibration of the line conductors, due to causes such as wind, and thus eliminate gaps from forming, vibration dampers have been installed at the end of the line conductors in each line span. Steel-frame cross-arms have been used on all intermediate and strain pole structures. This eases proper bonding of other hardware like the insulators and also provides a central point for connecting the ground wires for the wooden pole structures. All pole hardware such as bolts, nuts and washers have been tightly bonded together. To ensure a tight contact between the tie wires and the line conductors, pre-formed bare tie wires have been used to attach the bare conductors to the insulators.

Figure 6-3: Post-type (left) and long rods (right) silicon composite insulators used for the suspension and strain structures, respectively, on the wooden pole section

At the same time, the line has been designed such that there is no direct line-of-sight between the nearest MeerKAT antennas and the wooden section of the line. This has been achieved by taking advantage of the mountainous terrain of the area to shield the antenna site from possible radiation from this section of the line. In addition, there is about 20 km of separation distance between this line section and the nearest antennas. To ensure that noise sources are avoided on this line, regular maintenance has to be undertaken and proper correction measures for mitigation purposes. The entire line has also been constructed along the road. This would be invaluable for rapid location of suspected sparking noise sources on the line as it will be accessible for driving along by a vehicle.

6.6 Conclusions

Power line sparking noise can interfere with the operations of nearby communication instruments and it is therefore necessary to institute mitigation measures to reduce and/or eliminate it. Proper identification and distinction of this noise from other type of noise present in the environment is necessary. Also it is required to know the pole or hardware that contains the RFI source. This chapter discussed some of the basic steps of locating and pinpointing the interference sources, occurring on power lines, together with the basic instrumentation required to undertake these procedures. Design precautionary measures that have been taken to reduce the possibility of sparking noise sources from occurring on the newly constructed power line to supply the MeerKAT facility have also been described.

Chapter 7

Conclusions and Recommendations

EMI from overhead power lines can adversely limit the operations of various communication systems located near these lines. This power line generated noise can be in the form of either corona or sparking discharge phenomena. To reduce the impact to the victim facilities, it is necessary to mitigate these kinds of sources. An understanding of the characteristics of the generated EMI is required. This would be invaluable in locating their sources, identifying the relevant hardware on a power line, and in the creating of effective mitigation measures. This dissertation investigated the primary properties of power line electromagnetic noise with a specific emphasis on the sparking-related discharges. The emphasis was because corona noise, as discussed in Chapter 2, is not a major interference source on a distribution power line, such as that supplying the MeerKAT systems, due to the line's low voltage gradient. In addition, the corona noise rapidly decays with frequency and would not affect performance of communication systems operating in the frequency range at which the SKA and MeerKAT are planned to operate. The sparking noise, on the other hand, radiates energy across a broad frequency spectrum and mainly occurs on gaps formed by distribution power line hardware.

The generation mechanisms behind both corona and sparking breakdown discharges were outlined in Chapter 2. The sparking discharges are a function of potential differences across gaps formed by power line hardware, while corona discharges depend on the strength of the electric field in the air surrounding a high voltage conductor. When the potential difference across the gap exceeds the breakdown threshold, a spark in the form of a current pulse is generated. This pulse has very short rise time and duration, which produces very wideband interference. The theoretical temporal and spectral properties of the two discharges were

described with their comparisons discussed. Various possible sources of sparking noise were also given, which broadly include loose hardware, unbonded parts, insufficient spacing between some hardware parts, and corroded joints of some line fittings.

This research investigated the frequency and time domain characteristics of sparking noise through measurements that were undertaken in three environments: a high-voltage laboratory, a 40 m three-wire test-line, and an approximately 1.5 km, three-phase, test-line. An artificial spark-gap device that was mounted on energized line conductors was used as a noise generator. The generated time domain pulse properties such as the pulse rise times and repetition rates were measured. In addition, the resultant frequency spectrum was measured using a SA. The influences of the variations of the SA's RBW, gap length, supply voltage levels, and the measurement environment on the noise frequency spectrum were evaluated. Based on numerous measurements, the sparking noise frequency spectrum was found to exhibit a much wider bandwidth than those obtained in the literature. Energy content extending up to 3.6 GHz, the frequency limit of the SA used, was detected and is expected to extend further beyond 4 GHz with more sensitive systems used. The shape of the spectrum was noted to remain fairly constant across the considered frequency range. The behaviour of this noise at higher frequencies still needs to be investigated. With the broadband nature of this noise, the radiated noise was found to increase more rapidly than would be expected with thermal noise. The noise strength increases by approximately 20 dB with each decade increase in RBW.

The propagation characteristics of sparking on the power lines were also investigated by measuring the longitudinal, lateral, and height profiles. This evaluated the attenuation of the noise as the measurement position was moved away from the source, away from the line, or by varying the height of the measuring antenna. To examine the effectiveness of the line acting as an antenna to radiate the RF spectrum, both computation and physical scale modelling was undertaken. Various power line configurations were extensively simulated using FEKO, where the influence of such factors as the frequencies of the source, line impedances, line topology, ground properties, position of the source along the line *etc*. on the

line radiation patterns were investigated. The field patterns measured for the constructed physical scale model structures for simple line geometries compared well, in the regions of measurement, with the simulations for the corresponding line configurations.

The knowledge of sparking noise radiation properties is helpful while locating its sources in order to eliminate them. Some of the basic steps of locating and pinpointing these sources, together with the basic instrumentation required to for these procedures, were described. Since sparking noise is mainly caused by defects on power line hardware, it can almost always be corrected through proper and regular maintenance practices. Just as for other types of noise sources, MeerKAT and/or SKA operation teams would need to be constantly aware of the possibility of spark-gap sources occurring on the lines. These could be due to wind loosening some hardware, aging of wooden poles, non-maintenance of the line *etc*. They therefore need to institute regular noise surveys to locate and correct noise sources so that the integrity of the telescope's observational data measurements is not compromised.

Appendix A

Spark-gap frequency spectrum versus resolution bandwidth

Some typical variation of sparking noise frequency spectra for a 2 mm gap-length taken with RBWs of 300 kHz and 1 MHz are shown in Figure A-1 and Figure A-2, respectively. These measurements were carried out on the short test line site. Similar results were also obtained in the HV-Lab measurements.

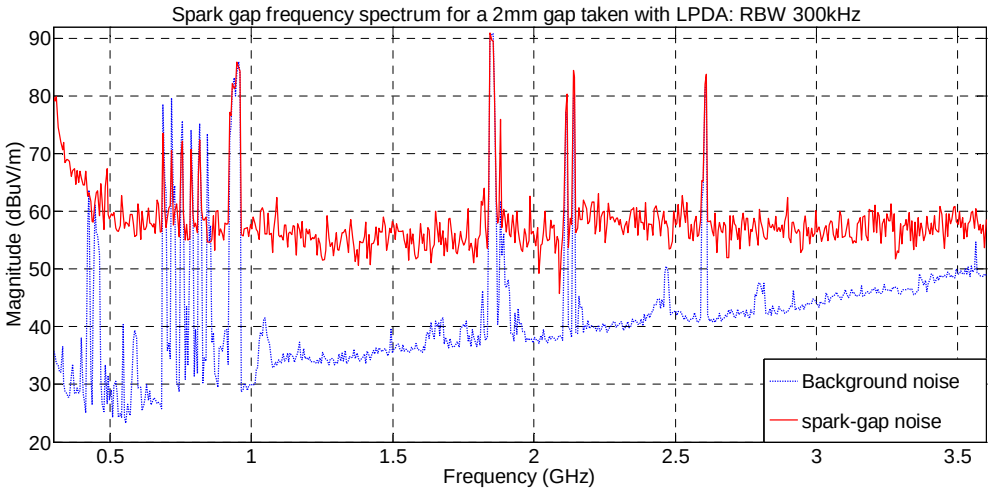

Figure A-1: Spark-gap frequency spectrum for a 2mm gap: RBW of 300 kHz

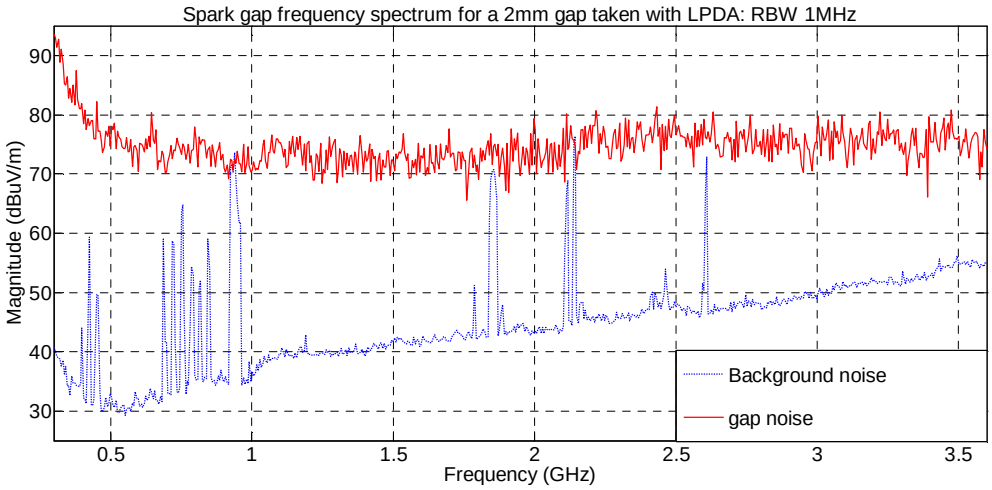

Figure A-2: Spark-gap frequency spectrum for a 2mm gap: RBW of 1MHz

Appendix B

Effect line voltage change on radiated sparking temporal pulse pattern

This appendix gives some additional measured time domain results from taken with the zero-span settings of SA at a frequency of 600 MHz. Figure B-1− Figure B-3 are the radiated pulse repetition pattern for a 2 mm gap length at supply voltage levels of 21, 26 and 30 kV, respectively. Figure B-4 and Figure B-5 are the patterns for a 6 mm gap length at voltage levels of 26 and 30 kV, respectively.

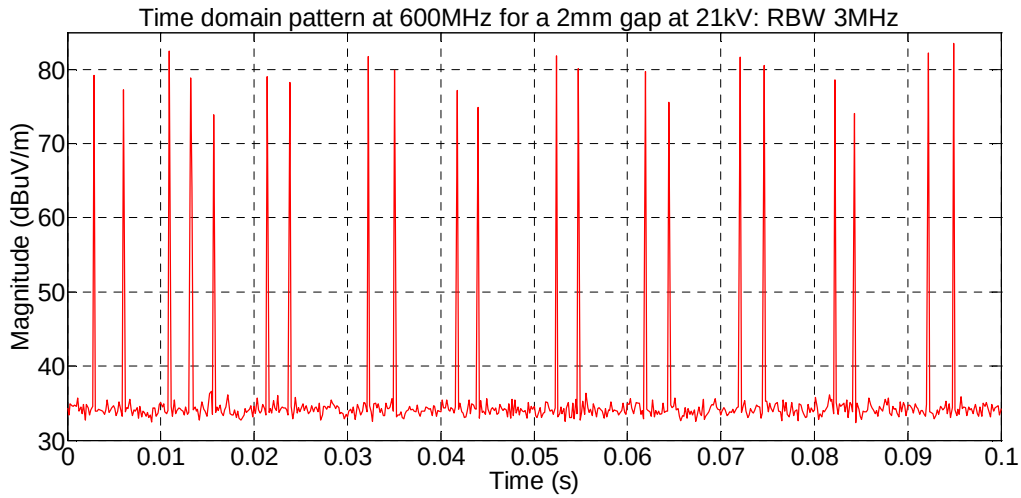

Figure B-1: Radiated sparking pulse repetition for a 2 mm gap length at voltage level of 21 kV

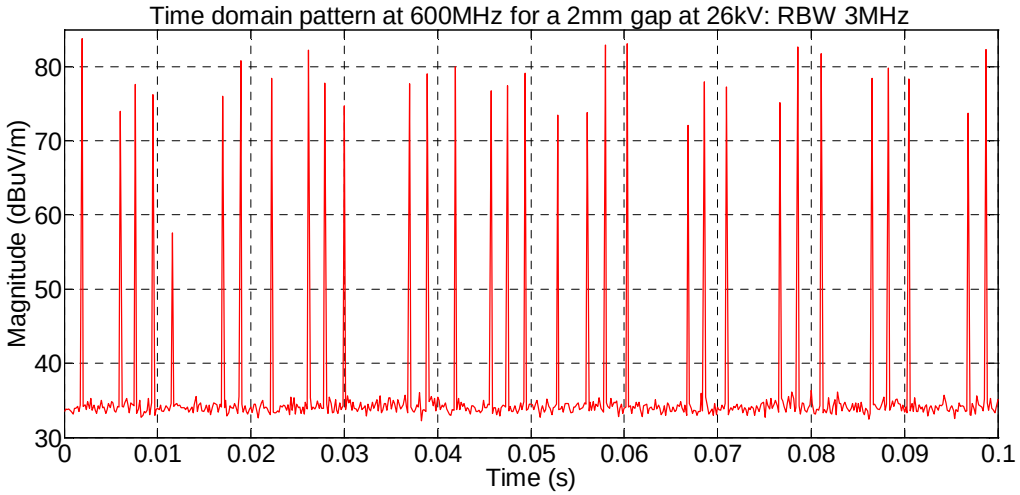

Figure B-2: Radiated sparking pulse repetition for a 2 mm gap length at voltage level of 26 kV

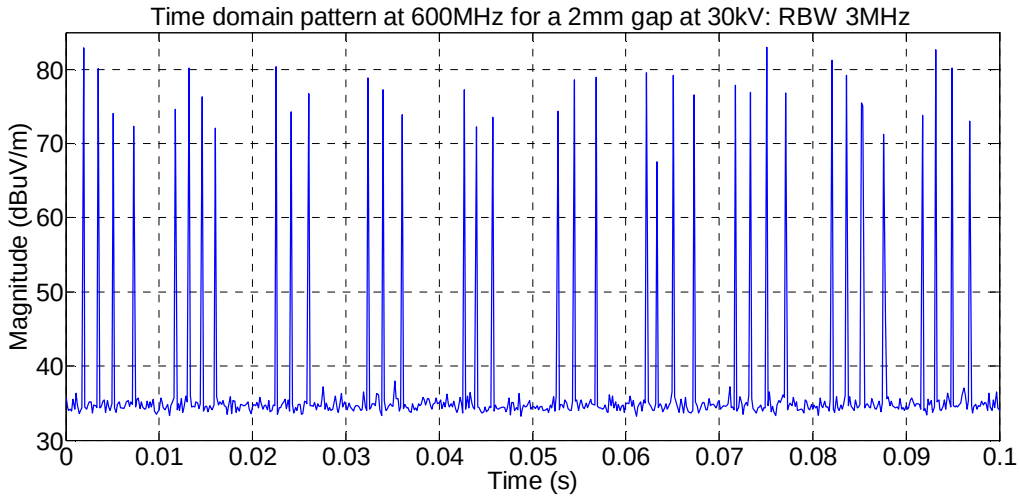

Figure B-3: Radiated sparking pulse repetition for a 2 mm gap length at voltage level of 30 kV

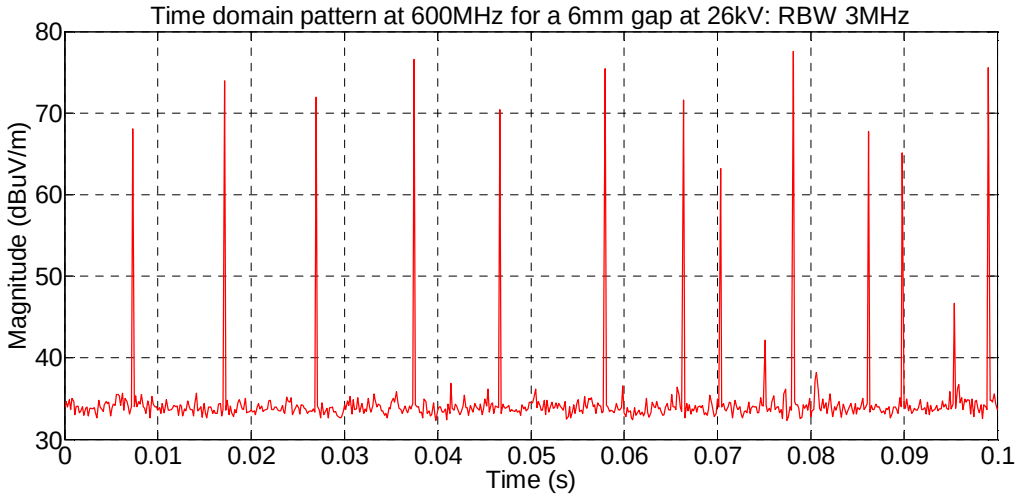

Figure B-4: Radiated sparking pulse repetition for a 6 mm gap length at voltage level of 26 kV

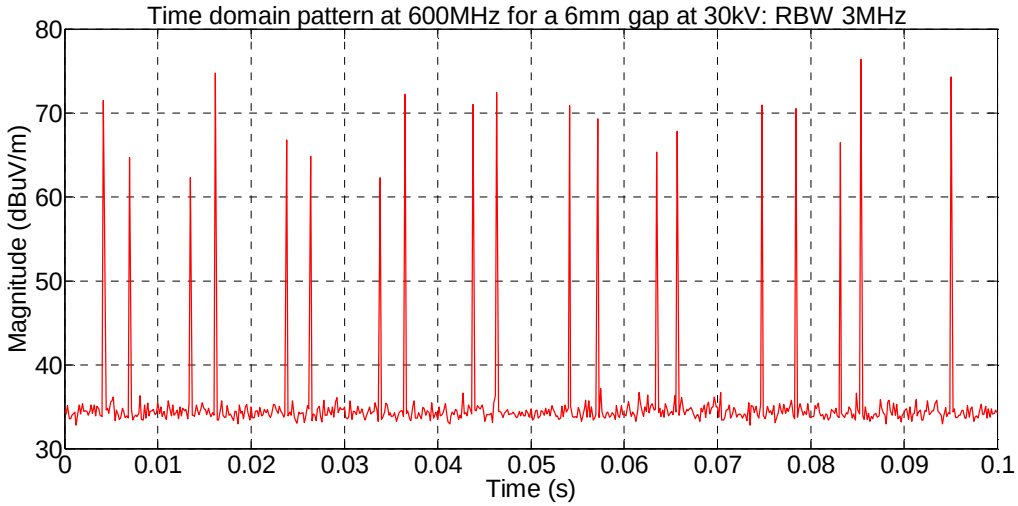

Figure B-5: Radiated sparking pulse repetition for a 6 mm gap length at voltage level of 30 kV

Appendix C

Scale-model lateral and longitudinal profiles

This appendix gives some typical lateral and longitudinal profiles for the PEC2 model that was computed at 2.5 GHz. Figure C-1 and Figure C-2 are the lateral profiles simulated along Lat1 and Lat2, respectively, while Figure C-3 is the longitudinal profile.

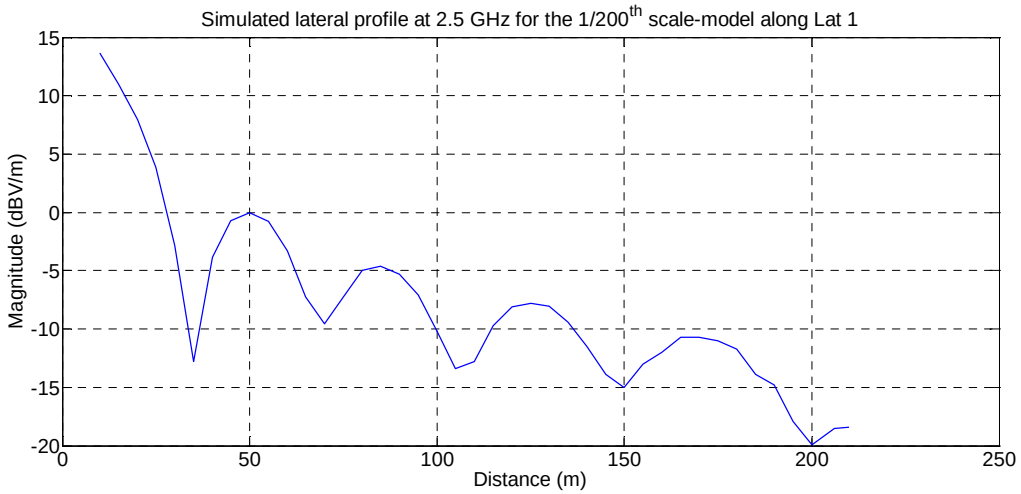

Figure C-1: The simulated near field lateral profile along Lat1 of PEC2 model at 2.5 GHz

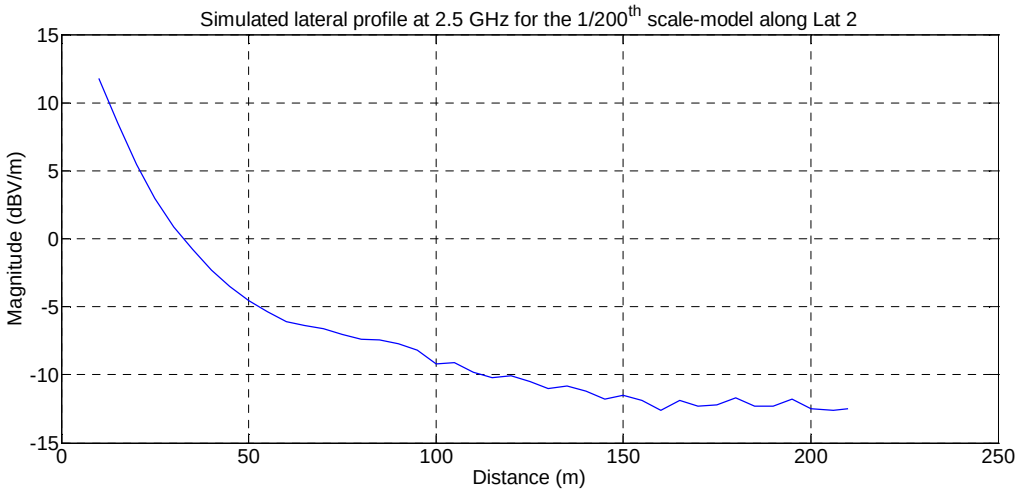

Figure C-2: The simulated near field lateral profile along Lat2 of PEC2 model at 2.5 GHz

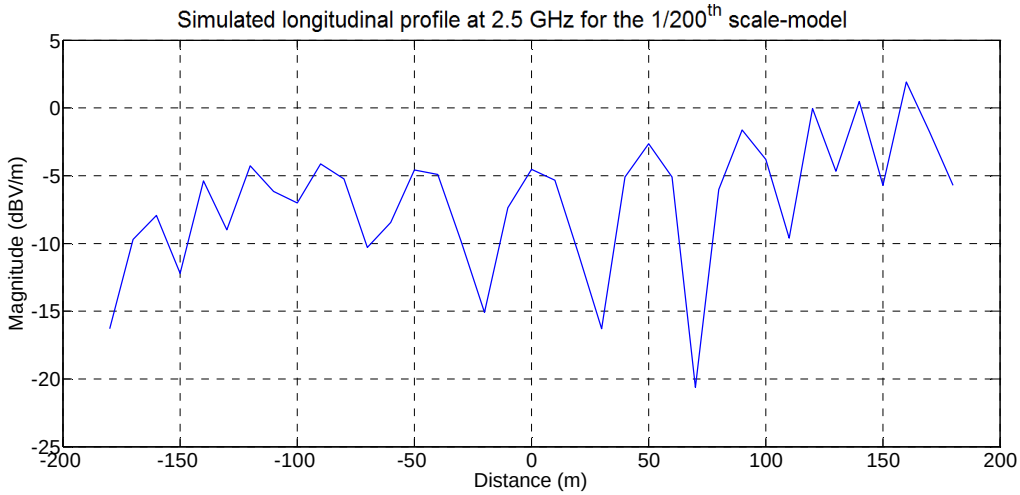

Figure C-3: The simulated near field longitudinal profile along Long of PEC2 model at 2.5 GHz

References

[1] Wilkinson P.N., "The Hydrogen Array," *URSI / IAU Colloquium 131, ASP Conference Series*, vol. 19, pp. 428-432, 1991.

[2] Swarup G., "An international telescope for radio astronomy," *Current Science*, vol. 60, pp. 106-108, 1991.

[3] Schilizzi R.T., "The Square Kilometre Array," in *Proceedings of the SPIE Conference on Astronomical Telescopes and Instrumentation*, Glasgow, UK, June 2004.

[4] Hall P. J., "The Square Kilometre Array: An international engineering perspective," *Experimental Astronomy*, vol. 17, no. 1-3, pp. 5-16, June 2004.

[5] Hall P., Schillizzi R., Dewdney P., and Lazio J., "The square kilometre array (SKA) radio telescope: progress and technical direction," *URSI. 236*, pp. 4-19, August 2008.

[6] Square Kilometre Array, the international radiotelescope for the 21st century. [Online]. http://www.skatelescope.org/

[7] Square Kilometre Array (SKA) Africa. [Online]. http://www.ska.ac.za/

[8] "Commencement of the Astronomy Geographic Advantage Act, 2007 (Act No. 21 of 2007)," Staatskoerant, No. 32163, April 2009.

[9] Tiplady A., "South African Radio Astronomy Service Protection Levels," SKA SA, RFI-WG Memo 12, Version 0.2, September 2008.

[10] International Telecommunication Union, "Protection criteria used for radio astronomical measurements," Recommendation ITU-R RA.769-2, 2003.

[11] Easton K.J., "Television Interference from Power Lines," *IEEE. Transactions on Cable Television*, vol. CATV-2, no. 4, pp. 162–168, October 1977.

[12] Pakala W. E. and Chartier V. L. , "Radio noise measurements on overhead power lines from 2.4 to 800 kV," *IEEE Transactions on Power Apparatus and Systems*, vol. PAS-90,

no. 3, pp. 1153 - 1165, 1971.

[13] German J. P., "Characteristics of Electromagnetic Radiation from Gap-type Spark Discharges on Electric Power Distribution Lines," *IEEE Transactions on Electromagnetic Compatibility*, vol. EMC-11, no. 2, pp. 83-89, May 1969.

[14] FEKO, Electromagnetic Software and Systems (EMSS). [Online]. http://www.feko.info/

[15] Hodge J. W., "A Comparison between Power-line Noise Level Field Measurements and Man-Made Radio Noise Prediction Curves in the High-Frequency Radio Band," Naval Postgraduate School, Monterey, CA., MS Thesis 1995.

[16] CISPR 18, *Radio Interference Characteristics of Overhead Power Lines and High Voltage Equipment.*: CISPR Standard, Publication 18-1, 1982.

[17] Sengupta D. L. and Liepa V. V., *Applied Electromagnetics and Electromagnetic Compatibility*. Hoboken, New Jersey, USA: John Wiley & Sons, 2006.

[18] Loftness M. O., "Power Line RF Interference -- Sounds, Patterns, and Myths," *IEEE Transactions on Power Delivery*, vol. 12, no. 2, pp. 934-940, April 1997.

[19] Begamudre R. D., *Extra High Voltage A. C. Transmission Engineering*. New Delhi: New Age International Limited Publishers, 2008.

[20] Goldman M., Goldman A. and Sigmond R. S. , "The corona discharge, its properties and specific uses," *Pure & Appi. Chem.*, vol. 57, no. 9, pp. 1353-1362, 1985.

[21] Lings R., *EPRI AC Transmission line reference book – 200 kV and above*, 3rd ed. Palo Alto, CA: EPRI, 2005.1011974.

[22] Nayak S. K. and Thomas M. J. , "An Integro-Differential Equation Technique for the Computation of Radiated EMI Due to Corona on HV Power Transmission Lines," *IEEE Transactions on Power Delivery*, vol. 20, no. 1, pp. 488 - 493, January 2005.

[23] Rakoshdas B., "Pulses and Radio Influence Voltage of Direct Voltage Corona," *IEEE Transactions on Power Apparatus and Systems*, vol. PAS-83, no. 5, pp. 483-491, May 1964.

References

[24] Maruvada P. S., *Corona Performance of High Voltage Transmission*. Baldock, Herfordshire , England: Research Studies Press Ltd, April 2000.

[25] Camp M. and Garbe H., "Parameter estimation of double exponential pulses (EMP, UWB) with least squares and Nelder Mead algorithm," *IEEE Transactions on Electromagnetic Compatibility*, pp. 675 - 678, Nov. 2004.

[26] Athanasios Papoulis, *Signal Analysis*. New York: McGraw-Hill , May 1977.

[27] Ryan H.M., *High Voltage Engineering and Testing*, 2nd ed.: Institute of Engineering and Technology, IET, 2001.

[28] Malik N. H. and Al-Arainy A. A., "EMI Characteristics of Distribution Lines Located in Desert Lands," *IEEE Transactions on Electromagnetic Combatibility*, vol. 31, no. 3, pp. 273-279, August 1989.

[29] Malik N.H., Al-Arainy A.A. and Qureshi M.I., *Electrical insulation in power systems*, Marcel Dekker Inc, Ed. N.Y. New York, USA, 1997.

[30] Vincent W. R., Munsch G. F., Adler R.W., and Parker A. A., "The mitigation of radio noise from external sources at radio receiving sites," Naval Postgraduate School, Monterey, CA, Handbook NPS-EC-07-002, May 2007.

[31] AI-Bahrani A. H. and Malik N. H., "Attenuation and EMI frequency spectrum for distribution lines," *Journal of Engineering Sciences, King Saud Univ., Riyadh, Saudi Arabia*, vol. 2, pp. 229-243, 1990.

[32] Huertas J. I., Barraza R. and Echeverry J. M., "Wireless data transmission from inside electromagnetic fields," in *6th International Conference on Electrical Engineering, Computing Science and Automatic Control,CCE,2009*, Toluca, Mexico, Jan. 2009, pp. 1-7.

[33] German J. P., "The Properties of the Radiation below 1 GHz from Gap-Type Electrical Discharges on Electric Power Distribution Lines," *IEEE Transactions on Electromagnetic Compatibility*, vol. 11G, pp. 35 - 42, June 1969.

References

[34] Tim Williams, *EMC for Product Designers*, 4th ed.: Newness, 2007.

[35] Larsen D. V., "The location of electromagnetic noise sources on power lines using radio direction finding and spectrum analysis techniques," *SAIEE*, 1979.

[36] Das S. K. and Rao P. H., "Calibration of antenna factor of a tuned dipole using two antenna method, NIST method and a proposed reference antenna," in *IEEE International Conference on Electromagnetic Interference and Compatibility*, Dec 1995.

[37] Harrold R.T., "The Spectrum Analyzer Applied to the Measurement of EHV Power Line Radio Noise," *IEEE Transactions on Power Apparatus and Systems*, vol. PAS-90, pp. 1837 - 1847, 1971.

[38] Paul C. R., *Introduction to Electromagnetic Compatibility*. New York: John Wiley & Sons Inc, 1992.

[39] Christoph Rauscher, "Fundamentals of Spectrum Analysis," Rohde and Schwarz, 2001.

[40] Urban R. G., "Modelling Corona Noise on High Voltage Transmission Lines," University of Stellenbosch, MSc. Thesis 2001.

[41] Johnson H. and Graham M. , *High-Speed Digital Design: A Handbook of Black Magic*. Englewood Cliffs, New Jersey 07632: Prentice Hall PTR, 1993.

[42] Weller D., "Relating wideband DSO rise time to bandwidth: Lose the 0.35!," *Agilent Technologies. EDN*, pp. 89-94, December 2002.

[43] "New Test Methodologies Improve EMI Testing Efficiency," Agilent Technologies, Application Note, 2008.

[44] Loftness M. O., KB7KK, *AC Power interference Handbook*, 3rd ed.: Percival Technology, Revised, 2007.

[45] Warburton F.W., Liao T.W., and Hoglund N.A., "Power Line Radiation and Interference above 15 MHz," *IEEE Transactions on Power Apparatus and Systems*, vol. PAS-88, no. 10, pp. 1492-1501, 1969.

[46] Balanis C. A., *Antenna Theory: Analysis and Design*, 2nd ed.: John Wiley & Sons. Inc,

1997.

[47] Reggiani U., Massarini A., Sandrolini L., Ciccoto M., Liu X., Thomas D. W. P., and Christopoulos C., "Experimental Verification of Predicted Electromagnetic Fields Radiated by Straight Interconnect Cables Carrying High-Frequency Currents," in *Proc. IEEE Bologna PowerTech Conf.*, Bologna, Italy, June, 2003.

[48] Balanis C. A. and Ioannides P. I., *Introduction to Smart Antennas*.: Morgan & Claypool Publishers, 2007.

[49] Rao S.M., Wilton D.R., and Glisson A.W., "Electromagnetic scattering from surfaces of arbitrary shape," *IEEE Trans Antennas Propag.*, vol. 30, pp. 409–418, 1982.

[50] Davidson D.B., *Computational Electromagnetics for RF and Microwave Engineering*, First Edition ed.: Cambridge University Press, 2005.

[51] Taheri P., Kordi B. and Gole A. M., "Electric Field Radiation from an Overhead Transmission Line Located Above a Lossy Ground," in *43rd International Universities Power Engineering Conference (UPEC 2008)*, Padova, Italy, September 2008, pp. 1-5.

[52] Olsen R.G, "Power Transmission Electromagnetics ," *IEEE Antennas and Propagation Magazine*, vol. 36, no. 6, pp. 7-16, December 1994.

[53] Balanis C. A., *Advanced Engineering Electromagnetics*. New York: John Wiley & Sons, 1989.

[54] Otto A.J., Reader H. C., and Marchand R. C., "Complex Permittivity Measurements of Karoo Soil for Square Kilometre Array," in *submitted to International Conference on Electromagnetics in Advanced Applications*, Torino, Italy, September 12-17, 2011.

[55] Semlyen A., "A. Semlyen, Ground Return Parameters of Transmission Lines an Asymptotic Analysis for Very High Frequencies," *IEEE Transactions on Power Apparatus and Systems*, vol. PAS-100, no. 3, pp. 1031-1038, March 1981.

[56] Theethayi N., Thottappillil R., Liu Y., and Montano R., "Important parameters that influence crosstalk in multiconductor transmission lines," *Electric Power System*

Research, vol. 77, pp. 896-909, 2007.

[57] Theethayi N. and Thottappillil R., "Surge propagation and crosstalk in multiconductor transmission lines above ground," in *Electromagnetic Field Interaction with Transmission Lines: from Classical Theory to HF Radiation Effects*, F. Rachidi and S.Tkachenko, Ed.: WIT Press, 2008, ch. 2, pp. 23-78.

[58] van der Merwe J., "Uniform Multiconductor Transmission Lines above a Dissipative earth: Direct FDTD Analysis and Experimental Validation," University of Stellenbosch, Ph.D. Dissertation 1998.

[59] Loftness M. O., "RFI Source-Locating on Power Lines -- An Update," *IEEE Transactions on Power Delivery*, vol. 4, no. 2, pp. 1137-1144, April 1989.

[60] Govind Swarup, "Power-line Radio Frequency Interference at the GMRT," NCRA-TIFR, Pune, NCRA Technical Report R233, 2008.

[61] Pathak S., Swarup G., Chatterjee A., Kale V., "Location of Radio Frequency Interference using GMRT," in *URSI General Assembly*, New Delhi, 2005.

[62] Roets H.A. and Britten A.C. , "Guidelines for the identification, location and correction of radio and television interference from High Voltage Lines," Pretoria, National Energy Council (NEC) Official Report 1992.

[63] Loftness M. O., "The Location of Power Line TVI: Some Reduction Considerations," *IEEE Transactions on Power Apparatus and Systems*, vol. PAS-89, no. 5/6, pp. 893-901, May/June 1970.

[64] Limberger E. N., "Locating Radio Frequency Interference On Power Lines," in *Papers Presented at the 36th Annual Rural Electric Power Conference*, New Orleans, LA, USA, May 1992, pp. C3-1 - C3-5.

[65] "Electrical Exterior Facilities," Joint Departments of the Army, the Navy and the Air Force, Washington, D.C., Technical Manual, TM 5-864/NAVFAC MO-200/AFJMAN 32-1082, November 1996.

References

[66] de Villiers W. and Tiplady A., "Powerline Design Study for the Minimisation of Spark-generated Interference," SKA SA, Johannesburg, Internal Technical Memo, 2009.

[67] De Villiers W., "Technical Note: Motivation for SKA Power Grid Design," MESA Solutions, Stellenbosch, Technical Report, available from SKA SA, August 2008.